UNIVERSITY OF OKLAHOMA

GRADUATE COLLEGE

GROWTH OF WIDE BANDGAP SEMICONDUCTORS USING PULSED ELECTRON BEAM DEPOSITION (PED) PROCESS

A DISSERTATION

SUBMITTED TO THE GRADUATE FACULTY

in partial fulfillment of the requirements for the

Degree of

DOCTOR OF PHILOSOPHY

By

NAZMUL AREFIN
Norman, Oklahoma
2015

GROWTH OF WIDE BANDGAP SEMICONDUCTORS USING PULSED ELECTRON BEAM DEPOSITION (PED) PROCESS

A DISSERTATION APPROVED FOR THE
SCHOOL OF ELECTRICAL AND COMPUTER ENGINEERING

BY

_____
Dr. Patrick J. McCann, Chair

_____
Dr. James J. Sluss, Jr.

_____
Dr. Zhisheng Shi

_____
Dr. Yan Zhang

_____
Dr. Michael B. Santos

To my dearest wife Fauzia and Son Fardis

Their sacrifice is the pillar of all my achievement

Acknowledgements

Thanks to Almighty Allah to allow me the opportunity to successfully complete my doctoral research. First, I would like to place my heartiest gratitude to Dr. Patrick J. McCann for his continuous support, guidance, and encouragement for last four years of my Ph.D. research. Without his valuable advice this project might not be possible. I consider myself fortunate to be one of his students, and believe his teaching and advising would help my next career path in every aspect. I also want to thank my previous advisor Dr. Matthew H. Kane. Without his initiative I could not get this excellent opportunity to dig in one of the most promising areas of solid state electronics. Many thanks to him for his valuable time and advice, regarding my research. Then, I would like to acknowledge the continuous support from Dr. James J. Sluss, Jr., during his office as the Director of ECE. I am grateful to Dr. Zhisheng Shi for his continuous support with the lab equipments. Dr. Yan Zhang has been a great patron for my research during my entire Ph.D. career. I am very grateful to Dr. Michael B. Santos for his continuous help with technical advice and help with equipment during my research.

I would like to deliver my heartiest gratitude to Dr. Matthew B. Johnson for his dedicated and unparalleled support during my research which has been a great asset for me. His advice and permission to use the resources, have expedite my work a lot. Also, my heartiest gratitude to Dr. Hjalti H. Sigmarsson, Dr. Daniel E. Resasco, Dr. Andrew S. Madden, Dr. Ian Sellers, Dr. Khalid Hossain (Amethyst Research Inc.), Dr. Vince R. Whiteside, Dr. Dachuan Shi, Dr. Wesley Tennyson, Dr. Binbin Weng, Dr. Preston Larson, Dr. Joel Keay, Dr. Jijun Qiu, Brittany N. Pritchett, Dr. Zhihua Cai, Dr. Namjou K. Khosrow, and above all Mr. Leonard E. Olona for their heartiest and dedicated

support in my tough hours. In the end, I want to place my gratitude to my parents and my family members, and my mother-in-law for their continuous prayers. I would like to thank my wife Fauzia Ahmed, and Son, Fardis Abyan Arefin for their patience, sacrifice and encouragement, during the progress of my work. Without their support, I could never reach this far!!!

Table of Contents

Acknowledgements iv

Table of Contents vi

List of Tables ix

List of Figures x

Abstract xv

Chapter 1 : Introduction 1

1.1 Motivation 1

1.2 Into the wide bandgap semiconductors 3

1.3 Study of WBG semiconductor properties 4

1.3.1 High power and high temperature electronics 4

1.3.2 Radio frequency (RF) industry 7

1.3.3 Solid state lighting industry 8

1.4 Challenges in establishing a competitive technology 8

Chapter 2 : Review on pulsed electron beam deposition (PED) process 13

2.1 Motivation 13

2.2 GaN films and devices (by MBE and MOCVD) 13

2.3 Low temperature growth processes 15

2.4 Pulsed electron beam deposition (PED) process 17

2.5 Plasma formation in PED process 19

2.6 Review: GaN growth using PED process 22

2.7 Review: ZnO growth using PED 26

2.8 Substrates for WBG III-nitride and II-oxide growth 29

2.9 Buffer layer strategy 31
2.10 Summary 34
Chapter 3 : PED growth process, plasma generation, and optimization 36
3.1 Motivation 36
3.2 System description 36
3.3 Substrate preparation 39
3.3.1 Sapphire cleaning 40
3.3.2 Silicon cleaning 40
3.3.3 Cleaning of buffered silicon samples 41
3.4 Target and plasma preparation 41
3.6 Thin film characterization techniques 53
3.6.1 Field emission scanning electron microscopy 53
3.6.2 Powder diffraction XRD 54
3.6.3 Photoluminescence (PL) 56
3.6.4 Rutherford back-scattering spectroscopy (RBS) 57
3.6.5 Hall measurement 58
3.7 Summary 59
Chapter 4 : Growth and characterization of wide bandgap materials 60
4.1 Motivation 60
4.2 Growth and characterization of ZnO films 60
4.2.1 Experimental Detail 60
4.2.2 Structural and morphological characterization 61
4.2.3 Optical characterization 71

4.2.4 Electrical characterization 74
4.2.5 Summary of ZnO growth 75
4.3 Growth and characterization of GaN films 76
4.3.1 Experimental Detail 76
4.3.2 Structural and morphological characterization 77
4.3.3 Optical characterization 83
4.3.4 Electrical characterization 85
4.3.5 Summary of GaN growth 87
4.4 Growth and characterization of AlN nanowires 87
4.4.1 Experimental detail 88
4.4.2. Structural and morphological characterization 90
4.4.3 Summary on growth of AlN NW 94
4.5 Summary 95
Chapter 5 : Future prospects of pulsed electron beam deposition process 96
5.1 Motivation 96
5.2 Modification of the existing PED system 97
5.3 New buffer layers for III-nitride growth at lower temperature 104
5.4 Continuation of previous research 108
5.5 Summary 108
References 109
Appendix A: PED System Drawings 113
Appendix B: Growth Specifications 123

List of Tables

Table 1.1: List of popular elemental and compound semiconductors.....4

Table 2.1: PED source (PEBS-21) specifications.....18

Table 2.2: Properties of potential substrates for III-nitride and ZnO epitaxy. 30

Table 2.3: Wafer curvature, AlN IL deposition temperatures, total stress, and lattice constants of GaN and $Al_{0.21}Ga0_{.79}N$ epilayers grow on AlN interlayer. 32

Table 3.1: Parameters for optimized plasma. 49

Table 3.2: Plasma generated reactive components of GaN target. 50

Table 3.3: List of characterization techniques used for thin film analysis.....53

Table 4.1: Parameters for ZnO/sapphire and ZnO/Si(100) growth 60

Table 4.2: Relative diffraction intensity from crystal planes of ZnO/sapphire samples. 67

Table 4.3: Distance between planes (observed in EBSD scan) of ZnO/sapphire samples. 67

Table 4.4: Relative diffraction intensity and distance between planes 71

Table 4.5: Summary of photoluminescence data from ZnO/Si(100) samples.....74

Table 4.6: Room temperature Hall measurement data for ZnO/sapphire and ZnO/Si(100) samples grown at different substrate temperatures. 74

Table 4.7: GaN thin film growth parameter on different substrates. 76

Table 4.8: Relative diffraction intensity from crystal planes of GaN samples.....82

Table 4.9: Distance between planes (observed in EBSD scan) of GaN samples. 82

Table 4.10: Growth parameters for AlN NW. 88

Table 4.11: Relative diffraction intensity and distance between two adjacent planes in AlN NW/sapphire and AlN NW/Si(111). 93

List of Figures

Figure 1.1: Energy bandgap schematic for insulators, conductors, and semiconductors..4

Figure 1.2: RF component market by 2016 with an annual CAGR of 7.9%.....8

Figure 2.1: Schematic of PED system.....18

Figure 2.2: Calculated penetration depth (range) of energetic electrons in Si (1), Al_2O_3 (2), and $YBa_2Cu_3O_x$ (3).....20

Figure 2.3: Schematic representation of pulsed electron beam deposition process.....21

Figure 2.4: RHEED patterns of GaN films grown on (a) Al_2O_3 and (b) 6H-SiC.....23

Figure 2.5: 2Θ/ω XRD curves, and (b) a typical GaN (10-12) pole configuration. 23

Figure 2.6: Time evolution of RHEED patterns and AFM images for GaN films grown on an atomically flat 6H-SiC substrate: (a), (b) 3 nm; (c), (d) 10 nm; (e), (f) 50 nm; and (g), (h) 200 nm. 24

Figure 2.7: Room temperature photoluminescence for 200 nm GaN/6H-SiC 25

Figure 2.8: RHEED pattern for a GaN/ZnO sample grown at 200^{o}C, (b) Zn2p XPS spectra for the GaN films grown at 500^o and 200^{o}C.....26

Figure 2.9: θ-2θ XRD diagram of ZnO thin film grown at 700^{o}C on *c*-plane sapphire, The inset shows the corresponding rocking curves of the (0002) reflection.....28

Figure 2.10: Al_2O_3 (01-18) and ZnO (10-13) pole figure of a ZnO film grown on *c*-plane sapphire. 28

Figure 2.11: Bandgap energy vs. lattice constants of III-nitrides, ZnO and their most common substrate materials. 29

Figure 2.12: The X-ray diffraction patterns of HT GaN films grown on the HT AlN-coated (1 1 1) Si substrates with AlN buffer layer.....34

Figure 3.1: Pulsed electron beam deposition (PED) system: GaNesis. 37

Figure 3.2: 2" Ni-Cr alloy platen, modified to house four 1cm x 1cm chips. 39

Figure 3.3: Emission spectroscopy of ZnO target after plasma generation using high energy electron bombardment.....43

Figure 3.4: Emission spectroscopy, with voltage variation, of (a) ZnI peak (480.94 nm), and (b) ZnII peak (491.16 nm) at 5.5 mTorr Ar pressure, with 1 Hz pulse rate, 2 mm gap. 46

Figure 3.5: Emission spectroscopy, with pulse rate variation, of (a) ZnI peak (480.94 nm), and (b) ZnII peak (491.16 nm) at 5.5 mTorr Ar pressure, with 11 KV pulse, 2 mm gap. 47

Figure 3.6: Emission spectroscopy, with vertical gap variation, of (a) ZnI peak (480.94 nm), and (b) ZnII peak (491.16 nm) at 5.5 mTorr Ar pressure, with 11 KV pulse, 3 Hz. 48

Figure 3.7: GaN emission spectrum in N_2 environment.....51

Figure 3.8: GaI peaks at 403.298 and 417.204 nm spectral lines. 51

Figure 3.9: NI peaks (atomic) at the 642.064 and 642.832 nm spectral lines. 51

Figure 3.10: Atomic GaI peak traces (time dependent) with chamber pressure dependency. 52

Figure 3.11: Atomic NI peak traces (time dependent) with chamber pressure dependency. 52

Figure 3.12: HR-FESEM system at University of Oklahoma. 54

Figure 3.13: Rigaku Ultima IV powder diffractometer (Courtesy of 55

Figure 3.14: Photoluminescence system setup (Courtesy of.....57

Figure 3.15: Ion Beam Analysis system hosting RBS system (top). Schematic of the system (bottom) (Courtesy: Dr. Khalid Hossain, Amethyst Research Inc, OK). 58

Figure 3.16: (a) Ecopia HMS-5000 Hall Effect Measurement system, (b) sample mounting fixture with upper cooling reservoir, and (c) sample mounting fixture (Photo: courtesy of Dr. Patrick. J. McCann, University of Oklahoma). 59

Figure 4.1: SEM images of ZnO on sapphire- grown at 700^{o}C: (a) planar, ...62

Figure 4.2: ZnO on sapphire: growth rate as a function of temperature. 63

Figure 4.3: EDX analysis of ZnO/sapphire grown at (a) 700^{o}C, (b) 500^{o}C, and (c) 300^{o}C. 64

Figure 4.4: Θ-2Θ scans from x-ray powder diffraction for ZnO/sapphire samples grown at (a) 700^{o}C, (b) 500^{o}C, and (c) 300^{o}C. 65

Figure 4.5: Kikuchi patterns generated from electron back-scattered diffraction (EBSD) from ZnO/sapphire samples grown in (a) 700^{o}C, (b) 500^{o}C, and (c) 300^{o}C. 66

Figure 4.6: EBSD mapping obtained for ZnO/sapphire samples grown at 68

Figure 4.7: SEM images of ZnO on Si(100) grown at 500^{o}C: (a) planar, (b) cross-section, and at 300^{o}C: (c) planar, (d) cross-section. 69

Figure 4.8: θ-2θ scans from x-ray powder diffraction for ZnO/Si(100) 69

Figure 4.9: Kikuchi patterns generated from electron back-scattered diffraction (EBSD) from ZnO/Si(100) samples grown in (a) 500^{o}C and (b) 300^{o}C. 71

Figure 4.10: Photoluminescence spectra of ZnO/sapphire samples grown at (a) 700^{o}C, (b) 500^{o}C, and (c) 300^{o}C. Blue and red lines are the PL responses in 4K 73

Figure 4.11: Photoluminescence spectra of ZnO/Si(100) samples grown at (a) 500°C and (b) 300°C. Blue and red lines are the PL responses in 4K and room temperature, respectively. 73

Figure 4.12: SEM images of GaN on sapphire- grown at 750°C: (a) planar, (b) cross-section, on Si(111) at 600°C: (c) planar, (d) cross-section, on Ge/Si(111) at 600°C: (e) planar, (f) cross-section, and on ZnO/sapphire at 300°C: (g) planar, (h) cross-section. .78

Figure 4.13: XRD scan (powder diffraction) for (a) GaN/sapphire, (b) GaN/Si(111), (c) GaN/Ge/Si(111), and (d) GaN/ZnO/sapphire. 79

Figure 4.14: Kikuchi patterns generated from electron back-scattered diffraction (EBSD) from (a) GaN/sapphire, (b) GaN/Si(111), (c) GaN/Ge/Si(111), and (d) GaN/ZnO/sapphire. 81

Figure 4.15: EBSD mapping of a selected area from (a) epilayer: GaN/ZnO/sapphire and (b) buffer: ZnO/sapphire. 82

Figure 4.16: RBS scanning of (a) GaN/sapphire, ...83

Figure 4.17: Photoluminescence spectra of (GaN/Si(111)) at (a) 4K, (b) 295K, (GaN/Ge/Si(111)) at (c) 4K, and (GaN/ZnO/sapphire) at (d) 4K. (Blue lines: PL spectra before H passivation, and Red lines: PL after H passivation). 84

Figure 4.18: Temperature dependent conductivity and mobility of (a) GaN/Si(111) and (b) GaN/Ge/Si(111). Temperature dependent bulk and sheet carrier concentration of (c) GaN/Si(111), and (d) GaN/Ge/Si(111). 86

Figure 4.19: Emission spectra of aluminum lines (a), and nitrogen lines (b) and (c).....89

Figure 4.20: SEM image of AlN nanowires on sapphire: (a) a single nanowire showing length of > 100 µm, (b) segment of a NW with diameter of ~ 2.5 µm, and (c) cross-

section of AlN NW on sapphire sample. AlN nanowires on Si (111): (d) a single nanowire showing length. 90
Figure 4.21: (a) An AlN NW on sapphire, subject to EDX analysis; EDX scan at (b) the base: Spec 1, (c) middle of the NW: Spec 2, and (d) tip of the NW: Spec 3. 92
Figure 4.22: Changes in Al and N atomic weight percentage 92
Figure 4.23: X-ray powder diffraction scan of AlN NW on sapphire. 93
Figure 4.24: Kikuchi patterns generated from electron back-scattered diffraction (EBSD) in (a) AlN NW on sapphire and (b) AlN NW on Si(111). 93
Figure 5.1: PED chamber with pressure variation during growth. 99
Figure 5.2: Variation of directional and thermal velocities with respect to changes in the normalized distance from the target surface. 101
Figure 5.3: Changes in pressure, plasma temperature, and mean-free path 103
Figure 5.4: Variation of directional and thermal velocities with respect 103
Figure 5.5: GaN/PbSe/BaF_2/CaF_2/Si(111) structure. 106
Figure 5.6: Powder XRD scan of GaN growth on (a) PbSe/BaF_2/CaF_2/Si(111) 107

Abstract

Wide bandgap materials hold a great potential in solid state lighting, power electronics, and radio frequency (RF) device applications. The cumulative market for all these applications is forecasted to be approximately $75 billion within a decade. The most promising wide bandgap materials are gallium nitride (GaN), aluminum nitride (AlN), their pseudobinary ternary alloys ($Al_{1-x}Ga_xN$), and zinc oxide (ZnO). This dissertation describes the development of growth processes for binary GaN, AlN, and ZnO films on various cost-effective substrates (sapphire and silicon) using the pulsed electron beam deposition (PED) technique. PED is a physical vapor deposition process that deposits materials through generation of high energy plasma from a target material using 10 to 15 keV electron beam pulse bombardment on the target surface at a 1-10 Hz pulse rate with a peak current density of ~10^6 A/cm^2 during the 70 to 100 ns pulse duration.

ZnO was grown on sapphire at 300^{o}C, 500^{o}C, and 700, and on Si(100) at 300^{o}C and 500^{o}C. The grown samples were studied using structural (scanning electron microscope, x-ray diffraction (XRD), Rutherford back-scattering, electron back-scattered diffraction), optical (photoluminescence (PL)), and electrical (Hall effect measurement) characterization methods. The ZnO/Si(100) samples, which had thicknesses between 68 nm and 130 nm, showed crystalline morphology along with near-band edge optical emission at 370 nm (3.36 eV) with very weak luminescence from defect bands. Measured electron densities and mobilities were in the range of 10^{20} cm^{-3} and 44.74 cm^2/Vs, respectively. By contrast, ZnO layers grown on sapphire substrates exhibited PL emission in the 500-700 nm (1.78-2.49 eV) indicating high

density of defects with energy levels in the ZnO band gap and a much lower electron mobility of ~10 cm^2/Vs. GaN was grown on sapphire, Si(111), and Ge/Si(111) at 600^oC. Measurement of the GaN/Si(111) sample showed only a polar (0002) x-ray diffraction peak, near band edge PL at 368.5 nm (3.37 eV), and an electron mobility of 300 cm^2/Vs at room temperature. Passivation of this material using hydrogen implantation improved the PL emission intensity by more than 100%. GaN was also grown on sapphire using a ZnO buffer layer, with a growth rate of 0.31 Å/pulse. PL characterization showed presence of near band edge emission (at 371.5 nm at 4K) with a strong defect band due to nitrogen vacancies. EBSD scan of the GaN surface demonstrated *c*-plane (0002) orientation.

AlN nanowires (NW) were grown on sapphire and Si(111) substrates at low temperatures such as 500^oC. SEM imaging reported that the nanowires were 100 µm long with an average diameter of 2.5 µm. Also EBSD scan verified the NW structures as hexagonal wurtzite structures.

This dissertation concludes with suggestions for future improvements for the PED equipment and the growth processes. Additional tasks for future application of this tool are (i) add a butterfly valve for better control of the chamber pressure, (ii) add a shutter to protect the growth substrate during first stages of plasma formation. In addition, initial results involving the use of compliant buffer layer materials such as IV-VI semiconductors grown by molecular beam epitaxy (MBE) to reduce strain effects in GaN growth are presented in the concluding section.

Chapter 1 : Introduction

1.1 Motivation

Wide bandgap (WBG) materials offer a lot of opportunities in the electronics and illumination industries. For efficient energy applications, wide bandgap compound semiconductors, such as GaN, AlN, ZnO, AlGaN, InGaN, AlInGaN hold lot of potential to yield smaller, faster, more reliable, and more efficient devices than existing smaller bandgap silicon based components. All these advances would result in improvement in volume, performance, and cost of industrial applications as well as save more money offering extended applications for future expansion. Attaining these improvements would certainly impact the energy consumption in both industrial and consumer sectors. Since the world is challenged by the upcoming scarcity of natural resources and optimized resource utilization is encouraged, the use of efficient electronic systems would be highly effective to tackle the problems. Furthermore, the use of solid state technology also promotes green and clean energy which would be very effective to lower the carbon emission issue that threatens the natural stability all over the world today.

Wide bandgap materials are now considered the most promising technology after the takeover of transistor world by silicon from germanium in the 1960s, since they offer devices that work in higher temperature, voltage, and frequencies. Thus, the power electronic devices are more powerful and versatile in nature compared to the conventional silicon based power electronics. Wide bandgap materials are also very strong candidates for the illumination industry since the first demonstration of blue light emission using GaN by Nakamura *et al.* [1]. Wide bandgap semiconductors, especially,

III-nitrides (such as AlN, GaN, and their ternary and quaternary alloys) have grabbed attention among the researchers all over the world. The inventions of Nakamura [2] showed that III-nitride based light emitting diodes (LEDs) can produce the same amount of light as an incandescent light bulb with only $1/10^{th}$ the power consumption. Since nitride based technology offers high brightness, durability, and energy efficiency, government organizations, universities, as well as private firms have invested lot of manpower and money in maturing this technology to establish a solid state lighting industry based on nitride semiconductors. In the later portion of this chapter the market impact of solid state lighting based on III-nitride technology will be discussed.

Radio frequency (RF) devices are also facilitated by the wide bandgap semiconductors because of the same properties that influence its expected dominance in the power electronics industry. High power density of these materials allow smaller device structures thus reducing input and output capacitances and increasing the bandwidth of the device as compared to the silicon-based RF devices. High breakdown voltage increases the device operating range (in terms of voltage) and helps in impedance matching. Efficiency is a vital aspect in RF engineering and wide bandgap semiconductor devices provide lower power loss thus facilitating development of more complex systems such as phased array radar systems. The broadband capability provides coverage for a broadband frequency range to support both the application's center frequency as well as the signal modulation bandwidth [3]. With all these features being offered, wide bandgap materials are now widely recognized as the enabling technology for next generation RF systems. For example, GaN-based power amplifiers

can find important applications in weather and military radar systems, telecom base stations, and in military and satellite communication modules.

1.2 Into the wide bandgap semiconductors

To have an idea of the wide bandgap semiconductor materials we first need to know how is their larger bandgaps make III-nitrides, ZnO, and SiC different from silicon. In a semiconductor material, most of the electrons reside in the valence band, which upon excitation (thermally, optically, or electrically) become energized and jump to a higher energy band called conduction band. This quantized jump into the conduction band allows the electron to move more freely under an external influence such as an applied voltage. The energy difference between the bottom of the conduction band and the top of the valence band is called the bandgap. It is very high for insulators, moderate for semiconductors, and non-existent for metals (see Figure 1.1 [4]). In general, a larger bandgap can withstand a larger applied electric field without experiencing dielectric breakdown. A larger bandgap semiconductor is therefore desired for high power electronic applications where high voltages are involved. Wide bandgap materials have bandgaps larger than those of more conventional semiconductors such as Si (1.1 eV) or GaAs (1.4 eV).

The following list presents some popular wide bandgap semiconductors (highlighted, along with conventional elemental and compound semiconductors), potential candidates for illumination, and electronic applications.

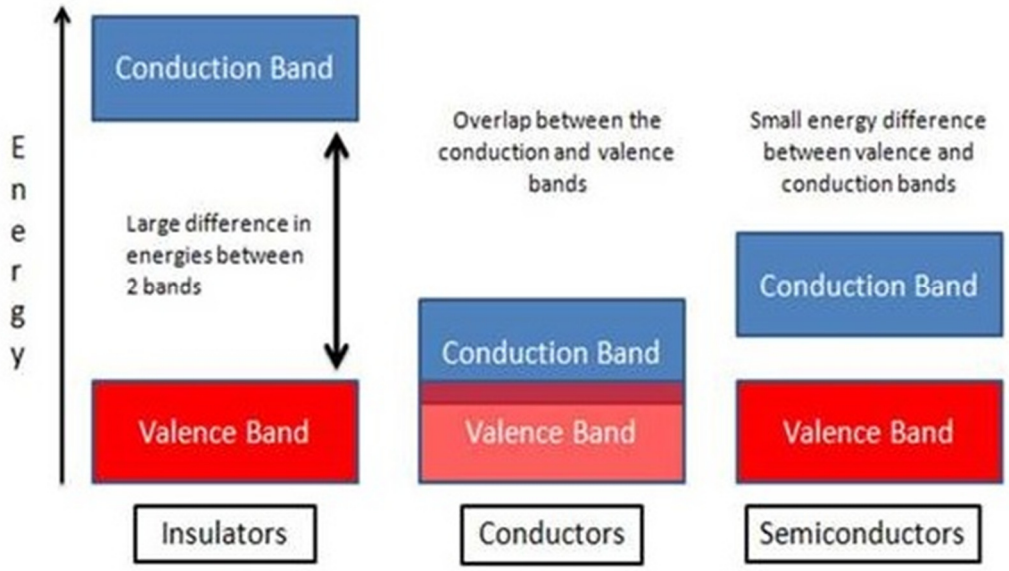

Figure 1.1: Energy bandgap schematic for insulators, conductors, and semiconductors.

Table 1.1: List of popular elemental and compound semiconductors.

Material	Chemical symbol	Bandgap energy (eV)
Silicon	Si	1.1
Germanium	Ge	0.7
Gallium Arsenide	GaAs	1.4
Silicon Carbide	SiC	3.3
Gallium Nitride	GaN	3.4
Zinc Oxide	ZnO	3.3
Diamond	C	5.5

1.3 Study of WBG semiconductor properties

In the following, a discussion will be presented on the major applications of wide bandgap semiconductor materials. Their technical advantages over conventional semiconductor materials and their market possibilities will be provided.

1.3.1 High power and high temperature electronics

The power electronics industry requires high power electronic devices such as junction field effect transistors (JFETs), bipolar junction transistors (BJTs), metal-oxide-semiconductor field effect transistors (MOSFETs), thyristors, rectifiers, and

insulated gate bipolar transistors (IGBTs). All these devices are used in different operating voltages (ranging from 0-1200+ V) and from low to high temperature operating conditions. Some key properties of power electronic devices that influence the choice of material and component design include: high frequency operation, high voltage, high temperature, and low Joule heating loss. The power electronics market is currently still dominated by silicon devices such as IGBTs, which are used widely in electric and hybrid vehicles, for example. Wide bandgap materials with their higher breakdown voltages, faster switching frequencies, lower on resistances, and higher operating temperatures offer many efficiency advantages over silicon-based IGBT technologies.

Among all the WBG materials SiC is the most mature technology so far. SiC-based devices have lower Joule heating losses higher frequency switching over the traditional Si power devices yielding more compact power module designs that can handle much larger kV-scale voltages. Another advantage of SiC is its high thermal conductivity. Usually the performance of Si based power electronic devices start deteriorating after 150^{o}C, while the SiC devices can still be operated reliably above this temperature. Device robustness at higher temperature reduces cooling and thermal management requirements (needed for Si devices) ensuring lower assembly cost and smaller form factors. In addition, vertical device assembly is possible for SiC devices with homogeneous epitaxy (SiC/SiC) that improves the device properties because of more effective heat dissipation. SiC devices have the capability to tolerate high current and voltage impulses thus improving device robustness in terms of transient device characteristics.

There is one drawback of the SiC technology that is forecasted to be the primary reason that can allow the penetration of GaN based devices in the market: cost of manufacturing. Although the SiC power devices outperform the Si devices in every aspect of device properties, the cost of wafers and material influences technologists to explore development of more cost-effective solutions. Although homogenous GaN on GaN bulk devices are more expensive than SiC on SiC device technology, GaN on SiC technology can be used to develop reduced cost devices. A more cost effective approach lies with GaN on silicon devices. It is expected that the performance of GaN-on-Si power devices would match up with the Si power devices in the sub 900V range by the first quarter of 2015, however, the technology depends a lot on the research and development to be undertaken in next few years. Key issues to be addressed are epi/substrate lattice parameter mismatch and thermal expansion coefficient mismatch.

The leading market applications of WBG semiconductors are renewable energy (solar, and wind), hybrid/electric vehicles, and consumer appliances. The sales of SiC power devices was $200 million in 2013 with a forecast to rise towards $1.8 billion by 2022, which will be only 2.4% of the forecasted global power semiconductor market in 2022 ($75 billion). On the other hand, by 2022, the global sales for GaN power devices is expected to reach up to a billion USD, which assures dominance of the silicon power devices over the market for next few years. However, the performance improvements would continue to influence technologists to hunt for a proper alternative to Si devices, ultimately heading towards the efficient application of GaN-on-Si technology ensuring both cost effective and improved device performance.

1.3.2 Radio frequency (RF) industry

Major applications of WBG semiconductors in the RF applications include lateral high electron mobility transistors (HEMTs) and MMICs (monolithic microwave integrated circuits). HEMTs are field effect transistors with a high density two-dimensional electron gas channel (produced by the sandwich between two different WBG materials), capable of operating with faster switching transients than conventional MOS or IGBT devices. On the other hand, MMICs are integrated circuits capable of operating in the range of 300 MHz to 300 GHz, with applications in the areas of RF electronics, microwave mixing, power amplification, and low-noise amplification, yielding RF devices such as broadband amplifiers, radar, base transceiver systems, high power defense and satellite communication modules [5].

In Figure 1.2 [6], a market study of Yole Developpment from France, it appears that the RF component market has a forecasted steady growth until 2016 with CAGR rate of 7.9%. However, the RF device market being comprised of different segments. Another rapidly growing RF application of components based on WBG semiconductor materials is in antenna switches. According to Yole's report, the state of the art LTE technology and increased number of signals have highly influenced the high frequency switching criteria. High RF power density yields smaller die size and more easily realized input and output circuit matches. Thus new WBG materials with their higher carrier density are expected to play a leading role in developing advanced architectures for LTE compatibility.

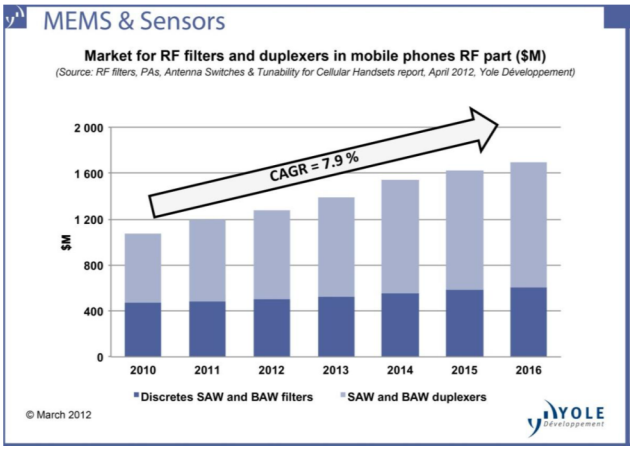

Figure 1.2: RF component market by 2016 with an annual CAGR of 7.9%.

1.3.3 Solid state lighting industry

First demonstration of LED made from wideband gap materials was done by Henry J. Round [7], however, the phenomenon was unexplained for one more decade, and the research direction turned to a different direction [8]. The dominance of wide bandgap materials, especially the III-nitride materials, started with the application in the lighting sector back in the early 90's with the works of Nakamura [2]. Since then solid state lighting industry has been revolutionized and reached a $15 billion market today with a forecast to grow to $42.7 billion by the end of 2020 [9]. It is expected that by 2020 that 20% of global lighting will be dominated by WBG material based solid state lighting technology. In addition, WBG materials are used for laser diodes, the key component in Blu-Ray disc players. Future applications of WBG materials include UV LEDs, which can be used for water and air sterilization and for chemical substance detection.

1.4 Challenges in establishing a competitive technology

Although SiC is a relatively mature technology used in some of the applications mentioned above, III-nitride based technology holds strong potential in terms of product

performance, cost effectiveness, and opportunities for mass production. In case of solid state lighting, power electronics, and RF systems cost is a vital factor that drives the choice of the consumer. Although SiC devices offer good performance in the power electronics and RF applications, they are very expensive. Si devices, although being cheap, are not capable enough to match with the device performances offered by WBG device technologies. On the other hand, the III-nitride technology dominates in the lighting industry, but in case of transistor device applications it suffers from poor performance due to thermal management problems associated with use of low thermal conductivity sapphire substrates. Use of bulk GaN as a substrate overcomes this problem, but device cost is increased substantially making this approach not viable for commercial success.

As a cost effective solution, it is desired to establish GaN on silicon as an alternative to all the GaN/SiC, SiC/SiC, and GaN/GaN thin film growth technologies. As an example, a 2" SiC wafer costs approximately $2000, while a Si(111) is only $8 for the same size. Furthermore, we have a very mature and established silicon wafer manufacturing industry and this established infrastructure can be used for low cost production of GaN based devices. In addition, if group III-nitride materials technology could be monolithically integrated with the silicon-based circuit technology then new opportunities for development of novel device concepts can be explored.

The major obstacles to achieve a silicon substrate technology for III-nitride device manufacturing involve overcoming the problems associated with lattice parameter and thermal expansion mismatch. Lattice mismatch causes defects in the deposited III-nitride epilayers on silicon. This can be tackled with the development of a

buffer layer technology that reduces the mismatch impact on the epilayer grown above it. Thermal expansion mismatch causes strain, and in severe cases cracks, in the epilayer as the contraction rates during cool down from the growth temperature are not same for Si and III-nitrides. This could be tackled through development of a low temperature growth process for III-nitrides. Currently available MBE and MOCVD processes involve very high growth temperature (at least 800^{o}C) for III-nitride epitaxy. The objective of the research described in this dissertation involves this last issue. The objective is to develop a new kind of epitaxial growth process that involves less substrate heating and simultaneously ensuring presence of highly energized reactant atoms capable of enough kinetic energy to facilitate growth of high crystalline quality III-nitride materials at low substrate temperatures.

This dissertation describes the development of a pulsed electron beam deposition (PED) process for growth of wide bandgap semiconductors. In a nutshell, this technology involves creation of plasma through high energy electron bombardment on a high purity sintered target material. The plasma is comprised of high energy atomic particles of the target material. The wafer surface, located at a vertical distance from the creation of the plasma, is positioned to collect these reactive atomic species where they can form a solid film. Commercial CVD and MBE processes involve high growth substrate temperatures to achieve the necessary surface chemical reactions and adatom migration for good epitaxial layer growth. The objective of this research is to explore the possibility for good epitaxial layer growth where the substrate can be at a lower temperature while surface chemical reactions and adatom migration are enhanced due to the plasma generated during the PED process. Ability to grow wide bandgap materials

like GaN and ZnO material at lower substrate temperatures on cost-effective substrates such as silicon will lead to new commercial applications for these materials.

So far, the first chapter of the dissertation focused on the opportunities of the wide bandgap materials in the power electronics, RF industry, and solid state lighting technology. The current market has been analyzed with a focus on the on growing demand and potential applications.

In chapter two, review is done on III-nitride (GaN) and II-oxide (ZnO) growth processes commercially available. The advantages of pulsed electron beam deposition process are demonstrated in comparison to molecular beam epitaxy, metal-organic chemical vapor deposition and pulsed laser deposition processes. It is easily distinguishable that PED possess some unique features allowing it to be a very strong candidate for low temperature growth process for III-nitride and II-oxide semiconductor fabrication. Description of the custom designed pulsed electron beam deposition system is presented in this chapter along with the recent applications of this process for wide bandgap thin film and nanowire growth.

PED process is comparatively new in nitride research. In chapter three, a quantitative analysis of wide bandgap material plasma in both N_2 and Ar environment will be analyzed. Varying the process variables, such as, pressure, pulse rate, electron energy, plots will be generated to present detail analysis of the PED generated plasma. It is to mention that the plasma of wide bandgap materials used in this research shows strong presence of metal reactant atoms in the ‘eye’ of emission spectroscopic analyzer, while the presence of ‘N’ and ‘O’ reactive atomic component is very low, since they recombine faster than the metal reactants. An optimized plasma generation process is

demonstrated that confirms the presence of the reactive anion components in the plasma. In addition, an overview of the thin film characterization techniques will be presented in this chapter.

Chapter four will present the detail growth process using PED. Plots describing the finding will be presented along with characterization of the films using different techniques, such as, SEM, EDS, EBSD, XRD, photoluminescence, Hall measurement etc. in this work, we successfully demonstrate the growth of AlN NW on sapphire and Si(111) at low temperature (~500^{o}C), growth of GaN thin film on sapphire, Si(111) and Ge/Si(111) at 600^{o}C with better crystallinity. In addition, growth of ZnO on sapphire and Si(100) is demonstrated at temperatures as low as 300^{o}C.

Chapter five concludes the findings and forecasts on some possible advanced use of PED low temperature growth, in terms of easy epi transfer to some other substrates through the application of flip-chip bonding process. We have found some success in growing low temperature GaN on some MBE grown IV-VI buffer layers on Si(111). However, the material properties still need further improvement in terms of crystallinity compared to the ones grown on bare silicon and sapphire. Additional modifications of the existing PED system design will be presented with the possible improvements expected.

Chapter 2 : Review on pulsed electron beam deposition (PED) process

2.1 Motivation

The previous chapter described a big picture for the applications and the markets of wide bandgap semiconductor materials. The technical issues involved with developing a cost-effective low temperature growth process for obtaining wide bandgap semiconductors were also outlined. This chapter will focus on the current growth technology using silicon as a substrate followed by a description on the pulsed electron beam deposition (PED) process. Plasma formation mechanism in PED will be presented later with a comparative discussion to the pulsed laser deposition (PLD) process. Review on application of PED in III-nitride and ZnO growth will demonstrate the achievement so far using this comparatively newer growth process. In a later section, properties of different substrates will be presented followed by a discussion on the most common buffer layer strategies that are used in the industry to overcome the epi-substrate mismatch issues.

2.2 GaN films and devices (by MBE and MOCVD)

Temperature is a very important issue for thin film growth. The large difference of thermal expansion coefficients (TEC) between GaN and silicon (111), i.e., $\alpha_{GaN} - \alpha_{Si} = 2.9 \times 10^{-6} K^{-1}$ results in a 56% thermal mismatch leading to bows and cracks in GaN epilayers in an attempt to obtain a sufficient thickness. Because, the difference in TECs of the epi and the substrate materials lead to tensile stress on the GaN epilayer, as the temperature reduces from growth temperature (~850^{o}C for MBE and 950^{o}-1100^{o}C for MOCVD) to room temperature. The GaN epilayer needs to be grown as compressively

strained to assist in compensating the TEC mismatch. Thus a suitable interlayer is required between GaN and Si to impose compressive strain. The lattice constant of AlN is a_{AlN} = 3.112 Å, and this is smaller than that of GaN resulting in obtaining a better matched completely relaxed nucleation layer which helps to grow GaN compressively strained on it with a 2.5% larger in-plane lattice parameter. In addition, AlN has a wurtzite crystal structure resembling a similar kind of planar and vertical expansion behavior to GaN.

In the case of most commercial production, the MOCVD process is widely used for GaN growth. MBE is also used, but compared to the growth rate of MOCVD, MBE is typically much less. The MOCVD process yields a few microns per hour growth rate while it is quite challenging to get a micron/hour growth rate from a regular MBE growth. It has been reported that GaN can be grown on AlN/Si wafers at 740^{o}C [10] and at 700^{o}C [11] using plasma assisted MBE. Aidam *et al* [11] demonstrate the lowest MBE growth temperature (700^{o}C) reported so far. But the disadvantage lies in the low growth rate of the MBE (growth rate of 0.5 µm/hr) [12] in comparison to MOCVD growth rate (5 µm/hr) [13]. In case of MOCVD growth, similar kind of thermal responses were observed as they appeared for MBE growth processes. Thus, Ishikawa *et al* [14] used Si/PSi (silicon on porous silicon) as substrate material, as the porous silicon layers (consisting of sponge and rodlike structures) are well capable of reducing wafer bending and residual stress in GaN films. But sole use of PSi results in small pits and cracks in the GaN epi from the porous substrate. This was reduced [14] using a Si deposition over the PSi prior to AlN nucleation layer growth. Although large biaxial stress is present during the initial growth of GaN films, later it was compensated as the

PSi deformed itself to reduce the thermal mismatch. Even though the growth rate was demonstrated a lot higher than the MBE in case of MOCVD, the crystalline quality of the grown GaN epilayer was poor due to the interfacial reactions between the films and the substrates at the high growth temperatures. This interfacial phenomenon shows up when the substrate temperature is above 300^{o}C. In addition, due to high growth temperature, there is a very high chance of Si carry-over, or autodoping, from substrate to the growing film [11]. This results in lower breakdown voltage of the device fabricated from the affected epi.

2.3 Low temperature growth processes

In search for a low temperature growth procedure for III-nitrides, pulsed laser deposition(PLD) was introduced as a suitable growth technique [15], [16], since laser irradiation provides high kinetic energies to the film precursors. Kobayashi's group has demonstrated the PLD technique in epitaxial deposition of III-nitride films on ZnO and $LiGaO_2$ [16], [17] substrates. Although PLD enables low temperature growth, the growth rate at this process is very low, around 100nm/h, which forces researchers to look for alternative low temperature growth processes with higher growth rates. The pulsed electron deposition (PED) process, which is similar in principle as the PLD process, but instead of producing a pulsed laser beam it produces a high energy pulsed electron beam through a channel spark discharge. The mechanism of this high energy electron pulse formation will be discussed in the next chapter. It was first reported by Porter *et al* at NCSU [18] on the use of PED process in depositing ZnO films on sapphire substrates. PED also offers higher production throughput than PLD, and thus can be considered a tool for mass production.

The effectiveness of both PED and PLD processes depends on the energy absorbed by the plasma plume rather than the target. This can be a problem for PLD because the quantity of the ablated material is highly sensitive to the optical absorption coefficient of the target material and the plasma plume consumes a big portion of energy from the beam. Thus, the beam ultimately has very low energy to ablate the target as the plume behaves like a shield for it. In the PED process, on the other hand, ablation is independent of the optical properties of the target material as the e^- beam-solid and the e^- beam-plume interaction is not similar to the laser-solid and laser-plume interaction. Additionally, the surface penetration depth in PED is an order of magnitude higher than the absorption depth of the laser radiation on the target. This allows evaporating at least ten times as much mass as that obtained from ArF based excimer laser PLD (0.6 µg/pulse). Thus it appears that PLD and PED, both based on the same principle of evaporation through high energy pulses, are good candidates for deposition of wide bandgap materials. The short laser pulse in PLD (about 10-100 ns) facilitates high power density at the target surface where the beam generates rapid non-equilibrium heating processes, forming a stoichiometric plasma plume [19]. PLD equipment costs, however, are very high because high power excimer lasers are expensive and costly to maintain. By contrast, the PED technique is potentially a more cost-effective solution for growth of wide bandgap semiconductors.

Thus, if we summarize the advantages of PED over PLD, we have:

1. The PED process can be used to grow wider bandgap materials such as AlN, CaF_2, and BN since the incoming high energy electrons collide with the deep level electrons of the target material atoms and stop at a penetration depth,

D, which is determined by material density and electron energy. On the other hand, the excimer laser driven PLD process shoots laser pulses of 5.0 eV (248 nm wavelength), which is not sufficient to excite electrons across wider bandgap materials like AlN, which has a bandgap of 6.2 eV.

2. With PLD, the produced plasma shadows the incoming laser pulses due to laser-plume interaction and reduces the effective laser intensity on the target surface. In PED, the incoming electrons do not interact significantly with the plume and effective power delivered to the target is much higher as compared to PLD.
3. In PED, the electron gun is physically present inside the deposition chamber. But in PLD the laser source is outside the chamber laser pulses pass through a quartz window. This presents a frequent maintenance problem since over time this window accumulates deposited material, which absorbs a portion of the incoming laser pulse power and reduces the effective laser intensity on the target surface.

2.4 Pulsed electron beam deposition (PED) process

Figure 2.1 presents a simple schematic of the PED process. The principle part of this setup is a high energy electron gun. The pulse parameters are presented in Table 2.1 [20]. High energy electron pulses are obtained in two ways: pseudo spark and channel spark discharge. GaNesis, the PED system at University of Oklahoma, uses a Neocera PEBS-21 electron gun, which uses the channel spark technique, a conversion efficiency of 25-30% is achieved in electrical energy conversion. This is much better that the 4% efficiency obtained for the peudo spark technique. With no magnetic lens, the PED

electron beam focusing system is simpler than what is used in electron microscopes. The acceleration of the electrons is induced by a high potential difference applied between the

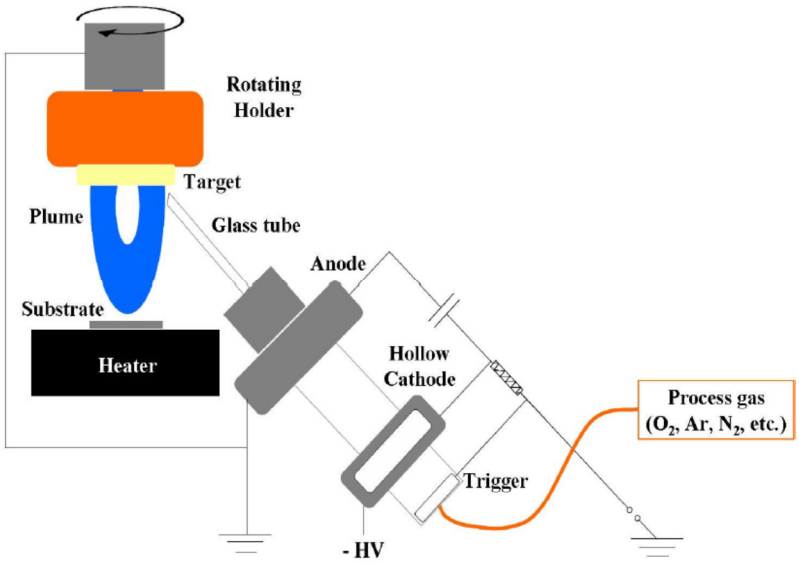

Figure 2.1: Schematic of PED system.

Table 2.1: PED source (PEBS-21) specifications

Maximum discharge voltage	20 kV
Electrical conversion efficiency	30% (maximum)
Energy/pulse	0.1-0.8 J
Operation pressure range	6-12 mTorr
Pulse frequency (maximum)	10 Hz at ≤ 15 kV and 5 Hz at 20 kV
Process Gas	O_2, N_2, Ar etc.
Pulse width	Variable 50 ns – 5 µs
Maximum pulse energy density	10 J/cm^2

hollow cathode and the target holder which acts as a ground. The electron flux extracted by the accelerating potential passes through a 4-6 mm diameter ceramic/glass tube between the hollow cathode and the target holder which acts as a ground. The electron flux extracted by the accelerating potential passes through a 4-6 mm diameter ceramic/glass tube towards ground, the target. In the hollow cathode electrical energy is

stored in a variable number of high voltage ceramic capacitors which are capable of delivering pulses of 10 J (maximum). Pulse discharge is activated by an external control circuit with variable pulse frequency ranging from 0-10 Hz. The current density obtained in this process is very high (~ 10^6A/cm^2) that results in very high peak power density of up to 1.3 x 10^8 W/cm^2 during the 70 – 100 ns pulse duration. Typically the process is very simple:

- High energy electron beam is pulsed on the target material at 40^o angle with respect to normal. Interacting with the target, material is ablated and a high temperature plasma is produced. The plasma plume extends from the target surface towards the substrate.
- The substrate is mounted on the heater at a vertical distance of 5-6 cm from the target. Ablated target material can thus reach the substrate and form a deposited layer.

2.5 Plasma formation in PED process

In the PED process, the incident electron energy of 5-20 kV is sufficient to excite atoms leading to plasma formation, as the beam energy is well above the threshold potential for ionization. As mentioned earlier, fast electrons collide directly with the deep level electrons of target material atoms, experience a broad-angle scattering and eventually stop at a certain penetration depth. This absorption range is expressed by the following equation [20]:

$$D\ (\mu m) \approx 5.37\ \varepsilon\ (1 - \frac{0.9815}{1+0.0031\varepsilon})\rho^{-1} \qquad (2.1)$$

Here, D is the absorption range, ε is the electron energy, and ρ is the target material density. Figure 2.2 [21] shows the penetration/absorption range to be 0.5 – 2.0 μm for a

typical PED electron beam energy of 10 – 15 keV. Even for dense materials (such as $YBa_2Cu_3O_x$, YBCO, with ρ = 6 gm/cm^3), the penetration range of ~1.0 µm is greater than the typical depth of ~0.2 µm for laser ablation, using a 248 nm KrF excimer laser at 5J/cm^2 [22].

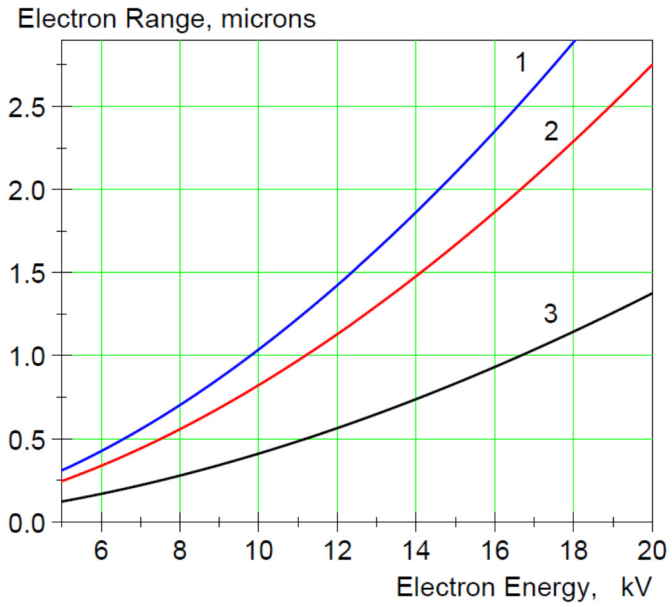

Figure 2.2: Calculated penetration depth (range) of energetic electrons in Si (1), Al_2O_3 (2), and $YBa_2Cu_3O_x$ (3).

Figure 2.3 [20] shows the schematic of the PED process in four different phases. Phase 1 is determined by the pulse duration. In this stage, most of the beam energy is transformed into the internal energy of the atoms in the plasma. This includes energies of evaporation, ionization and thermal energy of target material atoms as well as the energy of electrons in the plasma. Typically the plasma length is below 0.1 mm during this phase. As shown in the phase 2 of Figure 2.3, under high internal pressure, the plasma layer ejects itself perpendicularly from the target surface. The plasma does not get impacted by the process gas pressure because the plasma pressure is orders of magnitude higher than the process gas pressure in the deposition chamber. The plasma

experiences continuous acceleration by the pressure gradient supported by relaxation of the atoms. During phase 2, the original energy spectrum of the plasma flux is formed, with a typical plasma size

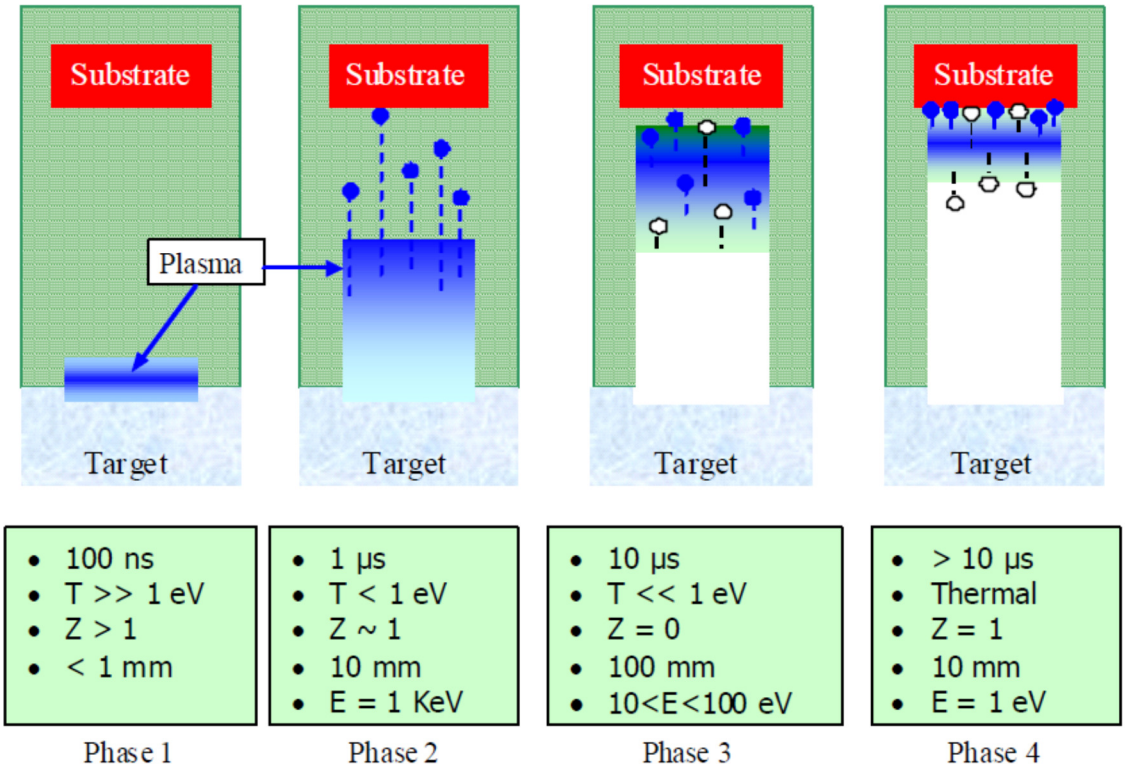

Figure 2.3: Schematic representation of pulsed electron beam deposition process.

being in the order of several times of the electron beam spot size on the target surface. This vertical expansion of the plume is of ~10 mm in length, when process is done in vacuum (pressure<10^{-6}Torr), as shown in phase 2.

If the process is done in a gas background, i.e., UHP N_2, Ar or O_2, as shown in phase 3, the flux atoms collide with the process gas atoms. As a result, the initial energy spectrum of the atoms in the plasma evolves on a characteristic length scale related to the length scale of the mean free path at a given pressure. If the quantity of the ablated atoms is comparable to the number of gas atoms in the mutual hydrodynamic

movement, this would ultimately drive most of the gas atoms towards the substrate leaving behind a gas-rarefield region as shown in phase 2. Simultaneously, as the entire ensemble decelerates, kinetic energy of both the target and the gas atoms decreases. In the last phase (phase 4), the directional velocity of the plasma flux becomes comparable to the thermal velocity of its particles (the flux transforms from supersonic to sub sonic states), plasma expansion stops yielding a visible plume and becomes nearly isotropic.

2.6 Review: GaN growth using PED process

There has not been a lot of work done on growth of WBG materials using PED compared to the application of PLD for the same objective. However, a few recent works have presented promising results in this regard. Ohta *et al* [23] have deposited GaN on *c*-plane sapphire, 6H-SiC (0001) and ZnO (0001). They attained a very low temperature epitaxial growth of the GaN films at around 200^{o}C (on ZnO substrate) after a ultrahigh vacuum (8.0 x 10^{-10}Torr) base pressure. 99.999% pure GaN (produced by HVPE) was used as a target material. The PED electron source was operated at 15 kV at 5-15 Hz with N_2 gas elevating the system pressure to 20 mTorr. The growth rate for deposited GaN films was 500 nm/h. The researchers have found that direct growth of GaN on Al_2O_3 and 6H-SiC results in a clear 3 x 3 and 1 x 1 surface reconstructions, respectively, as measured using reflection high energy electron diffraction (RHEED) (Figure 2.4) [23]. This phenomenon is considered as a contribution of the two different polarities of GaN films: N-faced and Ga-faced, respectively.

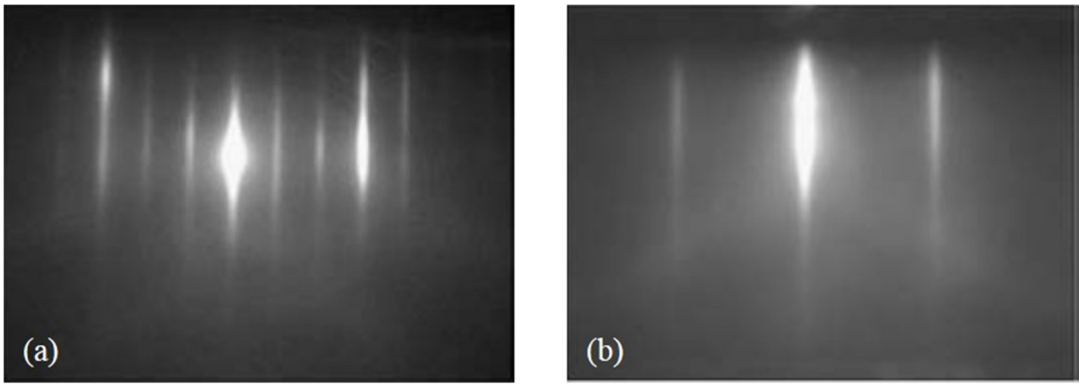

Figure 2.4: RHEED patterns of GaN films grown on (a) Al_2O_3 and (b) 6H-SiC.

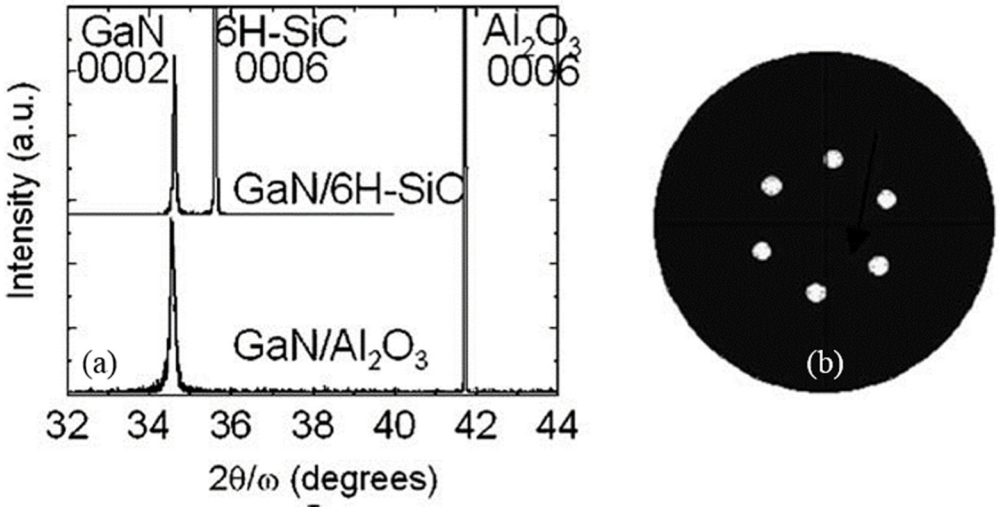

Figure 2.5: 2Θ/ω XRD curves, and (b) a typical GaN (10-12) pole configuration.

XRD curves, Figure 2.5(a) [23], show that the FWHM value of the 200 nm GaN (0002) is 147 arcsec, grown on 6H-SiC.Typically, TEM measurements are done for the estimation of the dislocation densities, but in this work, they depended on the analytical method proposed by Lee *et al* [24], which determined the screw dislocation densities to be approximately 5 x 10^7 /cm^2 from the FWHM of the rocking curve data. Figure 2.5(b) [23] describes the six-fold rotational symmetry indicating the absence of 30^o rotational domains and this yields a typical pole figure for GaN (10-12). The RHEED patterns, in Figure 2.4, reveals that the surface of the grown GaN films are 2D surfaces. *In situ*

AFM measurement of the grown surfaces, verified this claim (Figure 2.6 [23]). After the growth of 3 nm of GaN on 6H-SiC, the AFM measurements show that the root-mean-square (rms) surface roughness is 1.6 nm, which describes 3D growth of the GaN films. Gradual growth and simultaneous measurement of the GaN surface showed that up to the thickness of the GaN layer to be 200 nm the RHEED patterns showed sharp and streaky lines along with increment in rms roughness up to 4.7 nm; on the other hand, while

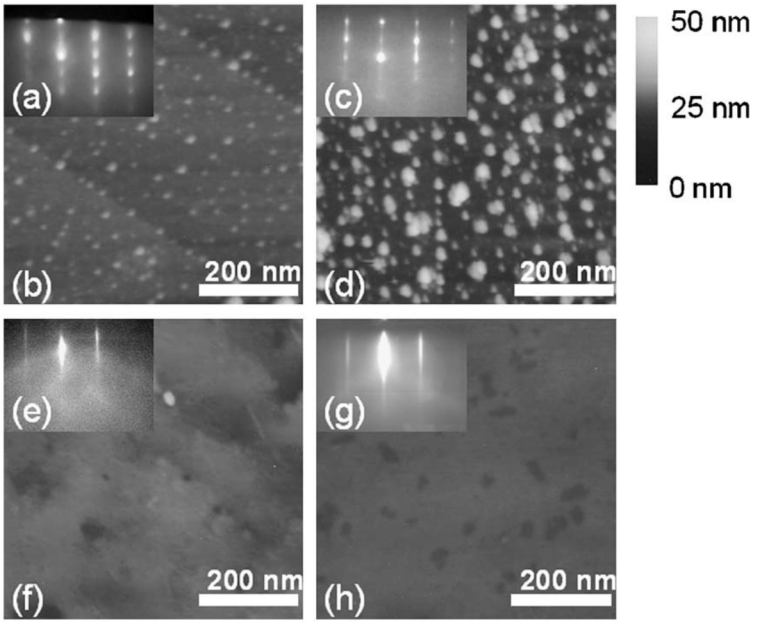

Figure 2.6: Time evolution of RHEED patterns and AFM images for GaN films grown on an atomically flat 6H-SiC substrate: (a), (b) 3 nm; (c), (d) 10 nm; (e), (f) 50 nm; and (g), (h) 200 nm.

attaining 200 nm film thickness the rms roughness jumped down to 0.5 nm and the RHEED patterns resemble the same as shown in the Figure 2.4(b).

The room temperature photoluminescence (RT-PL) spectrum of the 200 nm GaN/6H-SiC film shows that near-band-edge emission takes place around 360 nm (Figure 2.7). This also explains that the GaN grown using PED is optically active. This phenomenon is also observed for GaN/Al_2O_3 with a clear near-band-edge emission.

Ohta *et al* [23] attempted to grow GaN on 6H-SiC, Al_2O_3, and ZnO at different descending temperatures to study the effect of substrate temperatures. For 6H-SiC and Al_2O_3, growth temperature could be lowered to approximately 400^oC while for ZnO substrate the lowest growth temperature was 200^oC. They predicted that due to the less amount of lattice mismatch in ZnO compared to Al_2O_3 and 6H-SiC with GaN, a lower growth temperature yielded this film growth even at 200^oC. The x-ray photoelectron spectroscopy (XPS) of this GaN/ZnO film (Figure 2.8) shows that the Zn atoms are present in detectable amount

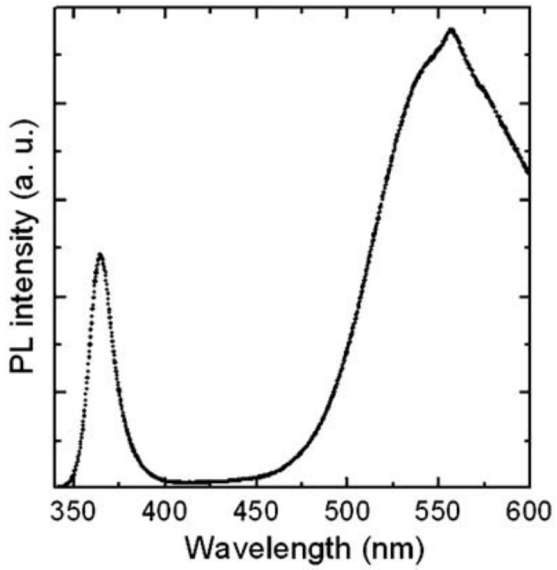

Figure 2.7: Room temperature photoluminescence for 200 nm GaN/6H-SiC

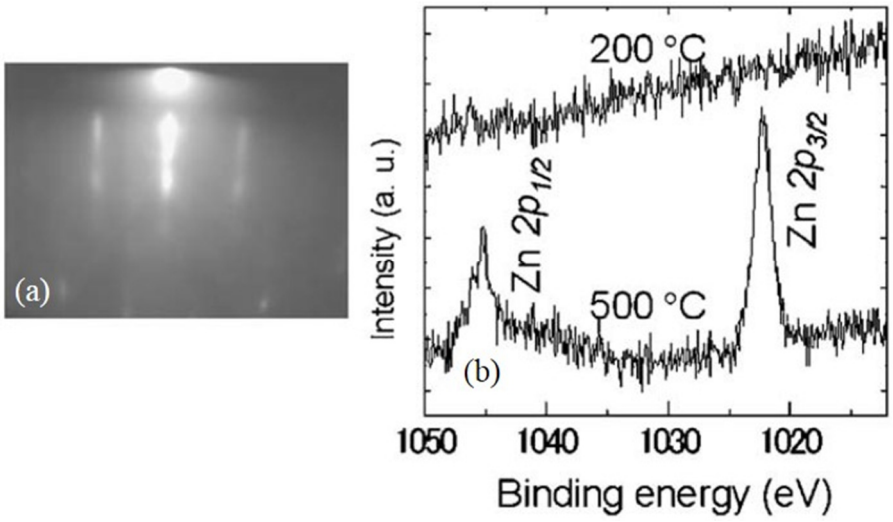

Figure 2.8: RHEED pattern for a GaN/ZnO sample grown at 200°C, (b) Zn2p XPS spectra for the GaN films grown at 500° and 200°C.

in the GaN films grown at around 500°C, while for the films grown at 200°C, the Zn quantities are negligible. This shows that a low temperature PED growth of GaN on ZnO is free from the intermixing reactions at the GaN-ZnO hetero interface.

2.7 Review: ZnO growth using PED

Tricot *et al* [25] used PED to grow ZnO and investigated the morphological, structural, optical and electrical properties of the films. They compared PED with a commercial PLD process. ZnO was grown on *c*-plane sapphire in 1.4×10^{-2} mbar Ar environment at 700°C. Electron pulses were shot at 1Hz rate with discharge voltage varied between 14-16 KV. Using RBS, the thickness and the stoichiometric ratio of Zn and O in the film was analyzed, and it was determined that PED grown samples were free from any Ar (from the process gas environment). This makes the PED more attractive as compared to the sputtering process [26], which showed Ar incorporation during the growth process. In addition, ZnO growth using PLD process requires an oxygen partial pressure for growth, otherwise the samples result in Zn rich condition,

which is not observed in PED grown samples in [25]. Also they reported [25] 10 times higher growth rate in PED compared to that of the PLD process. AFM measurements of the samples confirm a smooth surface with 4.5 nm rms roughness.

Powder diffraction and rocking curve XRD confirmed *c*-plane oriented ZnO films with some polycrystallinity, evidenced by a large rocking curve FWHM of 0.65^{o} (2,340 arcsec). Nevertheless, this material had better crystallinity than samples grown with PLD in the same process environment [25]. They verified the epitaxial growth of ZnO on *c*-plane sapphire using pole figure measurement using electron back-scattered diffraction (EBSD). Figure 2.10 [25] shows the six well defined poles at a declination angle of $\psi=32.5^{o}$ indicating the existence of an epitaxial relationship between the ZnO film and substrate.

Electrical and optical properties are also reported in [25]. Room temperature Hall measurements confirms the grown films as *n*-type with high amount of charge carriers (n_e = 3.4 x 10^{19} cm^{-3}) comparing to that of the PLD grown ZnO samples (~$10^{16}cm^{-3}$) [27]. However, the mobility is quite modest in the PED grown ZnO samples, ~11.65 cm^2/V-sec, which is significantly lower than the mobility of the bulk ZnO crystal (205 cm^2/V-sec [28]. The authors [25] reported that the high carrier density yields lower resistivity (~10^{-2} Ω-cm) originating from the better crystallinity and film stoichiometry. Optical absorption spectroscopy confirms the thin film ZnO band gap to be 3.28 eV, slightly red shifted from the bulk ZnO band gap of 3.3 eV.

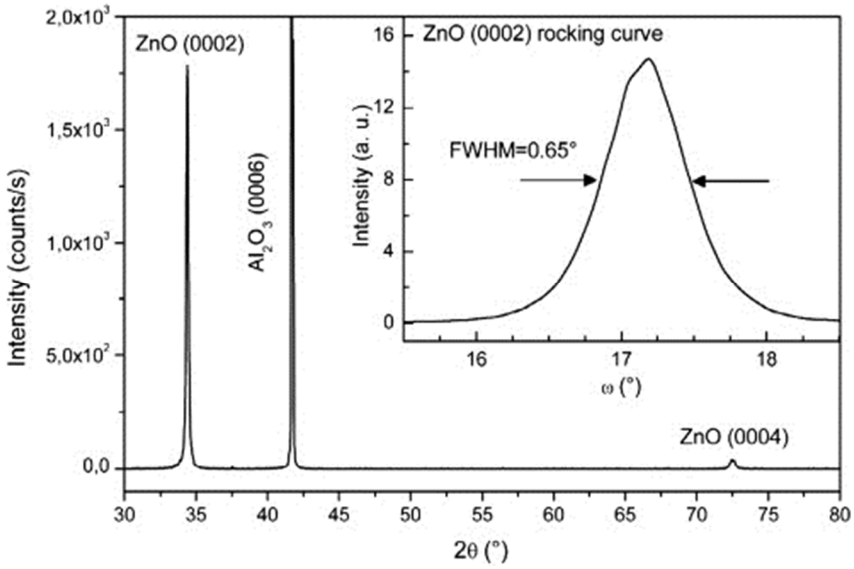

Figure 2.9: θ-2θ XRD diagram of ZnO thin film grown at 700°C on *c*-plane sapphire, The inset shows the corresponding rocking curves of the (0002) reflection.

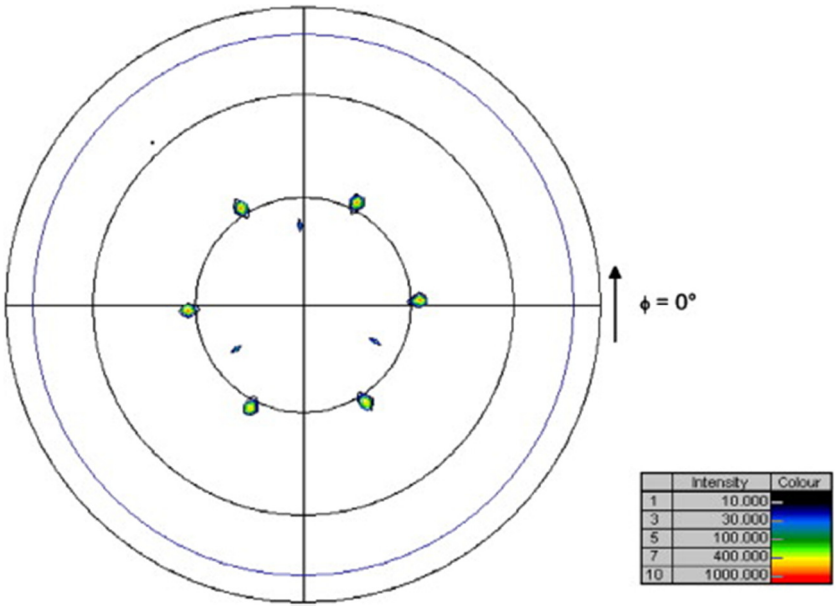

Figure 2.10: Al_2O_3 (01-18) and ZnO (10-13) pole figure of a ZnO film grown on *c*-plane sapphire.

2.8 Substrates for WBG III-nitride and II-oxide growth

Growth of III-nitrides and ZnO suffers from the availability of a well matched substrate material in terms of lattice constant and thermal expansion coefficient. In addition, cost also plays a vital role in the consideration. The best matched commercial substrate, i.e., 6H-SiC, is very expensive as a 2" wafer costs around 2,000 USD. Other widely used substrates are sapphire, silicon, bulk GaN, bulk AlN and bulk ZnO etc. Figure 2.11 [29] shows the lattice constants of the substrate materials widely used so far, providing a qualitative idea of the lattice mismatch between epilayer and the substrate.

Although it appears that ZnO has a better lattice match (a_{ZnO} = 3.25Å) with GaN (0002) (a_{GaN} = 3.189Å), there are several problems employing ZnO as a substrate material

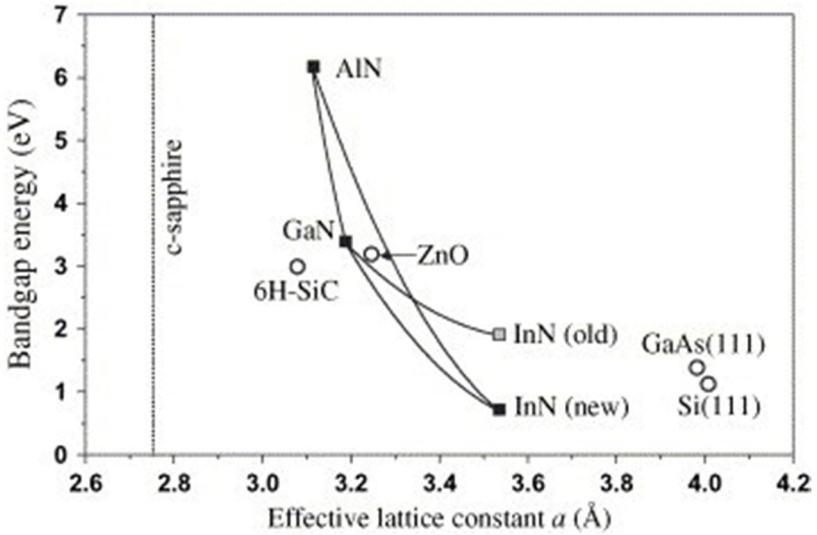

Figure 2.11: Bandgap energy vs. lattice constants of III-nitrides, ZnO and their most common substrate materials.

for GaN growth such as lack of a good surface morphology as it negatively impacts the achievement of high-structural-quality of group III-nitride films [30]. Another problem is the high reactivity between ZnO and GaN which ultimately forms a thick interfacial

layer of Ga_2ZnO_4 resulting in a poor epitaxial layer quality. Sapphire (Al_2O_3) has been widely used for III-nitride and ZnO growth. But, for bulk GaN growth, sapphire suffers from the large amount of threading dislocation densities resulting from lattice and thermal mismatch.

Si(111) has been under extensive research to get established as a potential candidate in terms of cost and integration of GaN devices with the current silicon industry. As explained earlier, epilayers grown on silicon suffer from high lattice and thermal expansion mismatch. Although many efforts have been given to grow crack-free epitaxial layers with low dislocation densities on different substrates, so far, the best lattice matched substrate for wurtzites (also thermally favorable) has been 6H-SiC, which is not a cost-effective solution. This promotes the use of silicon as a substrate. But, additional means are required to engage silicon in the growth process of WBG materials.

Table 2.2: Properties of potential substrates for III-nitride and ZnO epitaxy.

	Sapphire	4H-SiC	6H-SiC	Si	ZnO	GaN (epi)
Lattice Constant (Å)	a = 4.765 c = 12.982	a = 3.073 c = 10.053	a = 3.0806 c = 15.1173	a = 5.43102	a = 3.2496 c = 5.2065	a = 3.189 c = 5.185
ΔLC (%a)	-13.8 (after 30° rotation)	3.64	3.39	-17	-1.9	0
Thermal Expansion Coefficient (K^{-1})	$5x10^{-6}$		$4.46x10^{-6}$	$2.616x10^{-6}$	$4.31x10^{-6}$	$5.59x10^{-6}$
ΔTEC(%)	11		20.2	53.2	22.89	0
Thermal Conductivity ($Wm^{-1}K^{-1}$)	25	370	490	130	60-100	130

Thermal Diffusivity (m^2s^{-1})		$17x10^{-5}$	$22x10^{-5}$	$8.8x10^{-5}$		$43x10^{-5}$
Density (kgm^{-3})	3980	3210	3210	2329	5610	6150
Melting Temp (K)	2303	3103	3103	1687	2633	2773
Energy Bandgap (eV)	8.1-8.6	3.26	3.02	1.124	3.3	3.4
Young's Modulus (GPa)	452-460			165.6		181
Poisson's Ratio	0.25-0.30	0.183-0.192		0.218	0.358	0.352
Electron Mobility ($cm^2V^{-1}s^{-1}$)		1000	400	1430-1448	2000 (peak)	
Hole Mobility ($cm^2V^{-1}s^{-1}$)		115	101	473-495	0.1-50	

A widely used work around is to use a sacrificial buffer layer prior to epilayer growth followed by a suitable epitaxial layer lift-off process.

2.9 Buffer layer strategy

Due to significant amount of lattice mismatch (17%) between *c*-plane GaN and Si(111), a buffer layer strategy has been applied to reduce the strain on the epitaxial GaN layer. Watanabe *et al* [31] first proposed the idea of growing a thin AlN buffer layer over Si before GaN deposition after the idea of Takeuchi *et al* [32], which involved the use of expensive SiC as the buffer layer material. They used and atmospheric pressure MOVPE growth process. As a buffer layer, AlN has some significance: (i) it possesses the similar wurtzite structure as the GaN crystal structure, (ii) when the AlN buffer layer is grown on Si (111) the tensile strain between GaN and Si is converted to compressed strain, and (iii) AlN prevents the direct contact of Ga

atoms with that of the Si atoms, since a SiN layer forms on top of the Si substrate as a result of nitridation.

There have been reports of growing high temperature AlN (HT-AlN) and low temperature AlN (LT-AlN), both of which have their own advantages. When AlN is grown on Si(111) [33], AlN layer suffers from the tensile strain from the Si layer, which can be reduced through decreasing the AlN growth temperature, and this results in GaN growth on LT-AlN under compressive interlayer-induced strain. Table 2.3 [33] presents the results in optimizing a growth temperature for LT-AlN buffer layer for GaN and AlGaN growth.

Table 2.3: Wafer curvature, AlN IL deposition temperatures, total stress, and lattice constants of GaN and $Al_{0.21}Ga0_{.79}N$ epilayers grow on AlN interlayer.

T_{AlN} (^oC)	Curvature radius (m)	Total stress (GPa)	*a*-AlGaN (Å)	*a*-GaN (Å)
630	14.7	-0.01	3.1653	3.1899
900	7.9	0.46	3.1665	3.1923
1145	2.9	1.13	3.1923	3.1923

On the other hand, better crystalline quality of the grown GaN layers is observed when HT-AlN is used as the buffer layer by Gong *et al* [34]. They reported that the incorporation of LT-AlN interlayer on both Si(100) and Si(111) substrates results in poor GaN epitaxy as a consequence of the imperfect microstructure of the LT-AlN buffer layer. The imperfect microstructure of LT-AlN buffer layer is a result of the large lattice mismatch between film and substrate and the low surface diffusivity of the adsorbed radicals at a low growth temperature. They reported the effect of HT-AlN buffer layer grown at 1000^{o}C on silicon and analyzed the effect of buffer layer thickness on the grown GaN epitaxial layer. It was reported that with a 200Å buffer layer the

crystallinity (Figure 2.12) of the GaN film was improved compared to 100Å and 1000Å thick buffer layers.

Thus it appears from research that LT-AlN helps to prevent cracking of the epitaxial GaN layer, while the use of HT-AlN buffer layer results in better crystalline quality of the GaN epi. Arslan *et al* [35] used the advantages from both of these techniques by having a LT-AlN (grown at 700^{o}C) sandwiched between two HT-AlN (1100^{o}C) layers and then growing a graded $Al_xGa_{1-x}N$ layer before the desired GaN epilayer is deposited. This graded $Al_xGa_{1-x}N$ layer was introduced to reduce further the cracking in GaN layer, which was present even though the HT-AlN stack was thicker than 400 nm. The $Al_xGa_{1-x}N$ composition was reduced from x= 0.64 to 0.22 (in 7 steps) to match up well with the GaN layer on top. The PL emission of all the samples are reported to be in the range of 3.387 and 3.394 eV, very close to bulk GaN PL emission calculated at 3.4 eV. It was reported that the samples grown with 400 nm HT- AlN buffer layer showed better optical properties (FWHM of near band edge PL emission is 58 meV) with a low dislocation density (6 x10^{8} cm^{-2}).

A similar LT-ZnO buffer layer strategy was adopted by Xiu *et al* [36] for ZnO epitaxy on silicon. They did a temperature dependent buffer layer study and reported that a ZnO buffer layer of 1.1µm thickness grown at 450^{o}C works better than other

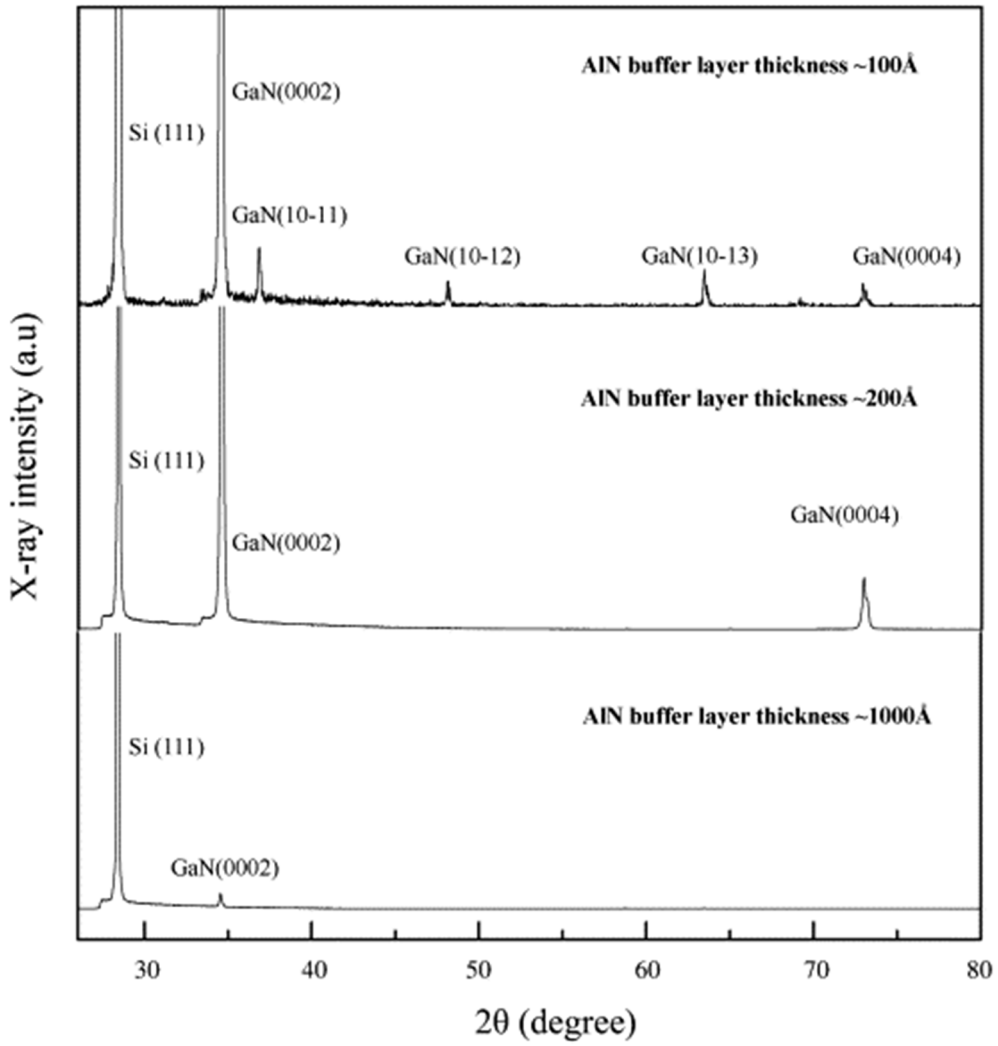

Figure 2.12: The X-ray diffraction patterns of HT GaN films grown on the HT AlN-coated (1 1 1) Si substrates with AlN buffer layer

temperatures to grow a ZnO epitaxial layer at 550^{o}C. They performed RT-PL, powder diffraction and Raman spectra studies confirming the better performance of a 450^{o}C buffer layer.

2.10 Summary

A comparative study of the low temperature growth processes (PLD and PED) for WBG material is presented in this chapter. The plasma formation mechanism in PED is studied in detail followed by review on application of PED for III-nitride and II-

oxide film growth. Considering the lattice and thermal mismatch issues, buffer layer strategies for WBG material growth on silicon have been presented. The next chapter will focus in detail on the plasma optimization procedure for the PED system.

Chapter 3 : PED growth process, plasma generation, and optimization

3.1 Motivation

The previous chapters discussed potential applications for WBG materials and various thin film growth techniques. This chapter will explain step-by-step growth procedures for the PED process. A detailed analysis of plasma generation and optimization will be followed by a summary of the material characterization techniques used in this research.

3.2 System description

Figure 3.1 shows the pulsed electron beam deposition system, named here as GaNesis, after assembly and installation in the University of Oklahoma cleanroom. The system comprises of four major components:

(1) Custom designed vacuum chamber (Designed by OU ECE, made by MDC Vacuum, Hayward, CA).

(2) High energy electron gun (PEBS-21, Neocera LLC).

(3) Target manipulator (Thermionics LLC).

(4) Substrate manipulator (Thermionics LLC).

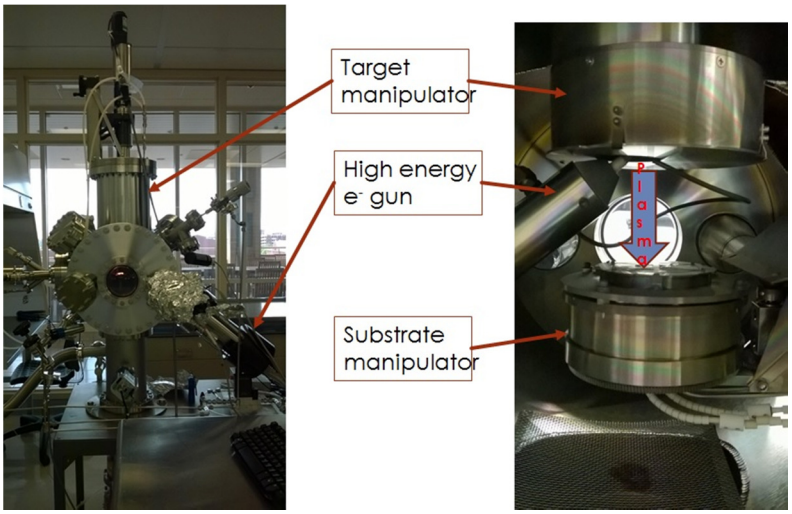

Figure 3.1: Pulsed electron beam deposition (PED) system: GaNesis.

The chamber is a 14" diameter cylindrical chamber made of type 304 stainless steel, providing capabilities to attain a vacuum of 10^{-7} Torr using an Ebara 300W Turbo pump (300 l/Sec) backed up by an Alcatel mechanical roughing pump. After sample loading, the roughing pump attains a chamber pressure of ~10^{-3} Torr and then turbo pump operation is initiated (maximum speed of 48,000 rpm). Overnight pumping is required to attain a base pressure of 10^{-7} Torr. The chamber is equipped with multiple vacuum compatible viewports to observe the condition inside. Gas feeding is controlled using one Alicat mass flow controller to control the process pressure. A second gas inlet (?) controlled by a Pfeiffer needle valve feeds gas into the chamber near the tip of the electron gun. The distance from the gun tip is about 14 mm, as recommended by the electron beam gun manufacturer Neocera LLC.

The target manipulator is assembled on top of the chamber, facing down vertically, with the capability of housing four 1" diameter x 0.250" thick targets. For this research work three different sintered target materials were used: 99.8% pure AlN (from Kurt J Lesker, PA), 99.99% pure GaN (from Superconductor Materials, NJ), and

99.9% pure ZnO (from Kurt J Lesker, PA), with one spot not used so far. The manipulator is cooled by house water, maintained at 24^{o}C by the OU Clean room Facilities, running at an inlet pressure of 20 PSI. The substrate manipulator is usually stationed 5 cm away from the target surface (the distance can be changed for better plasma production). The distance between the target and substrate manipulator can be adjusted by moving the target manipulator position vertically. This helps to have a vertical distance of 3.5–9 cm between target and substrate. This wide range allows studying different parameters for growth, especially growth rate change and stoichiometry studies with change in target-substrate spacing. The substrate platen was modified so it can simultaneously house four different substrates (each of 1cm x 1cm dimension). Figure 3.2 shows the modified Ni-Cr platen stage. This improves research efficiency since growth of a specific thin film on four different substrates with the same growth conditions can be performed simultaneously. The substrate manipulator is designed to rotate continuously up to a rotation speed of 30 rpm. With high intensity incandescent lamps located below the substrate holder it can heat up the substrates up to ~750^{o}C, a limit that can be adjusted with a potentiometer located inside the substrate heater controller box. However, for equipment safety, it is advised to contact Thermionics technical support before such an operation is executed. Two 500W Ta filaments are used to heat up the substrates. The maximum filament temperature achieved so far is 1230^{o}C. However, due to a recent maintenance, for the use of one additional barrel connector ensuring manipulator operation, the maximum temperature has been reduced to 1130^{o}C.

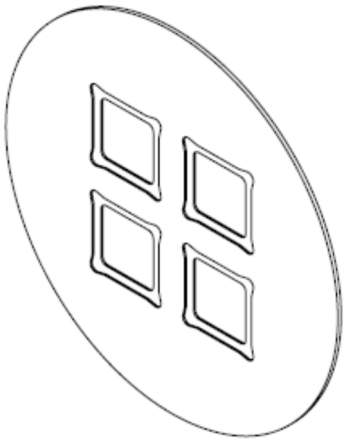

Figure 3.2: 2" Ni-Cr alloy platen, modified to house four 1cm x 1cm chips.

Substrate surface temperatures were calibrated using a type-k thermocouple on the substrate surface. The highest temperatures for sapphire and silicon were 750^{o}C and 720^{o}C, respectively.

3.3 Substrate preparation

Four different substrates were used:

1. Double side polished *c*-plane sapphire
2. *n*-type Silicon (111)
3. *p*-type Silicon (100)
4. The other samples were 3^{o} off–cut Si(111) (*p*-type) and 2 nm Ge coated 3^{o} off–cut Si(111) (*p*-type) wafers, supplied by Amethyst Research Inc. of Ardmore OK. Also used were CaF_2/Si(111) and PbSe/BaF_2/CaF_2/Si(111) samples grown by MBE. Growth of wide bandgap materials using IV-VI semiconductor buffer layers on silicon is potentially promising because of the possibility of the IV-VI material to function as a compliant material that can absorb the thermal expansion

mismatch strain between the silicon substrate and the WBG material. Further discussion of this possibility will be presented in Chapter 5. The substrate preparation procedure is explained below for different the kinds of samples mentioned above. A diamond scriber from Dr. Zhisheng Shi's laboratory at OU was used to cut the sapphire, silicon, and coated silicon samples into 1 cm x 1 cm chips.

3.3.1 Sapphire cleaning

The chips were first blown with UHP N_2 then submerged in running DI water (room temperature) for 5 minutes. They were then rinsed in acetone and methanol for 5 minutes each in an ultrasonicator. After methanol rinsing the chips were dipped in DI water again for 30 seconds then dipped in a sapphire etching solution (1:3 mixture of H_3PO_4:H_2SO_4) for one minute. The chips are then rinsed with fresh DI water, dried with UHP N_2, and put in the PED chamber for growth.

3.3.2 Silicon cleaning

The chips were first blown with UHP N_2, then submerged in running DI water (room temperature) for 5 minutes. They were then rinsed in acetone and methanol for 5 minutes each in an ultrasonicator. After methanol rinsing the chips were dipped in DI water again for 30 seconds then dipped into 25% HF solution for native oxide removal (for 2-3 minutes). The chips were then rinsed in fresh DI water, dried with UHP N_2, and put into the PED chamber for growth.

3.3.3 Cleaning of buffered silicon samples

The epi-ready silicon substrates, the ones with germanium, IV-VI semiconductor, or fluoride epitaxial layers, were kept in dry-boxes for avoiding contamination from atmospheric exposure. Before loading in the PED chamber, the substrates were simply blown with UHP N_2 and put in the PED chamber for growth. Care was taken not to expose the fluoride coated silicon substrates to the atmosphere for extended time periods since fluoride materials are hydrophilic and thin films of these materials can deteriorate especially if the humidity is high. On the other hand, the Ge coated silicon samples were first blow dried using UHP N_2, followed by 1 minute DI water rinsing. Then organic cleaning was done using 1 minute ultrasonication in methanol and again rinsed in DI water for 30 seconds. Then the chips were dipped in 25% HF solution for 30 seconds only, rinsed in DI water, dried using UHP N_2, and put into the PED chamber.

3.4 Target and plasma preparation

The sintered targets were mounted in the carousel in the target manipulator. Before plasma production there are few impact factors that need to be keenly observed to ensure the plasma quality and presence of reactive components in the plasma. It is advised [20] to optimize the plasma intensity to ensure significant presence of reactive components in the plasma for better growth. For this work an Ocean Optics spectrometer (UV4000) was configured to observe the plasma produced by electron beam ablation of the AlN, GaN, and ZnO target materials. Metal emission lines were selected to monitor the plasma condition during material growth. As the chamber is not equipped with a load lock system, the chamber is exposed to atmospheric condition

once it is opened for sample collection or sample loading. Thus, as the only precaution, the chamber is kept in strong positive UHP N_2 pressure (with a 1000 sccm UHP N_2 flow) once it is opened for sample exchange.

Once, the chamber is loaded with samples and pumped down overnight to reach a base pressure of ~10^{-7} Torr, the vitals (chamber pressure, background emission spectra) are recorded prior to growth. Substrate condition is obtained (temperature and rotation speed), and the target is lowered to gun proximity prior to its firing. A desired chamber pressure is monitored by the Pirani gauge as it serves as the pressure indicator in the gun proximity. Once everything is checked, the firing is initiated with a comparatively lower voltage and low pulse rate (8KV, 1Hz) to allow the gun to reach a steady state condition with the chamber environment, and also to help adjust the plasma intensity and plume structure to form. Once the plasma plume is generated, as suggested by technical expertise from the gun manufacturer Neocera LLC, the deposition starts as the substrates are exposed to the plasma. From experience, it was understood that having a high intensity does not always ensure a good thin film, as most of the time with a high intensity metal line, the semiconductor film appears to be metal rich after growth, as verified by the EDX analysis.

During the plasma optimization, the following factors were studied to help identify a specific parameter set that yields a considerably strong plasma:

- Chamber pressure in gun proximity (mTorr)
- Electron energy (in KV)
- Pulse rate (in Hz)
- Gap between gun tip and target surface (in mm)

The following section describes the emission spectroscopy of the ZnO target (as example) helping in optimizing the plasma for thin film deposition.

3.5 Plasma optimization

Figure 3.3 shows the plasma emission spectrum of a ZnO target (99.9% purity) after high energy electron (11KV at 3Hz) is bombarded on the surface in Ar environment (5.5 mTorr, chamber pressure in gun proximity) with a target to gun-tip distance of 2 mm. The spectrum was obtained using an Ocean Optics USB4000 spectrometer with an observation range from 200-1100 nm. As observed, there are distinct spectral lines in the plasma. Using the National Institute of Standards and Technology (NIST) database [37], different atomic species were identified. Optimization of the plasma is performed using observing a few of the peaks originated from the electron ablated plasma.

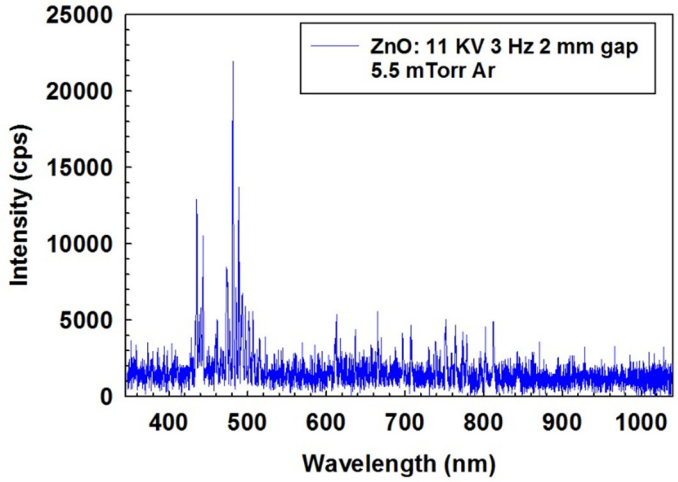

Figure 3.3: Emission spectroscopy of ZnO target after plasma generation using high energy electron bombardment.

Of the above four parameters (mentioned in Section 3.4), it appears that the pulse rate and the gun tip-target surface distance are the more impacting parameters, as

a minor variation causes more influence in case of these two parameters, other than the first two parameters. For the GaNesis system plasma optimization, chamber pressure ranges from 7-15 mTorr for UHP N_2 and 4.5-7 mTorr for Ar provide good plasma properties. Lower pressures than these results in suspension of gun operation causing "missing pulse" and the system interlock triggers in. Chamber pressures higher than this range will also suspend the gun operation in terms of "self-triggering" interlock. These ranges have been optimized and are applicable for all the target materials. The plasma generation and optimization has been found to be independent for AlN, GaN, and the ZnO target materials investigated so far.

The electron gun can fire electron pulses in the pressure ranges mentioned above from 8 KV to 20 KV energies. As observed, the most optimized and intense plasma was not produced at the highest pulse energy (as described in Neocera's technical manual [20]). A set of trials was employed to find the best pulse energy. After a process gas window is fixed along with a suitable pulse energy, the important task lies with fixing the other two parameters: pulse rate and gap between target and gun tip. Pulse rates was varied from 1 to 5 Hz, and vertical gap between gun-tip and target surface from 2 to 3.5 mm. The work routine for optimization is as follows:

(i) After setting the process gas pressure in the chamber in the optimized range, the vertical gap was set to a fixed value (this will be optimized later in step (iii)).

(ii) The pulse rate was varied from 1 Hz to 5 Hz, observing the atomic species. This step will help in fixing a specific pulse rate.

(iii) After the pulse rate is fixed, keeping the gun in operation, the vertical gap is varied from 2 – 3.5 mm, observing the changes in atomic species intensity, confirming balanced intensities from the components of the target.

According to the steps mentioned above, the optimization process was performed for ZnO plasma in Ar environment, at a chamber pressure of 5.5mTorr. Figure 3.4 shows the three different intensities of the two most prominent Zn emission lines, also responsible for the Zn reactants for ZnO thin film formation: ZnI (480.94 nm), Figure 3.4(a) and ZnII (491.16 nm), Figure 3.4(b) [38]. Attempts were made to distinguish the O reactive component at 844.41 nm [38], however, it was difficult to identify this component for the following reasons:

(i) The ablation was performed in Ar environment, and the Ar plasma generated due to interaction with the high energy electron shadows the O spectral lines in the infrared range as the intensities of Ar species are much greater in the same spectral range.

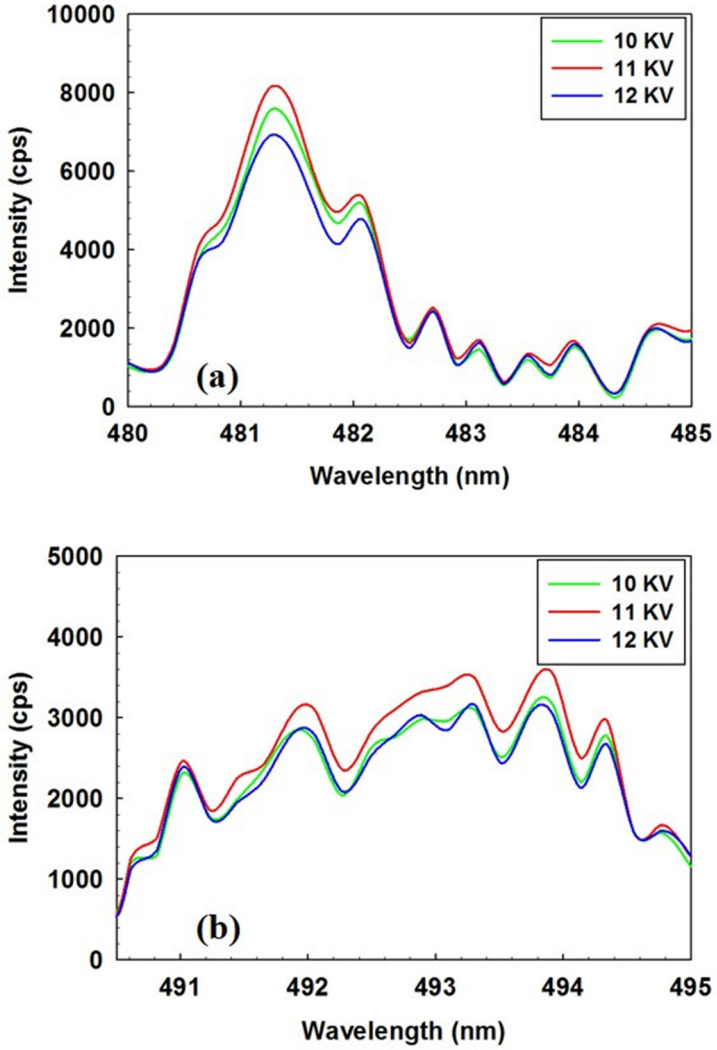

Figure 3.4: Emission spectroscopy, with voltage variation, of (a) ZnI peak (480.94 nm), and (b) ZnII peak (491.16 nm) at 5.5 mTorr Ar pressure, with 1 Hz pulse rate, 2 mm gap.

(ii) The recombination rate of O reactive components is very high so they recombine lot faster compared to the Zn components, after generation. So, the detection is difficult for these components, which requires high speed CCD facilities and also some other measures.

Thus, it appears that 11 KV electron pulses produce the more intensity in case of the Zn components in the plasma (Figure 3.4). So, in the optimization experiments, 11 KV pulses were used as the pulse voltage to generate ZnO plasma. The next parameter

to be analyzed is the pulse rate. Three different pulse rates were used: 1, 2, and 3 Hz. Figure 3.5 shows the effect of pulse rates on the two mentioned peaks of ZnI and ZnII.

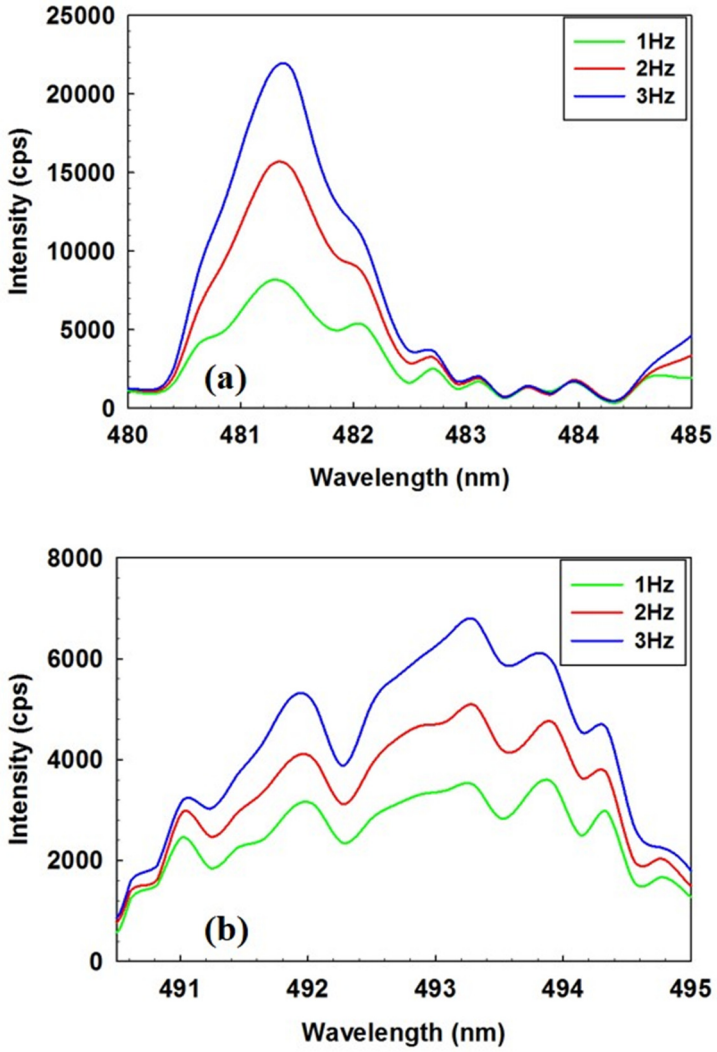

Figure 3.5: Emission spectroscopy, with pulse rate variation, of (a) ZnI peak (480.94 nm), and (b) ZnII peak (491.16 nm) at 5.5 mTorr Ar pressure, with 11 KV pulse, 2 mm gap.

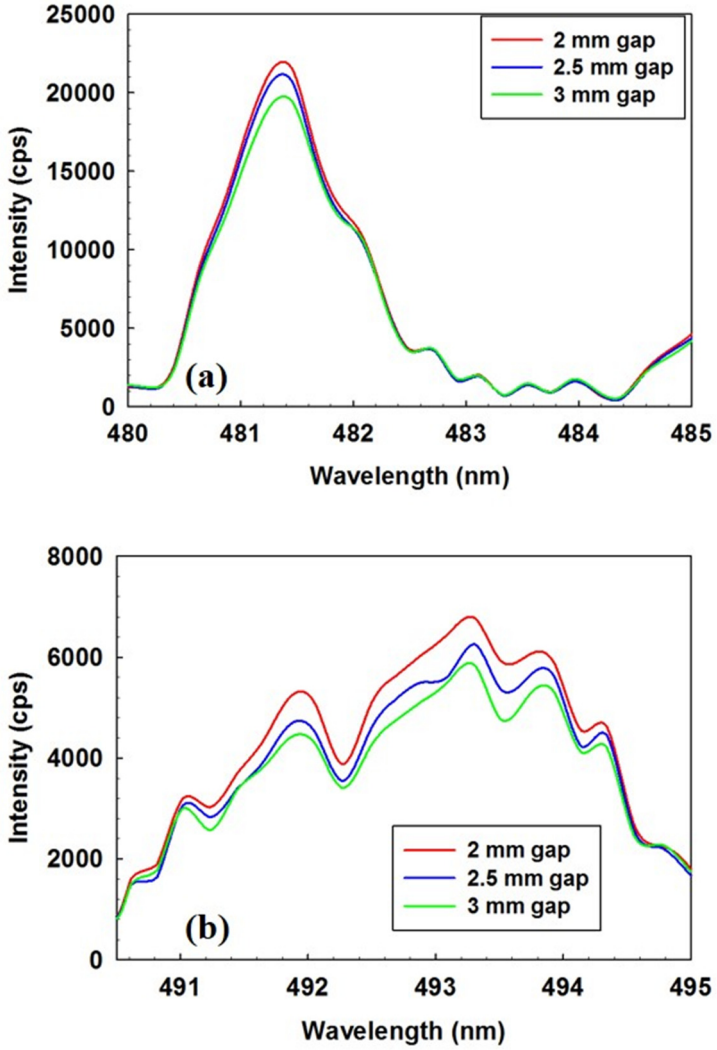

Figure 3.6: Emission spectroscopy, with vertical gap variation, of (a) ZnI peak (480.94 nm), and (b) ZnII peak (491.16 nm) at 5.5 mTorr Ar pressure, with 11 KV pulse, 3 Hz.

Now, after fixing the pulse energy and pulse rate in a specific chamber pressure, the remaining parameter to be optimized is the vertical gap between the electron gun tip and the target surface. Specified by Neocera LLC [20], this distance should vary between 2 to 4 mm. This gap was varied from 2 to 3 mm in an increment of 0.5 mm, observing the intensities of the peaks for the ZnI and ZnII atomic components. Figure 3.6 shows the observations in this regard.

Using the above optimization procedure, the obtained parameters are presented in the Table 3.1, for both ZnO and GaN.

Table 3.1: Parameters for optimized plasma.

	Chamber pressure (mTorr)	Electron energy (KV)	Pulse rate (Hz)	Vertical Gap (mm)
ZnO	5.5 (Ar)	11	3	2
GaN	14 (N_2)	15	3	2
AlN	20 (N_2)	15	1	2

Optimization of the AlN plasma was more difficult due to the following reasons:

- Generation of atomic nitrogen is difficult (especially, if the material purity is low).
- It takes longer time to reach a steady state plasma condition (the first few nm of deposition had high Al content).
- Requires more energy density for plasma generation.

Nevertheless, we succeeded in depositing high aspect ratio, crystalline, micron scale AlN nanowires. A higher nitrogen process gas pressure of 20 mTorr was used, as the target material purity was lower (99.8%) as compared to the purity of the GaN target (99.99%).

The GaN plasma, in its optimized condition, generates the species listed in Table 3.2. The shaded components are the ones held responsible for the chemical reaction to form GaN thin films during PED operation [39]. Figure 3.7 shows the total emission spectrum from a GaN plasma in an N_2 environment under the optimized condition in Table 3.1. The broad spectrum in the infrared region is due to the emission coming from the substrate heaters below the transparent sapphire substrate during deposition. Figures 3.8 and 3.9 show the GaI peaks and the NI atomic nitrogen peaks. Using optical

emission spectroscopy, the time dependent variation of the species in Table 3.2 is observed in detail. Traces were collected for the four spectral lines, integrated around the values mentioned in the Table 3.2.

Table 3.2: Plasma generated reactive components of GaN target.

Species	**λ (nm)**	**Lower level conf., term, J**	**Upper level conf., term, J**
GaI	403.298	$3d^{10}4s^2 4p,\ ^2P^0,\ 3/2$	$4s^2 5s,\ ^2S,\ ½$
GaI	417.204	$3d^{10}4s^2 4p,\ ^2P^0,\ 3/2$	$4s^2 5s,\ ^2S,\ ½$
GaII	426.201	$4s4d,\ ^3D,\ 3$	$4s4f,\ ^3F^0,\ 3$
GaIII	486.303	$3d^{10}5s,\ ^2S,\ ½$	$3d^{10}5p,\ ^2P^0,\ 3/2$
NII	500.148	$2s^2 2p3p,\ ^3D,\ 2$	$2s^2 2p3d,\ ^3F^0,\ 3$
GaII	521.646	$4s5d,\ ^3D,\ 1$	$4s7f,\ ^3F^0,\ 2$
GaII	536.358	$4s5p,\ ^3p^0,\ 1$	$4s5d,\ ^3D,\ 1$
GaII	541.631	$4s5p,\ ^3p^0,\ 2$	$4s5d,\ ^3D,\ 3$
GaII	633.406	$4s5s,\ ^3S,\ 1$	$4s5p,\ ^3P^0,\ 2$
NI	642.064	$2s^2 2p^2(^3\mathrm{P})3p,\ ^4D^0,\ 5/2$	$2s^2 2p^2(^3\mathrm{P})4d,\ ^4D,\ 5/2$
NI	642.832		

The time traces of the four atomic components were also studied with the impact of changes from the process gas pressure in the chamber, i.e., the chamber pressure. For the Ga reactive components (Figure 3.10) with the increase of chamber pressure the spectral intensity is reduced. However, with the pause of N_2 gas supply, the intensity reduces to zero since the gun function is halted. On the other hand, staying in a safe limit of operation, reducing the chamber pressure (through a mass flow controller) increases the intensity. Since a reduced amount of gas is fed in the chamber, a reduced amount of gas particles interact with the high energy electron beam leaving a significant amount of electrons to interact with the target material.

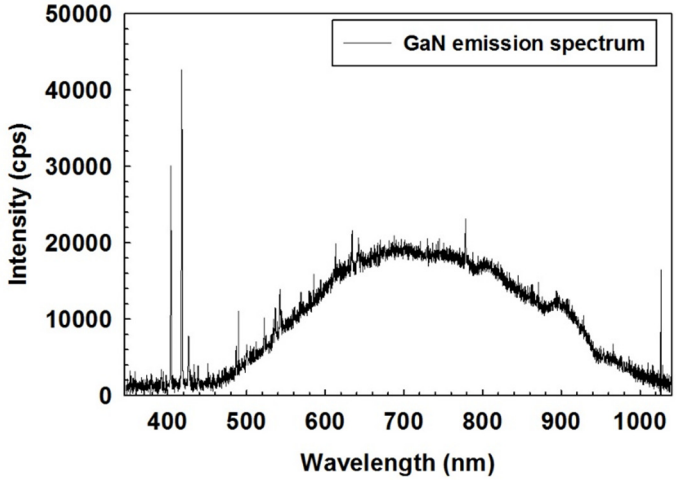

Figure 3.7: GaN emission spectrum in N_2 environment.

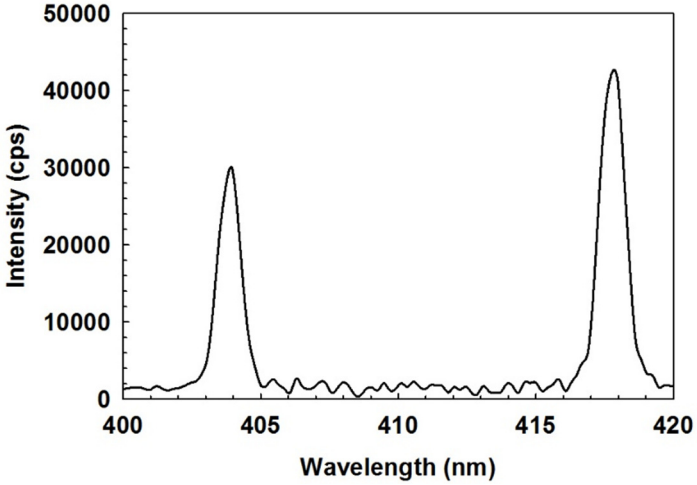

Figure 3.8: GaI peaks at 403.298 and 417.204 nm spectral lines.

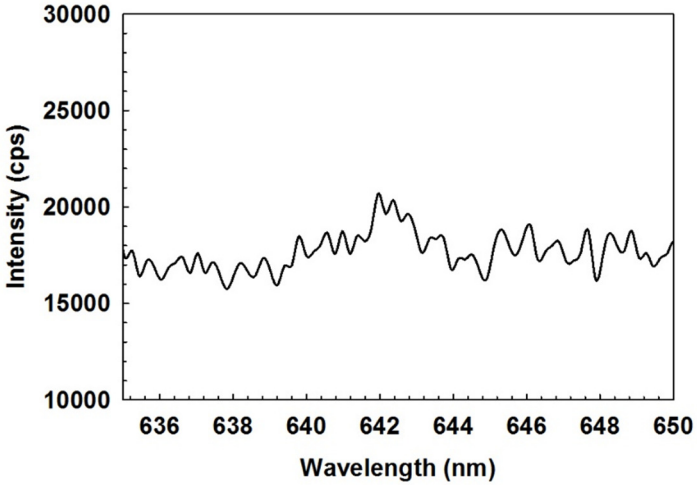

Figure 3.9: NI peaks (atomic) at the 642.064 and 642.832 nm spectral lines.

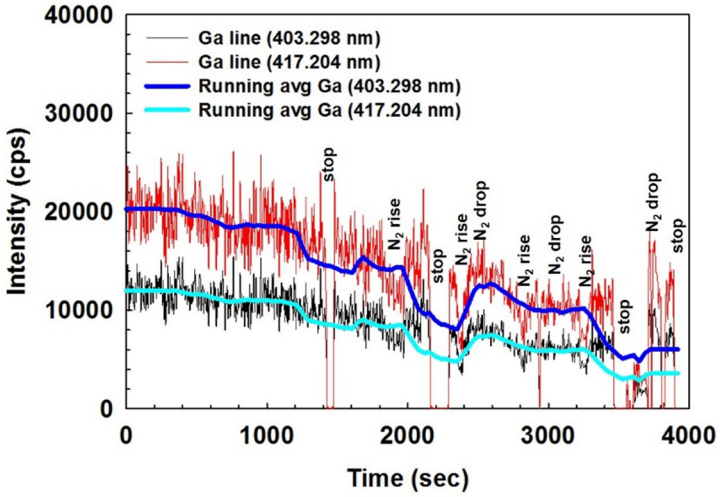

Figure 3.10: Atomic GaI peak traces (time dependent) with chamber pressure dependency.

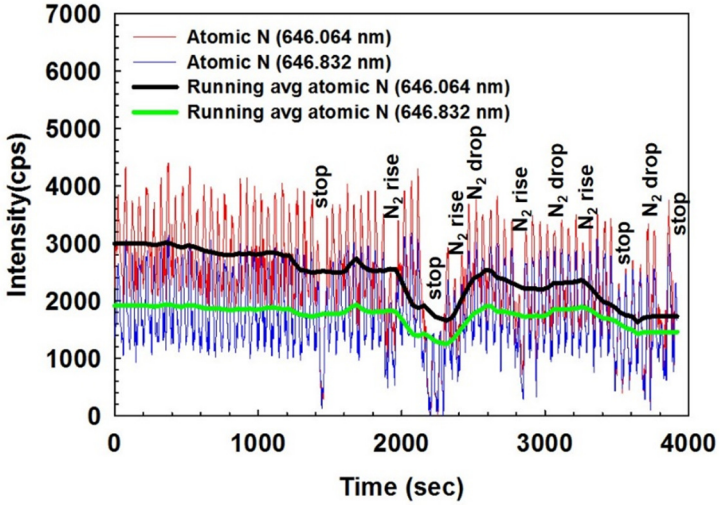

Figure 3.11: Atomic NI peak traces (time dependent) with chamber pressure dependency.

The study of the atomic N traces (Figure 3.11) shows the similar behavior as shown in the Figure 3.10. As the traces behave in reciprocal relation with the process gas pressure changes, it can be concluded that atomic nitrogen results from the target material (here binary GaN, 99.99% pure), rather than the N_2 process gas.

3.6 Thin film characterization techniques

Different thin film characterization techniques were used to study the structural, stoichiometric, optical, and electrical properties of the grown samples. A few of these properties were also analyzed in respect to substrate temperature changes. Table 3.3 summarizes the characterization techniques used in this research.

Table 3.3: List of characterization techniques used for thin film analysis

Technique	**Acquired information**	**Equipment**
HR-FESEM	Crystallites and thin film imaging (planar and cross-section)	Zeiss Neon 40 EsB
EBSD	Crystal orientation in nanoscale regions	Zeiss Neon 40 EsB
EDX	Thin film surface stoichiometry	Zeiss Neon 40 EsB
X-ray diffraction	Crystal growth orientation	Rigaku Ultima IV
Photoluminescence	Optical properties	Princeton Instruments
Rutherford Back Scattering Spectroscopy	Morphological properties	Van de Graaf IBA system
Hall measurement	Electrical properties	Ecopia HMS 5000

3.6.1 Field emission scanning electron microscopy

A high resolution field emission electron microscope (Zeiss Neon 40 EsB) with combined imaging and analytical capabilities was used. This machine is capable of high resolution imaging (1.1 nm resolution) along with focused ion beam (FIB) imaging, energy dispersive x-ray spectroscopy (EDX) for surface chemical analysis, and electron back scattered diffraction (EBSD) to study thin film crystallinity. Figure 3.12 shows the HR-FESEM at the Samuel Roberts Noble Microscopy Laboratory at university of Oklahoma, Norman, OK. Some characteristics of the system are listed below [40]:

- Dual beam SEM/FIB
- Accelerating voltage: 0.1-30 kV

- Electron source: Schottky emitter (Gemini lens SEM column)

Figure 3.12: HR-FESEM system at University of Oklahoma.

- 2-30 kV Ga liquid metal ion source (Canion FIB column)
- Magnification: X 20 to X 900,000
- 1.1 nm resolution
- The Oxford EBSD (energy and angle selective BSE) detector can provide compositional and orientation information
- Multi-channel gas injection system for deposition of metal and insulating layers as well as enhanced and selective etching
- INCA Energy 250 Energy Dispersive X-ray Microanalysis system with Analytical Drift Detector

3.6.2 Powder diffraction XRD

X-ray diffraction is a nondestructive characterization technique revealing the crystal orientation of the deposited thin film with respect to the substrate. In addition, using the obtained data from powder diffraction, film grain size and lattice constant can be calculated. Powder x-ray diffraction (XRD) analyses were performed in the School

of Geology and Geophysics at the University of Oklahoma using a Rigaku Ultima IV diffractometer. Cu-K-alpha radiation (40 kV, 44 mA) was used with a scintillation detector. The samples were adhered to the center of the sample holder using a small amount of vacuum grease. They were analyzed using Bragg-Brentano optical set-up, with a 5 mm divergent height limiting slit, a variable divergent slit, a variable scatter slit, a 0.3 mm receiving slit, and a 5 mm irradiation width. The samples were azimuthally rotated during irradiation at 30 RPM, and data were collected over a 2Θ range of 2^{o}-70° at a 0.02 step size with a 2 second count time.

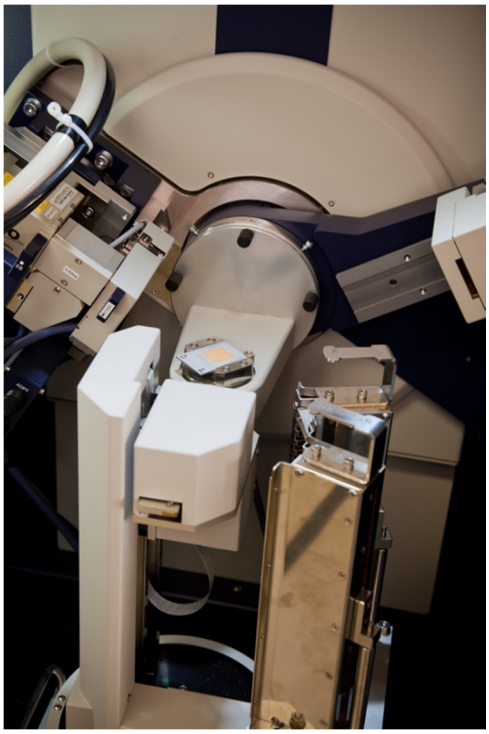

Figure 3.13: Rigaku Ultima IV powder diffractometer (Courtesy of Dr. A. S. Madden, University of Oklahoma).

Figure 3.13 shows the Rigaku powder diffractometer at University of Oklahoma. Using the Scherrer equation [41], the average grain size of the thin films can be calculated:

$$D = \frac{0.9\lambda}{A\cos\theta} \tag{3.1}$$

Here, D is the grain size in nm, λ is the x-ray wavelength (in nm), A is the FWHM of the diffraction peak (in radian, from Θ-2Θ scan), Θ is the position of the diffraction peak in the scan (in radian).

3.6.3 Photoluminescence (PL)

Photoluminescence is a non-destructive analytical method that can provide useful electronic band structure information for grown materials. A sample is irradiated using a high energy laser which excites electrons to a high energy state. This high energy electron returns to a lower energy state and emits a photon. Using a CCD detector the photon emission spectrum is collected and qualitative and quantitative information can be obtained for the material bandgap and the presence of defects.

Figure 3.14 shows the PL system setup used in this research. The detector is a Princeton Instruments PIXIS-eXcelon silicon CCD (350-950 nm) detector. The spectrometer is Princeton Instruments Acton SP2560i spectrometer. The samples were illuminated with a Kimmon Electric HeCd dual wavelength (325 and 442 nm) laser (model: IK552). We used the 325 nm laser line for our samples. The system is equipped with a cryostat (Janis Model SHI-4-5 optical closed-cycle system operating between 4.2 and 300K).

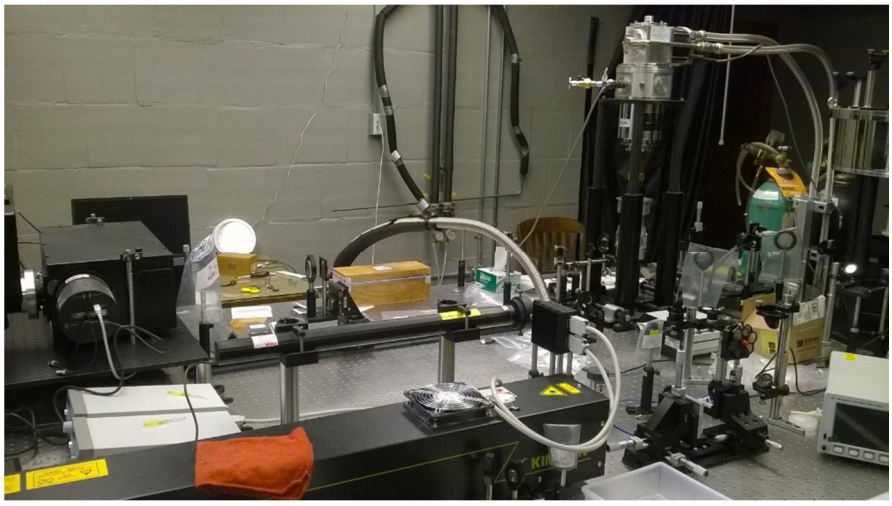

Figure 3.14: Photoluminescence system setup (Courtesy of Dr. Ian Sellers, University of Oklahoma).

3.6.4 Rutherford back-scattering spectroscopy (RBS)

Rutherford back-scattering spectroscopy is a standard analytical thin film characterization process based on the kinematics for binary collisions. In this process a beam of known particle mass and energy is incident on an unknown sample at a specific incident angle. The incident and the impacted particles experience difference in momentum and direction of motion after impact. The changed energies and scattering angles of the incident beam particles are recorded, and using laws of conservation of momentum and energy, the unknown thin film properties are identified. Figure 3.15 shows the RBS system setup at Amethyst Research in Ardmore, OK. It uses a Van de Graaff accelerator at 1.5 MeV of ^{4}He+ beam. Scattering angle of the system was dedicated at 160^{o}.

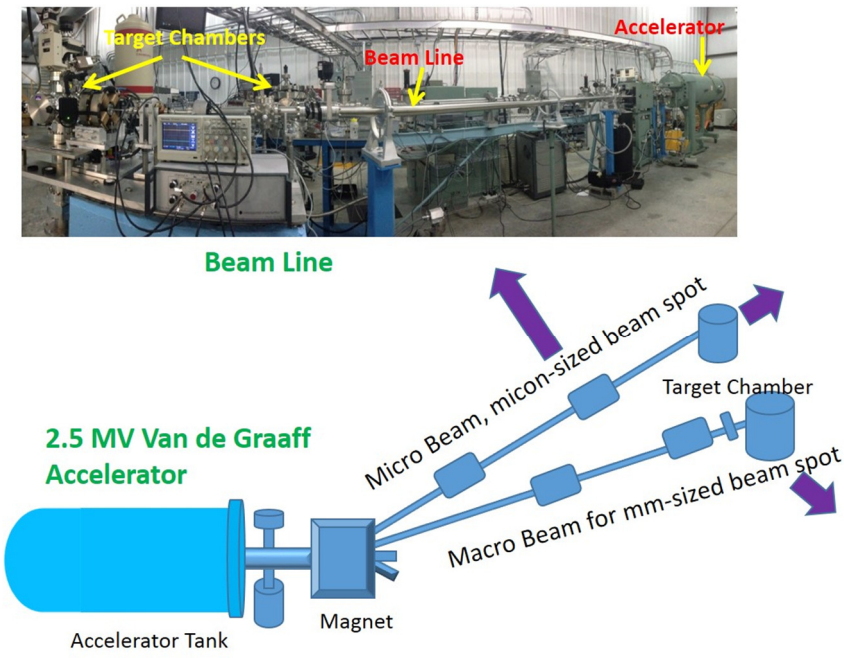

Figure 3.15: Ion Beam Analysis system hosting RBS system (top). Schematic of the system (bottom) (Courtesy: Dr. Khalid Hossain, Amethyst Research Inc, OK).

3.6.5 Hall measurement

A Hall Effect measurement system is a very important tool to determine the electrical properties of materials. Polarity of the charge carriers (e^- or hole), carrier mobility, conductivity, bulk and sheet concentrations are the important properties for this research work. Figure 3.16 shows the Ecopia HMS 5000 Hall Effect measurement system. It has the ability to collect parameters with temperature dependency ranging from 80-300K. The following are the equipment operation ranges to study samples:

- Sample size: 5 mm x 5 mm up to 15 mm x 15 mm
- Resistivity: 10^{-4} to 10^{7} (Ω-cm)
- Magnetic flux density: 0.55 Tesla (nominal)
- Mobility: 1~10^{7} (cm^2/V-sec)

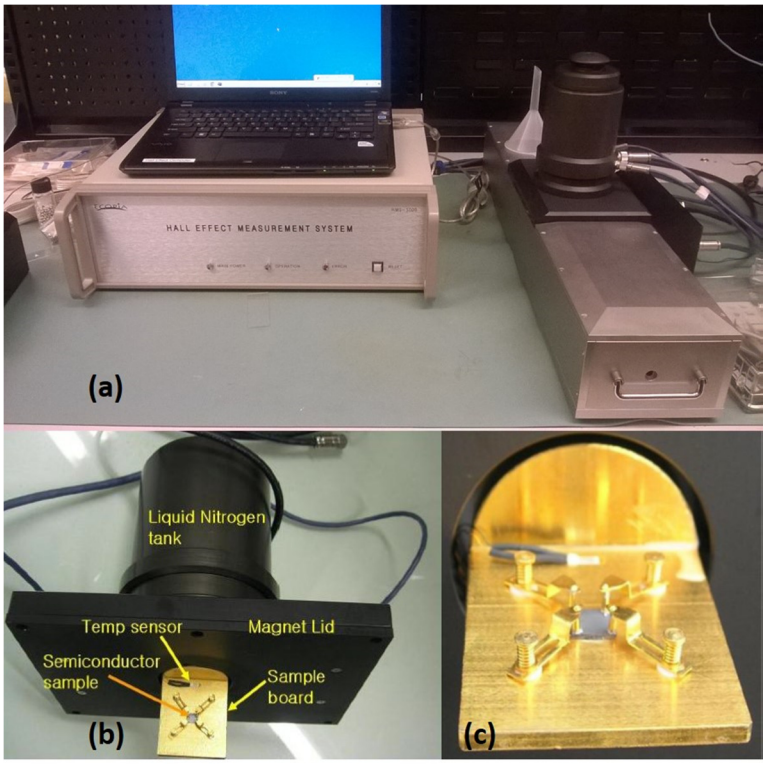

Figure 3.16: (a) Ecopia HMS-5000 Hall Effect Measurement system, (b) sample mounting fixture with upper cooling reservoir, and (c) sample mounting fixture (Photo: courtesy of Dr. Patrick. J. McCann, University of Oklahoma).

- Bulk carrier concentration: 10^{7} ~ 10^{21} (cm^{-3})
- Current source range: 1 nA ~ 20 mA compliance: 12V
- Minimum Hall voltage: 1 µV
- Temperature range: 80K to 300K

3.7 Summary

An overview on the pulsed electron beam deposition (PED) system is presented followed by the critical plasma generation parameters and their optimization routine. Trace analyses have been presented on the successful attempts to the formation of III-nitride plasma. Later in the chapter brief description of the characterization techniques used in this research has been presented. The next chapter will describe the results obtained with growth of group III-nitrides and ZnO on different substrate materials.

Chapter 4 : Growth and characterization of wide bandgap materials

4.1 Motivation

The PED system description has been presented followed by plasma generation and optimization along with brief description on the characterization techniques in Chapter 3. The first two chapters focused on the market and current technology involved in low temperature growth of wide bandgap materials. This chapter will present results from the growth of ZnO, GaN, and AlN nanowires grown on sapphire and silicon substrates.

4.2 Growth and characterization of ZnO films

ZnO was grown on sapphire at substrate temperatures ranging from 300^{o} to 700^{o}C. Similar growth of ZnO was carried out on Si(100) substrates at 300^{o} and 500^{o}C. The growth process parameters remained the same (shown in Table 4.1), except the substrate temperatures.

Table 4.1: Parameters for ZnO/sapphire and ZnO/Si(100) growth

	ZnO/sapphire	**ZnO/Si(100)**
Substrate temperature	700^{o}, 500^{o}, 300^{o} C	500^{o} and 300^{o} C
Chamber pressure	7 mTorr (Ar)	7 mTorr (Ar)
Electron gun voltage	11 KV	11 KV
Pulse rate	3 Hz	3, 5 Hz
Target-e^{-} gun tip distance	2 mm	2 mm
Target-substrate distance	5 cm	5 cm
Substrate rotation	20 rpm	20 rpm

4.2.1 Experimental Detail

The substrates were prepared according to the process mentioned in Section 3.3. Every growth run is preceded by obtaining a base pressure of ~10^{-7} Torr. After the substrates were heated to desired temperature, sufficient time was provided for the

chamber pressure to recover from the outgassing wafers. Typical times were 30 minutes to 60 minutes. We used four similar substrates in each growth run. Following the procedure in Section 3.5, ZnO plasma was produced in an Ar environment, and deposition began. The emission spectroscopy lines were monitored during growth to avoid any dominance of metal reactant species. After intended amount of pulses were fired, the desired deposition being done, the samples were cooled in the Ar environment and later in vacuum.

Grown samples were taken for characterization using powder diffraction (XRD) first. This tells about the growth orientation of the ZnO thin film. SEM images were then taken for planar view and cross-section followed by EDX and EBSD characterization in the same instrument. Finally, Hall effect measurements and photoluminescence characterization were performed. The characterization data will be presented in the next sections.

4.2.2 Structural and morphological characterization

Figure 4.1 shows the SEM images (planar and cross section) of the ZnO samples on sapphire grown at temperatures 700^{o}, 500^{o}, and 300^{o}C. As shown, for same number of pulses, the film thickness, grain sizes, and growth rate are all increased with substrate temperature increase. The grain size ranges from 100-200 nm for the sample grown at 700^{o}C. For the sample grown at 500^{o}C it ranged from 60-100 nm, and when the sample is grown at 300^{o}C, the grain size was reduced to the range of 20-50 nm. The growth rate is estimated as Å/pulse in pulsed electron beam deposition system. Figure 4.2 shows the increment in growth rate according to the growth temperature.

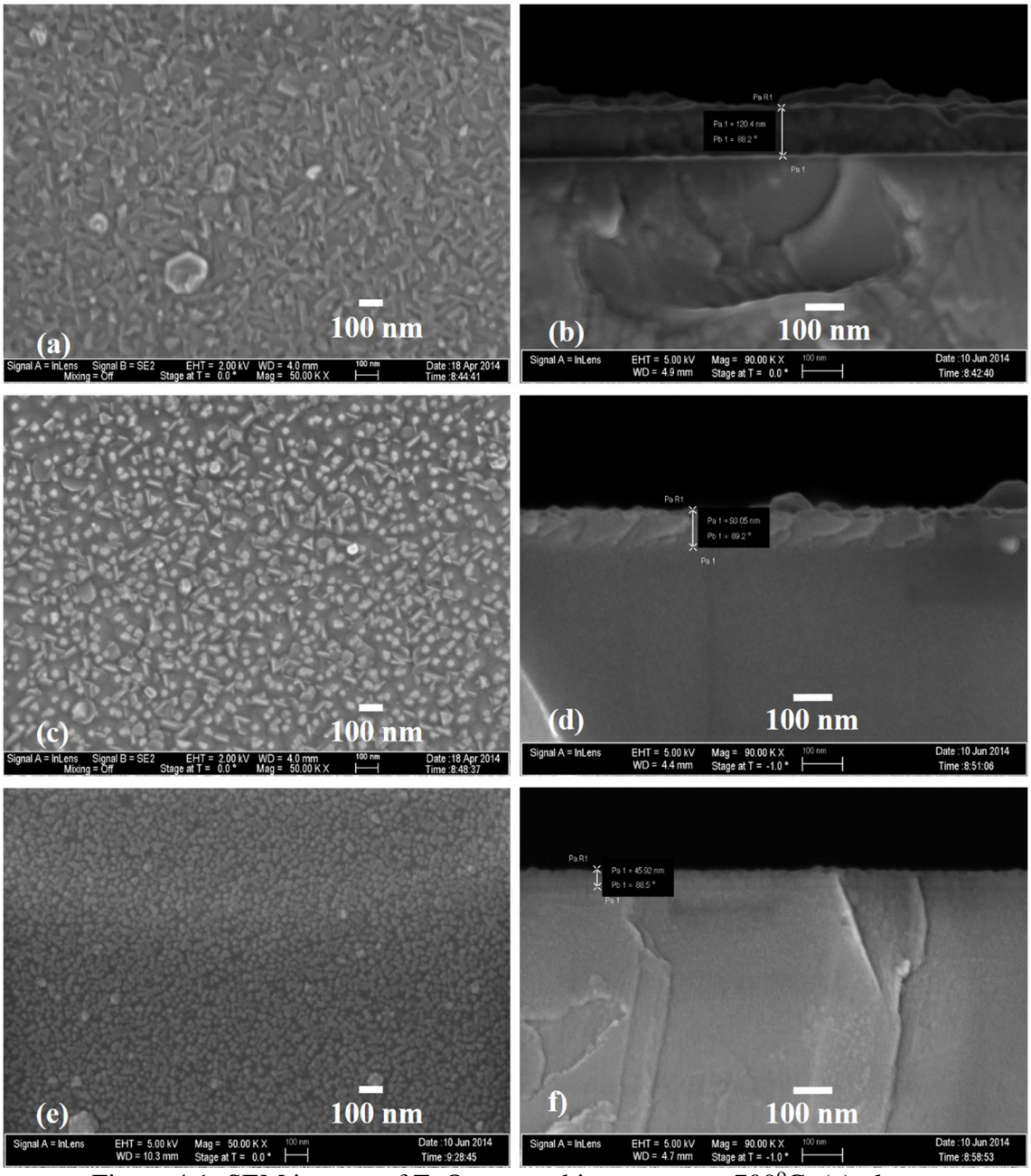

Figure 4.1: SEM images of ZnO on sapphire- grown at 700°C: (a) planar, (b) cross-section, at 500°C: (c) planar, (d) cross-section, and at 300°C: (e) planar, (f) cross-section.

The increment appears to be linear ranging from 0.167 Å/pulse (at 300°C) to 0.463 Å/pulse (at 700°C). Similar phenomenon was observed by Son *et al* [42] as they studied the growth of ZnO using PLD process. Also, Omichi *et al* [43] experienced similar

growth rate increment using HVPE growth process in the similar temperature range of growth. The deposition of ZnO takes place in a surface-kinetics-limited regime as described by Bang *et al* [44] as the Arrhenius plots in [42] and [43] showed negative slope. Similar Arrhenius plot with a negative slope was also observed for the growth of ZnO/sapphire using PED (Figure 4.2). Some other processes, such as ALD growth of ZnO [45] show rise and fall of the growth rates as a bell-shape curve. But, as appears in pulsed energy deposition processes, the main factor of growth limitation is the adsorption and migration of the growing species on the growing surface, rather than desorption of growing-species depending on the sticking coefficient. With increment in growth temperature the adsorption of growing species is increased by higher thermal energy [42] yielding higher growth rate.

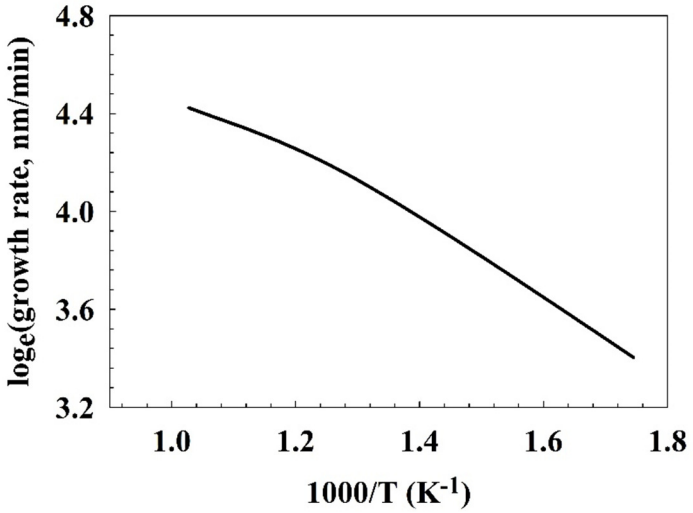

Figure 4.2: ZnO on sapphire: growth rate as a function of temperature.

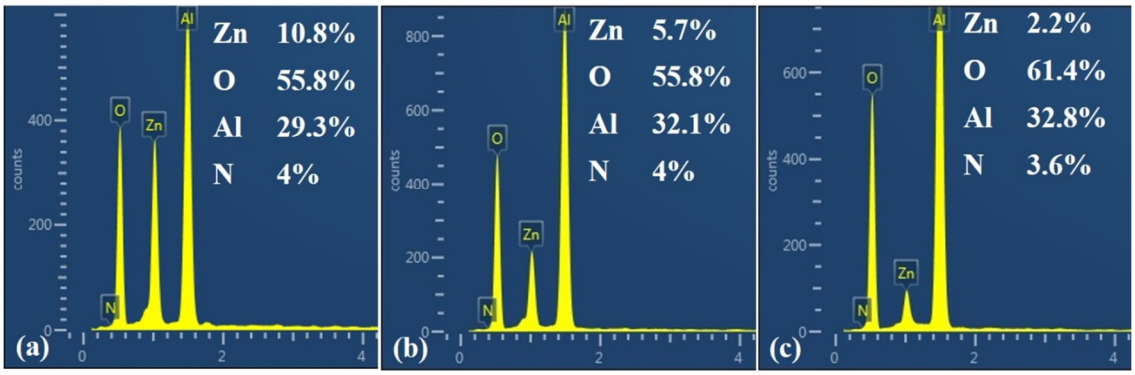

Figure 4.3: EDX analysis of ZnO/sapphire grown at (a) 700°C, (b) 500°C, and (c) 300°C.

As it appears in the EDX analysis (Figure 4.3), with same number of pulses deposited on sapphire at different temperature, the peak of Zn at 1 keV decreases with temperature, following the similar trend demonstrated in Figure 4.2. Figure 4.4 shows the powder diffraction plots of the three samples. With the increase of sample growth temperature (as well as thickness), there appeared an additional non-polar (10-11) peak along with the polar (0002) plane. However, the intensity of the non-polar planes are significantly lower than the polar planes, showing the dominance of the polar direction growth. This is caused by the increment in surface migration rate with the increase in growth temperature. Experiencing higher thermal energy at an increased growth temperature, the growing species migrate with more flexibility to the nearest grains with higher crystallographic orientations with higher surface energy as well as the polar (0002) direction. Thus, the films grown at higher growth temperature consist of grains of other crystallographic orientations as well as the polar (0002) plane [42].

To validate the growth direction of the epilayers, the ZnO/sapphire samples were characterized using the EBSD technique (Figure 4.5). Analyzing the Kikuchi lines [46] [47], we found that the growth direction of the deposited ZnO films on sapphire at different temperatures ranging from 300°-700°C is dominated mostly by the (0002)

direction of growth, i.e., *c*-plane direction or the polar direction of growth. The following table (Table 4.2) presents the relative intensity of the backscattered electrons from different planes in the three samples. A following table (Table 4.3) contains the data for the spacing between the planes identified in the three samples. The *d*-spacing for the planes estimated by the EBSD tool match with the data published [48] [49] for the *d*-spacing in ZnO crystals grown by chemical bath deposition.

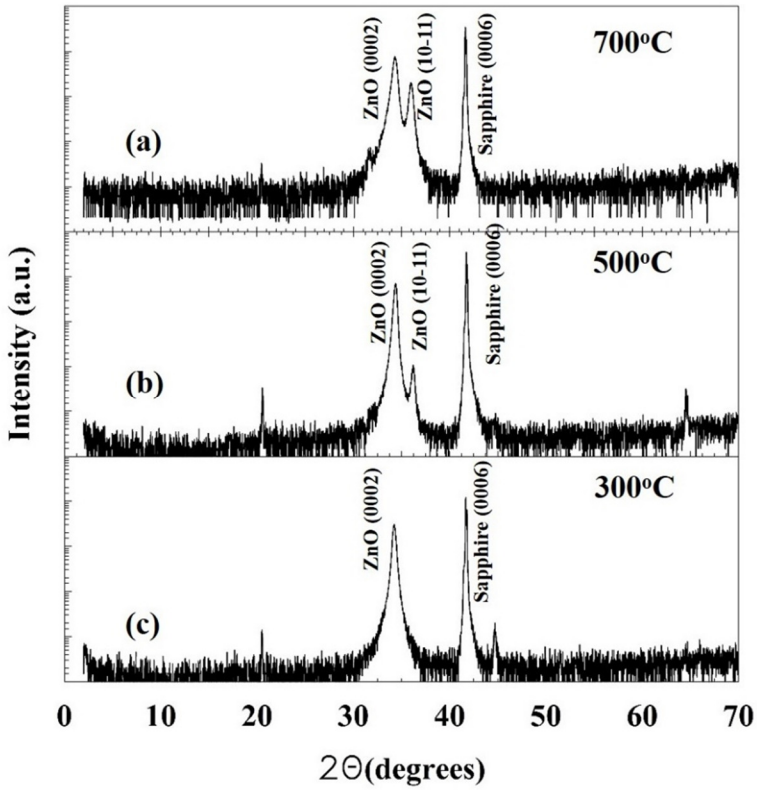

Figure 4.4: Θ-2Θ scans from x-ray powder diffraction for ZnO/sapphire samples grown at (a) 700°C, (b) 500°C, and (c) 300°C.

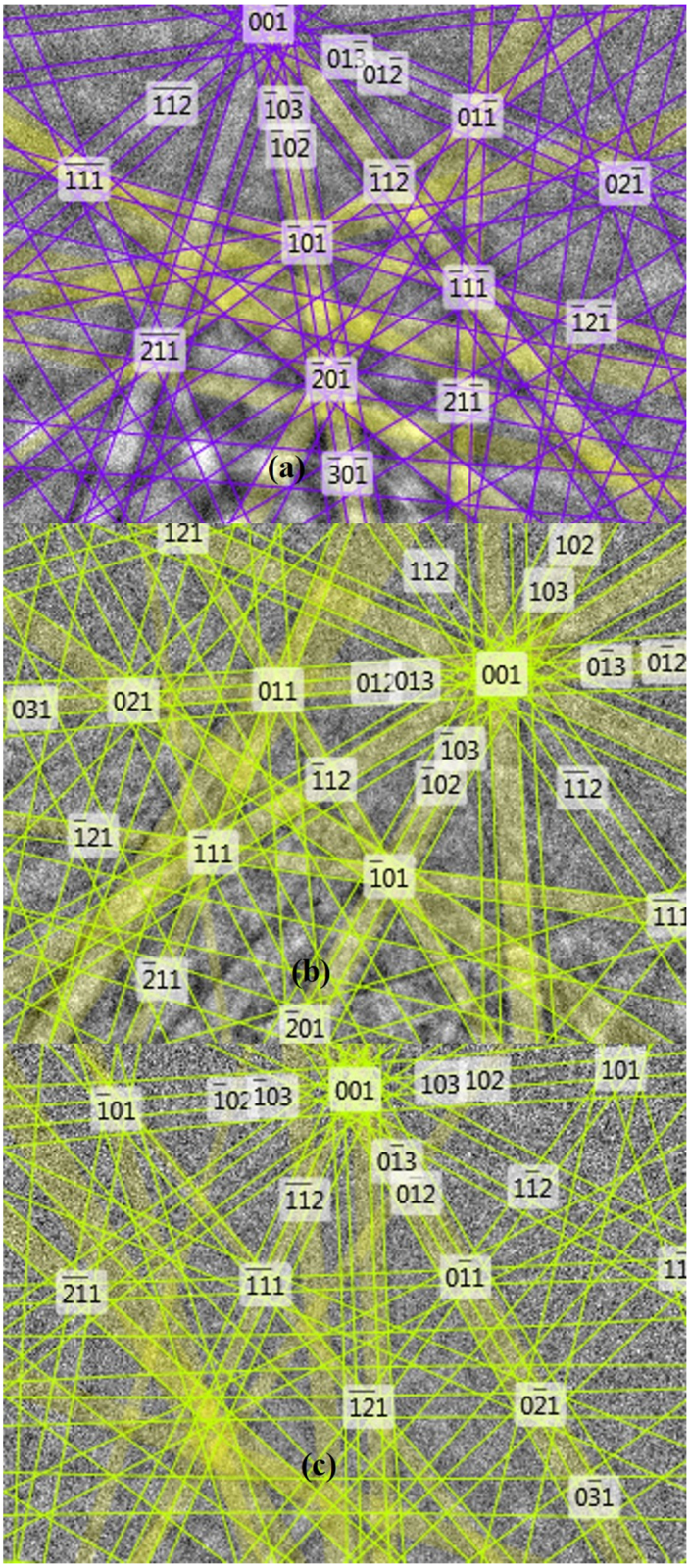

Figure 4.5: Kikuchi patterns generated from electron back-scattered diffraction (EBSD) from ZnO/sapphire samples grown in (a) 700°C, (b) 500°C, and (c) 300°C.

Table 4.2: Relative diffraction intensity from crystal planes of ZnO/sapphire samples.

hkil **plane**	**Diffraction intensity (%)**		
	700°C	**500°C**	**300°C**
0002	100.0	100.0	100.0
11-20	72.2	76.0	76.0
2-1-10	72.2	76.0	76.0
1-210	72.2	76.0	76.0
1-100	41.9	44.2	44.2
10-10	41.9	44.1	44.1
01-10	41.9	44.1	44.1
10-13	35.7	39.7	39.7
01-1-3	35.7	39.7	39.7

Table 4.3: Distance between planes (observed in EBSD scan) of ZnO/sapphire samples.

hkil **plane**	**Distance between adjacent planes (Å)**		
	700°C	**500°C**	**300°C**
0002	2.6049	2.6076	2.6076
11-20	1.6270	1.6268	1.6268
2-1-10	1.6270	1.6268	1.6268
1-210	1.6270	1.6268	1.6268
1-100	2.8180	2.8176	2.8176
10-10	2.8180	2.8176	2.8176
01-10	2.8180	2.8176	2.8176
10-13	1.4784	1.4795	1.4795
01-1-3	1.4784	1.4795	1.4795

After the Kikuchi patterns were identified, the low temperature growths of the ZnO/sapphire samples (grown at 500° and 300°C) were studied. Mapping of the sample surfaces provides information on the epitaxial nature and dominance of a single growth direction of the epilayers. Figure 4.6 shows the EBSD area mapping of the ZnO/sapphire samples grown at lower temperatures. As shown, the mapped data points are accumulated near the *c*-plane growth direction (0001).

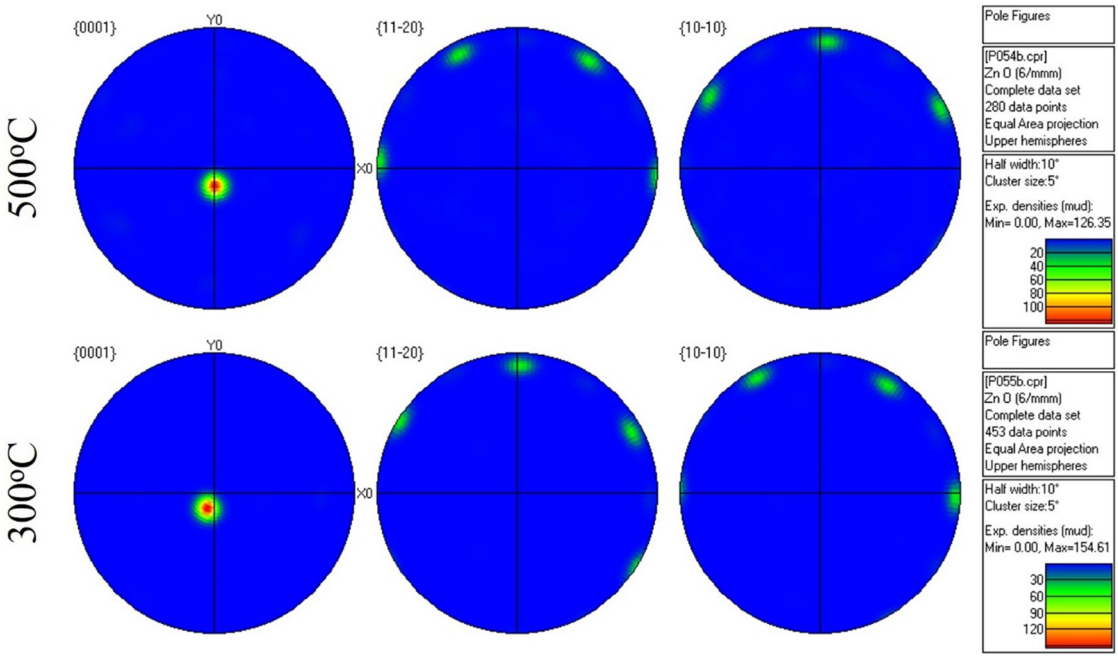

Figure 4.6: EBSD mapping obtained for ZnO/sapphire samples grown at (top) 500°C and (bottom) 300°C.

At this point, two other ZnO samples were grown on Si(100). The growth procedure was similar to the ZnO/sapphire samples, and substrate cleaning was same as cleaning the Si(111) substrates (Section 3.3). The growth parameters were kept the same as the ZnO/sapphire growth, except for the ZnO/Si(100) sample grown at 300°C, as the pulse rate was increased to 5Hz, compared to 3Hz for the other cases, with total number of pulses being the same, which was 2700. Figure 4.7 shows SEM images of the ZnO/Si(100) samples grown at 500° and 300°C. The sample grown at 500°C shows a rough surface morphology with grain sizes in the range of 50-300 nm, while the other sample (grown in 300°C) shows a more coalesced thin film with a grain size in the range of ~30nm.

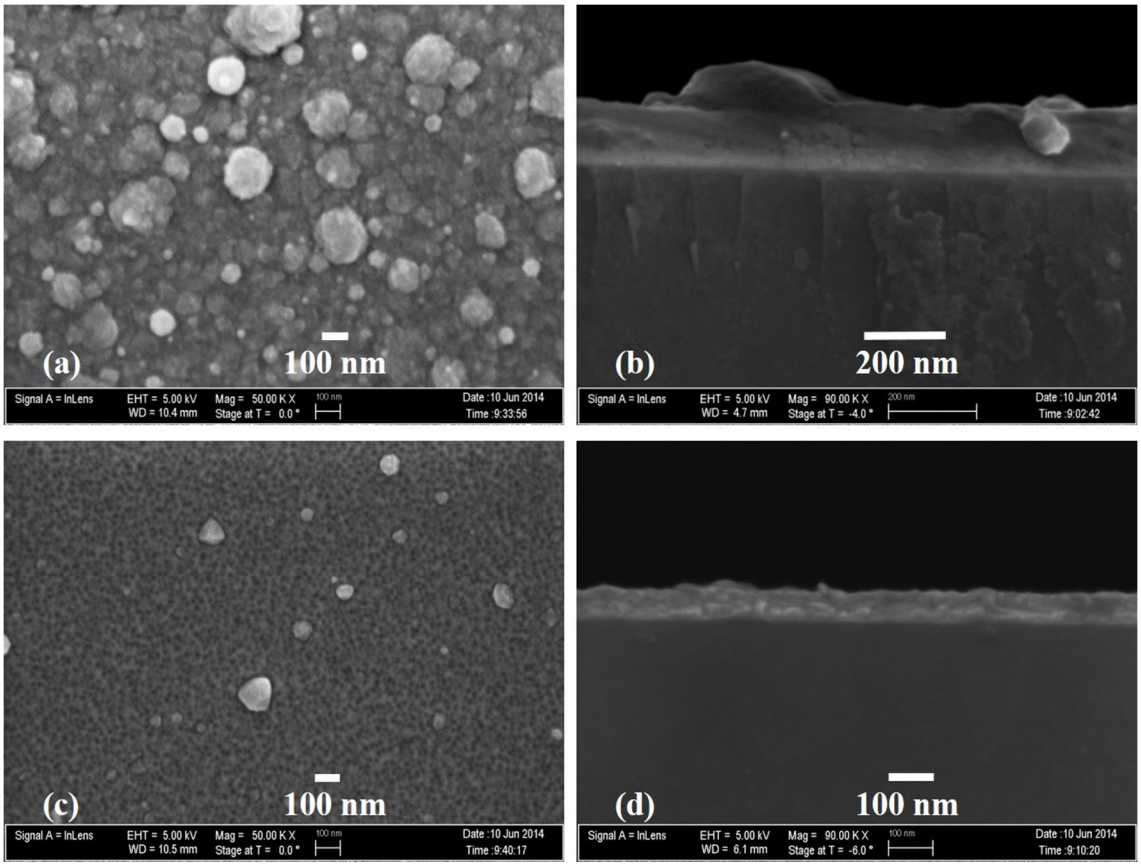

Figure 4.7: SEM images of ZnO on Si(100) grown at 500°C: (a) planar, (b) cross-section, and at 300°C: (c) planar, (d) cross-section.

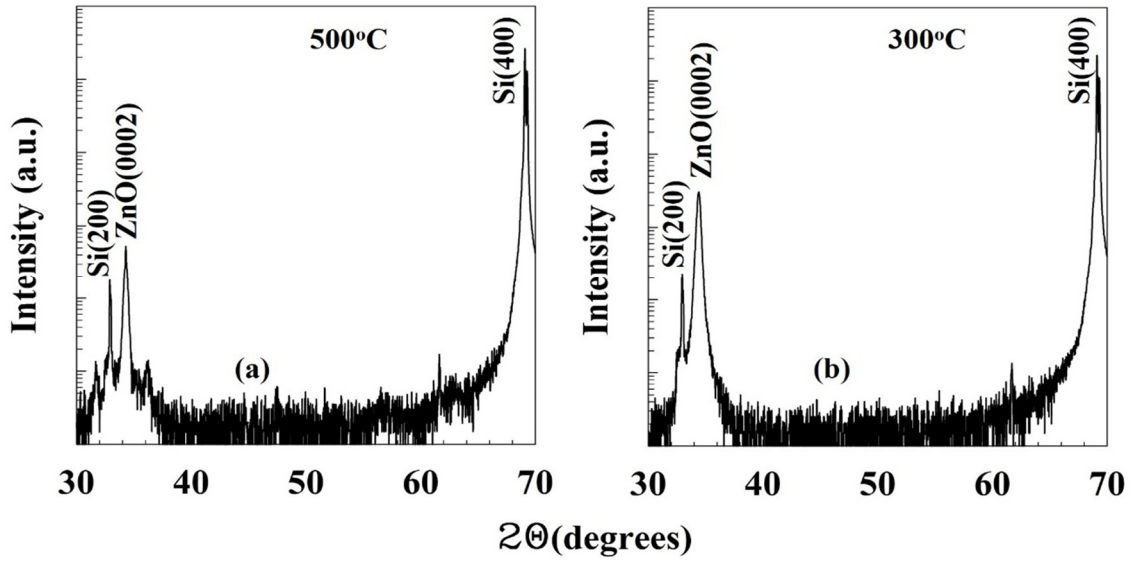

Figure 4.8: θ-2θ scans from x-ray powder diffraction for ZnO/Si(100) samples grown at (a) 500°C and (b) 300°C.

Powder x-ray diffraction analysis performed on these samples (Figure 4.8) showed that the grown layer on top of the Si(100) substrate has a predominately (0002) orientation. No other diffraction peaks were observed in the XRD scan. As we observe, the higher temperature growth of ZnO/Si(100) (at 500^{o}C) shows presence of some other peaks, but very negligible in comparative intensity, while the low temperature ZnO/Si(100) sample, Figure 4.8(b), shows the presence of only ZnO(0002) polar plane in Si(100). The FWHM values of the ZnO(0002) peaks were 0.2^{o} and 0.3^{o} for the samples grown in 500^{o} and 300^{o}C, respectively. Analyzing both Figures 4.4(c) and 4.8(b) it appears that PED grown ZnO at a low temperature of 300^{o}C with an optimized plasma is epitaxial with *c*-plane orientation. This ZnO layer can be used as a template for GaN growth at low temperature, as will be demonstrated later in section 4.3.

The ZnO/Si(100) samples were also characterized using the EBSD technique to verify the dominant growth direction along with the lattice plane spacing, as have been shown earlier in this section for the ZnO/sapphire samples. The EBSD scan shows that the sample contains *c*-plane (0002) ZnO as the dominant orientation for the deposited material. The determined lattice plane spacing also match with the data published in [48]

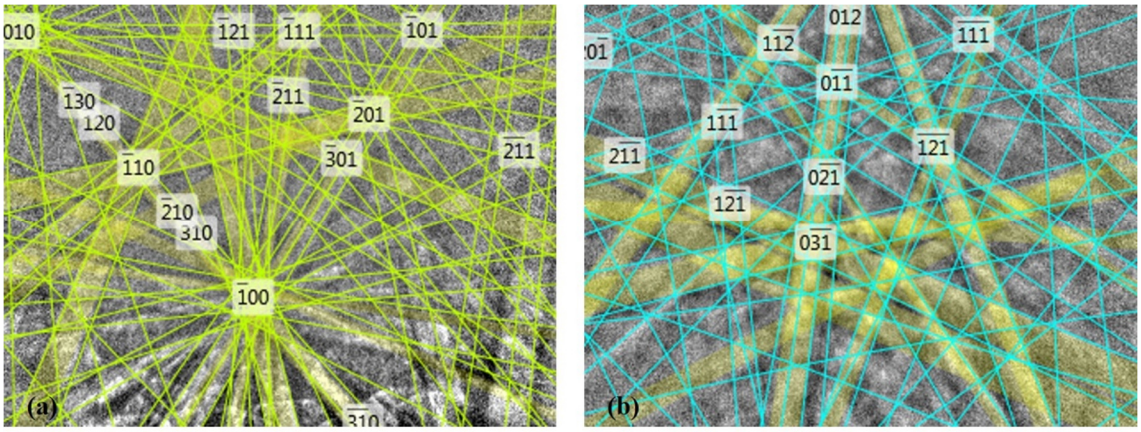

Figure 4.9: Kikuchi patterns generated from electron back-scattered diffraction (EBSD) from ZnO/Si(100) samples grown in (a) 500°C and (b) 300°C.

Table 4.4: Relative diffraction intensity and distance between planes (observed in EBSD) of ZnO/Si(100) samples.

hkil **plane**	**Diffraction intensity**		**Distance between planes (Å)**	
	500°C	**300°C**	**500°C**	**300°C**
0002	100.0	100.0	2.6076	2.6025
11-20	76.0	76.6	1.6268	1.6245
2-1-10	76.0	76.6	1.6268	1.6245
1-210	76.0	76.6	1.6268	1.6245
1-100	44.2	44.5	2.8176	2.8136
10-10	44.1	44.5	2.8176	2.8136
01-10	44.1	44.5	2.8176	2.8136
10-13	39.7	40.2	1.4795	1.4768
01-1-3	39.7	40.2	1.4795	1.4768

[49], as shown in Table 4.4.

4.2.3 Optical characterization

A 325 nm He-Cd laser equipped photoluminescence system was used to collect the optical excitation response of the ZnO samples grown on sapphire and Si(100) substrates. Figure 4.10 shows the photoluminescence emission from the ZnO/sapphire samples at both 4K and room temperature (295K). The near-band-edge (NBE) emission at 370 nm is stronger in intensity for the sample grown at 700°C as compared to the

other two samples. This is strongly influenced by the thickness of the samples. All the spectra in Figure 4.10 are comprised of a violet emission band, i.e., the NBE emission at around ~370 nm, and a broad band in the range of 500-700 nm, i.e., the green-yellow-orange band, likely originating from the defects in the deposited material. ZnO demonstrates luminescence in the defect band due to different intrinsic and extrinsic defects [50] [51]. Djurišić *et al* [50] studied the sources of green and yellow emission from different point defect and donor-acceptor possibilities, and explained such broad emission as due to such defects. They concluded that the broad defect band is not due to a single point defect, Zn or O, rather a collection of different phenomena acting together creating different oxygen and zinc vacancies. They have grown ZnO structures in humid Ar environment (similar to that reported in this dissertation), and their PL response matches with that observed in Figure 4.10 with a large and broad defect band. Also, they [50] experienced larger intensity in the defect band once they have grown thinner ZnO layers , which also satisfies the observation in Figure 4.10(c). As it appears, the emission peaks are distinguishable in the low temperature PL spectra, while the room temperature data reveals the effect of phonon scattering. In addition, the NBE emission peak experiences a red shift (11.4 nm or 0.1 eV) at higher temperature, according to the Varshni formula.

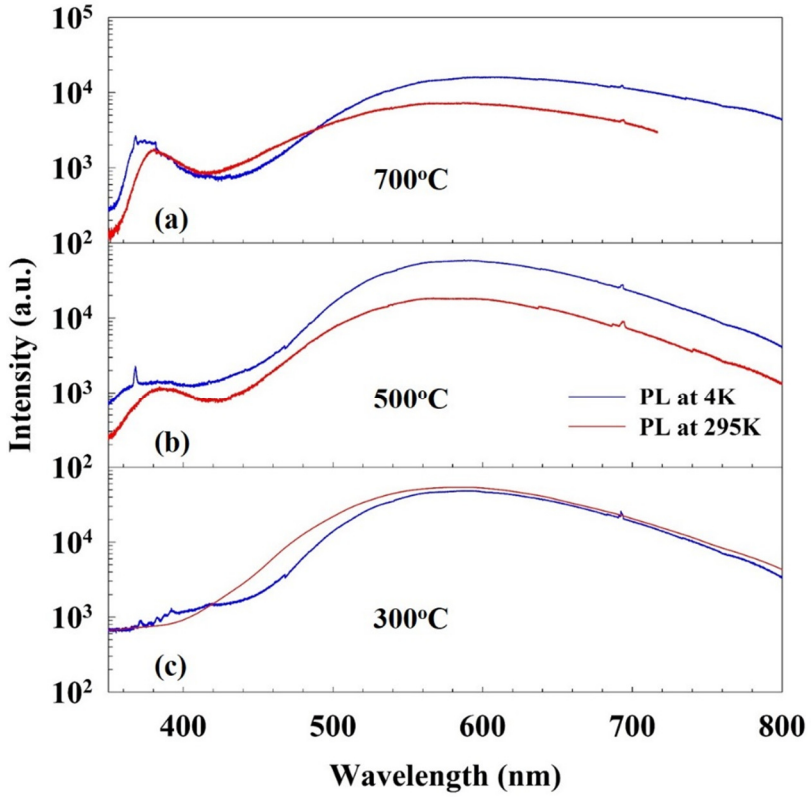

Figure 4.10: Photoluminescence spectra of ZnO/sapphire samples grown at (a) 700°C, (b) 500°C, and (c) 300°C. Blue and red lines are the PL responses in 4K and room temperature, respectively.

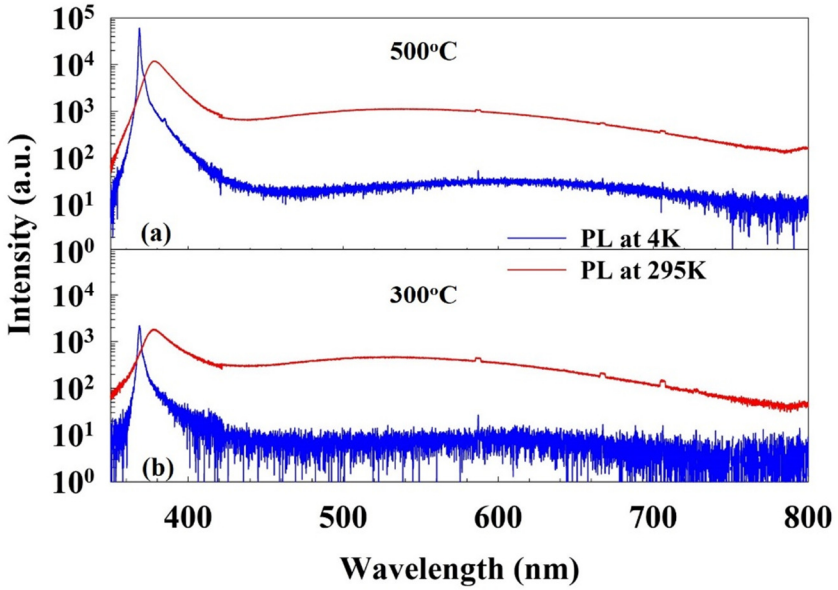

Figure 4.11: Photoluminescence spectra of ZnO/Si(100) samples grown at (a) 500°C and (b) 300°C. Blue and red lines are the PL responses in 4K and room temperature, respectively.

For the ZnO/Si(100) samples, the PL data, Figure 4.11, appeared to be improved compared to the ZnO/sapphire samples, Figure 4.10, as the defect band emission was almost negligible compared to the NBE emission. In addition, the NBE peak is demonstrated as highly dominated by excitonic emission, with a very low FWHM values of 8.56 meV and 143 meV at 4K and room temperature, respectively, for the sample grown at 500°C. At 4K, from Figure 4.11, the defect band, i.e., the green-yellow emission band, is almost less than 1% of the peak value of the NBE emission peak (368 nm = 3.35 eV). The RT-PL spectra shows comparable defect band in both the samples. Both the samples show red-shifts of about 80 meV in the NBE peaks at room temperature. Table 4.5 summarizes the PL data collected from the ZnO/Si(100) samples.

Table 4.5: Summary of photoluminescence data from ZnO/Si(100) samples.

ZnO/Si(100)	E_g at 4K (eV)	E_g at 295K (eV)	FWHM at 4K (meV)	FWHM at 295K (meV)
At 500°C	3.35	3.28	8.56	142.67
At 300°C	3.35	3.27	13.32	165.28

4.2.4 Electrical characterization

Hall effect data at room temperature were taken for the ZnO/sapphire and ZnO/Si(100) samples. Table 4.6 presents the room temperature bulk concentration, sheet concentration, resistivity, conductivity, mobility, and Hall coefficient for the five samples of ZnO discussed in this section.

Table 4.6: Room temperature Hall measurement data for ZnO/sapphire and ZnO/Si(100) samples grown at different substrate temperatures.

	ZnO/sapphire samples			**ZnO/Si(100) samples**	
Parameters	700°C	500°C	300°C	500°C	300°C
Bulk conc.	-6.91E+19	-7.81E+19	-3.48E+20	-1.354E+19	-1.373E+20
Sheet conc.	-6.08E+14	-6.87E+14	-6.96E+14	-1.625E+14	-9.338E+14

Resistivity	1.013E-02	8.998E-03	2.092E-03	4.302E-02	1.016E-03
Conductivity	9.87E+01	1.111E+02	4.781E+02	2.325E+01	9.842E+02
Mobility	8.92E+00	8.89E+00	8.575E+00	1.072E+01	4.474E+01
Hall co-eff.	-9.04E-02	-7.996E-02	-1.794E-02	-4.610E-01	-4.546E-02

As observed, unintentional *n*-type electrical transport was measured for the undoped ZnO samples using the van der Pauw four-point probe configuration. The carrier concentration, both bulk concentration (cm^{-3}) and sheet concentration (cm^{-2}) are observed to be in the same range of magnitude for all the samples. However, the samples grown on both substrates at 300°C, exhibit a 5x to 10x increase in electron density. This improvement is also continued in case of resistivity and conductivity, as these parameters are higher for the low temperature grown samples compared to the higher temperature ones. The samples were compared in terms of carrier (electron) mobility (cm^2/V-sec). ZnO/Si(100) grown at 300°C exhibits the highest mobility among the grown samples. To verify that no substrate influence is taking place, the *p*-type Si(100) wafer was itself characterized with the Hall effect measurement system at room temperature in search of any significant contribution in terms of carrier mobility. But, the wafers were significantly resistive with boron doping yielding a resistivity of 30 Ω-cm.

4.2.5 Summary of ZnO growth

In this section, growth of ZnO on sapphire and Si(100) substrates was demonstrated. Detailed structural, morphological, optical, and electrical characterization data were presented. The results show the capability of the PED tool for ZnO growth. The next section will focus on employing the PED technology for GaN growth of reasonably good quality ZnO.

4.3 Growth and characterization of GaN films

GaN was grown on sapphire, Si(111), Ge/Si(111) and ZnO/sapphire at different substrate temperatures ranging from 300^{o} to 700^{o}C. The objective is to demonstrate GaN growth at comparatively lower temperature using the pulsed electron beam deposition process. Optimized plasma conditions were used for growth of the samples mentioned above. The growth process parameters are presented in Table 4.7.

Table 4.7: GaN thin film growth parameter on different substrates.

	GaN/sapphire	**GaN/Si(111)**	**GaN/ Ge/Si(111)**	**GaN/ZnO/sapphire**
Substrate temperature	750^{o} C	600^{o} C	600^{o} C	ZnO: 300^{o} C GaN: 300^{o} C
Chamber pressure	20 mTorr (N_2)	14 mTorr (N_2)	14 mTorr (N_2)	ZnO: 7 mTorr (Ar) GaN: 15 mTorr (N_2)
Electron gun voltage	15 KV	15 KV	15 KV	ZnO: 11 KV GaN: 15 KV
Pulse rate	3 Hz	3 Hz	3 Hz	ZnO and GaN: 3Hz
Target-e^- gun tip distance	2 mm	2 mm	2 mm	ZnO and GaN: 2 mm
Target-substrate distance	5 cm	5 cm	5 cm	ZnO and GaN: 5 cm
Substrate rotation	30 rpm	20 rpm	20 rpm	ZnO and GaN: 20 rpm

4.3.1 Experimental Detail

The substrates were prepared according to the process mentioned in Section 3.3. Every growth run is preceded by obtaining a base pressure of ~10^{-7} Torr through overnight pumping following the cleaned samples loading process. After the substrates were heated to the desired temperature, sufficient time was provided to pump the chamber back down. Typically, the chamber pressure increased to the ~$5x10^{-6}$ Torr range due to outgassing from the substrate heater assembly. Four substrates were used in each growth run. Following the procedure in Section 3.5, the GaN plasma was

produced in a UHP N_2 environment and deposition began. The emission spectroscopy lines (two GaI and two NI lines) were keenly monitored to avoid any dominance of metal reactant Ga species. The growth parameters are listed in Table 4.7 for each sample. After the intended amount of pulses were fired, desired deposition being done, the samples were cooled in UHP N_2 environment and later in vacuum.

Grown samples were characterized using powder diffraction (XRD) first. This provides the growth orientation of the deposited GaN thin film. SEM images were taken for planar view and cross-section, followed by EDX and EBSD characterization. Then, RBS was performed on the samples followed by Hall effect and photoluminescence measurements. In the next sections, the characterization data will be presented.

4.3.2 Structural and morphological characterization

Figure 4.12 shows the SEM images (planar and cross section) of the GaN samples grown on different substrates at different temperatures. SEM imaging confirmed a rough surface morphology with the presence of GaN crystallites ranging in size from 30 nm to 300 nm for the GaN/sapphire sample, while smaller but more coalesced crystallites of 30- 50 nm size were observed for the GaN/Si (111) and GaN/Ge/Si (111) samples. Two different growth runs for the sapphire substrate and for the silicon substrates were used. The growth rate on sapphire was 0.370Å/pulse, while it was less for the growth on silicon substrates, ~0.15Å/pulse. On the other hand, for the GaN/ZnO/sapphire sample grown at 300^{o}C, there are small gains of 20-50 nm size on the surface, but the growth rate is significantly increased to 0.3125 Å/pulse. Although a rougher surface morphology is seen for low temperature grown GaN samples on bare

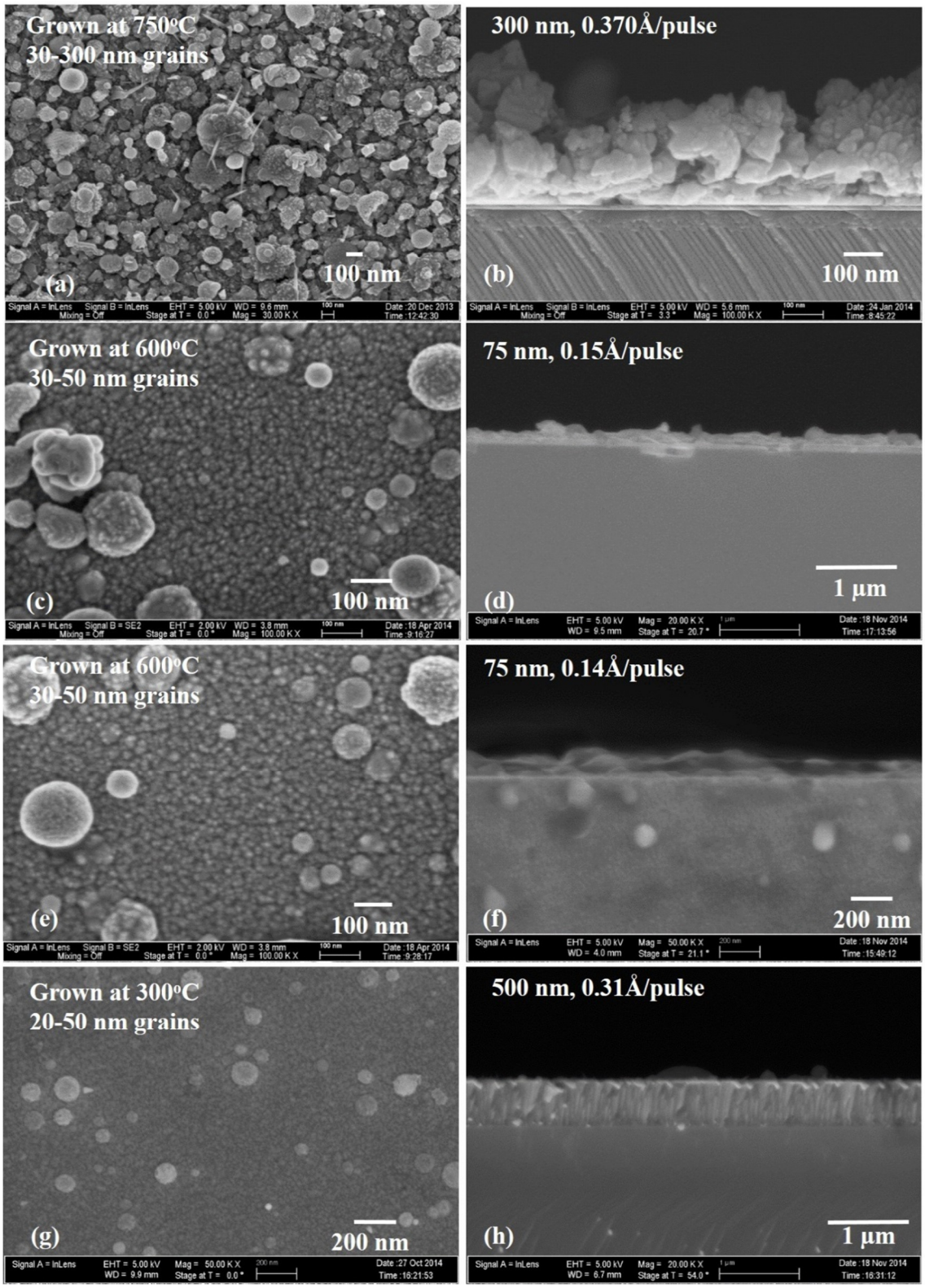

Figure 4.12: SEM images of GaN on sapphire- grown at 750°C: (a) planar, (b) cross-section, on Si(111) at 600°C: (c) planar, (d) cross-section, on Ge/Si(111) at 600°C: (e) planar, (f) cross-section, and on ZnO/sapphire at 300°C: (g) planar, (h) cross-section.

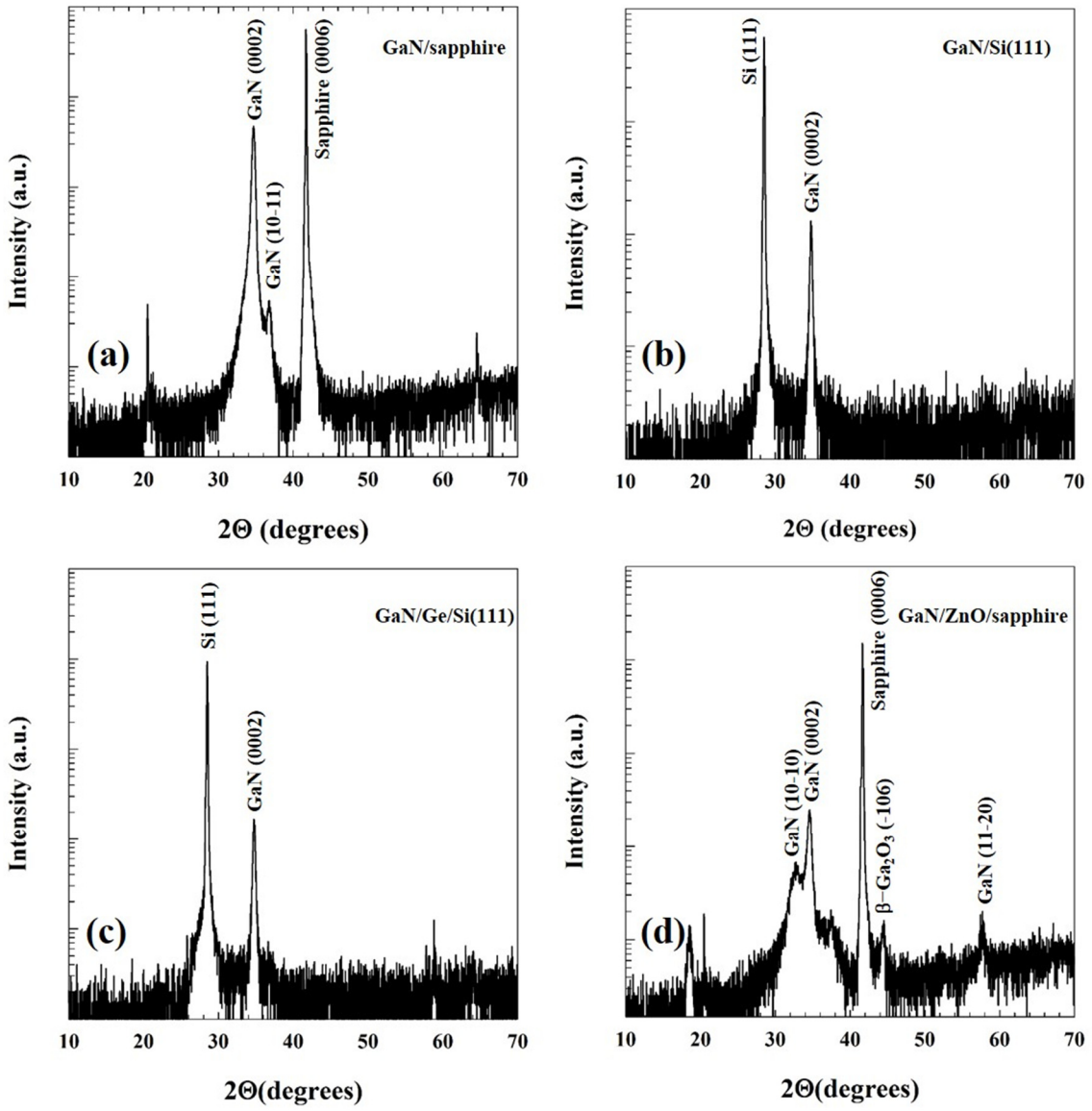

Figure 4.13: XRD scan (powder diffraction) for (a) GaN/sapphire, (b) GaN/Si(111), (c) GaN/Ge/Si(111), and (d) GaN/ZnO/sapphire.

sapphire or silicon substrates, it appears that insertion of a 15 nm ZnO buffer layer prior to GaN growth (in the GaN/ZnO/sapphire sample) helps in obtaining a smoother GaN surface even at a lower temperature.

Powder diffraction x-ray scans from $2\theta = 0°$ to $2\theta = 70°$ for the GaN on sapphire sample showed only two other peaks, besides the peaks from the sapphire, near $2\theta = 34.6°$. They consist of a stronger peak at 34.668° and a much weaker peak at 36.903°.

These peaks correspond to the (0002) and (10-11) orientations for GaN, respectively. XRD scans for the GaN/Si (111) and GaN/Ge/Si (111) showed only a polar GaN (0002) peak at 34.7°. Thus, no non-polar plane GaN was observed in these samples. To verify the growth direction of the samples electron back scattered diffraction (EBSD) scanning was performed on the GaN samples grown on sapphire and silicon substrates, and the results are shown in Figure 4.14. From the analyzed data, the *d*-spacing of planes in different directions are obtained for the GaN samples. Reflection intensity is highest for the polar *c*-plane in (0002) direction. The reflection data along with the *d*-spacing are shown in Tables 4.8 and 4.9 for the samples discussed in this section. As shown in the EBSD reflections, the dominant plane is the *c*-plane, i.e., (0002) plane with the highest of the diffracted intensity from layers grown on silicon substrates. Powder diffraction on GaN/ZnO/sapphire showed two other GaN planes besides the (0002) plane, the (10-10) and (11-20) plane, $2\theta=32.412^{o}$ and 57.915^{o}, respectively. An additional peak corresponding to β-Ga_2O_3 (-106) was also observed at $2\theta = 44.87^{o.}$ This is assumed to originate due to the interaction of high energy Ga species with the previously deposited ZnO layer (15 nm buffer layer) on the sapphire substrate. This sample was studied using the EBSD technique to analyze the growth direction of the GaN layer on the 15 nm thick ZnO buffer layer on sapphire. EBSD maps of selected scan areas on both the GaN layer and the ZnO/sapphire layer are presented, respectively, in Fig. 4.15(a) and 4.15(b). These EBSD maps verify dominance of *c*-plane GaN growth on the ZnO/sapphire at a

300°C.

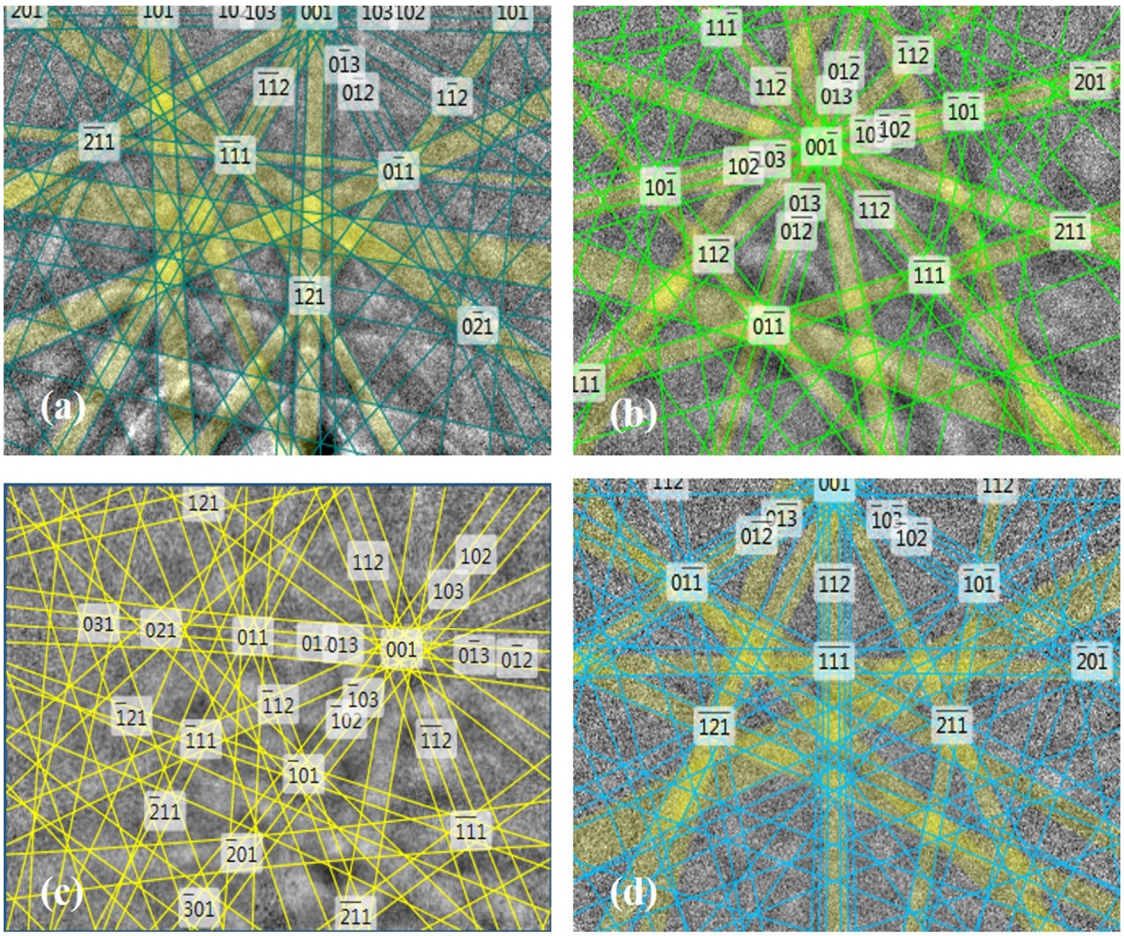

Figure 4.14: Kikuchi patterns generated from electron back-scattered diffraction (EBSD) from (a) GaN/sapphire, (b) GaN/Si(111), (c) GaN/Ge/Si(111), and (d) GaN/ZnO/sapphire.

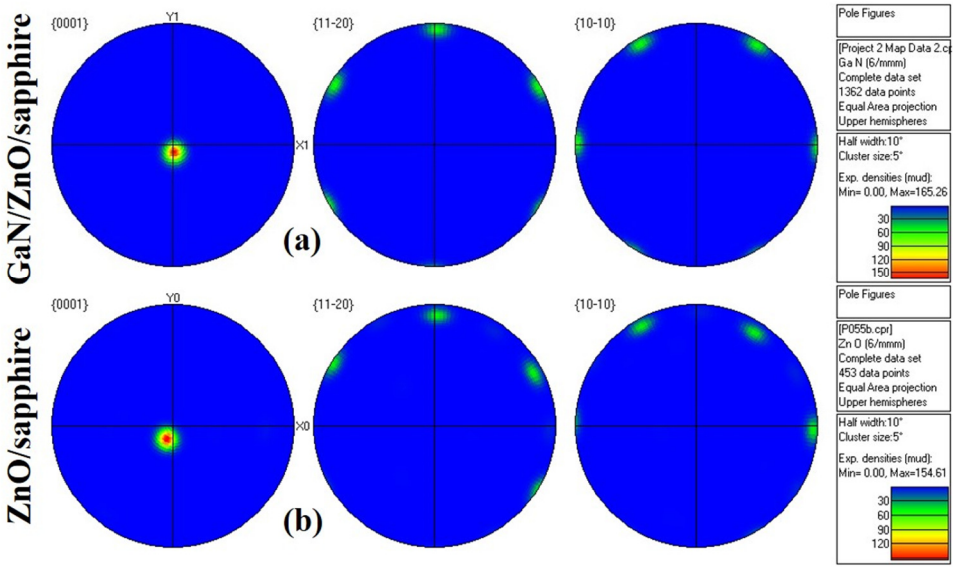

Figure 4.15: EBSD mapping of a selected area from (a) epilayer: GaN/ZnO/sapphire and (b) buffer: ZnO/sapphire.

Table 4.8: Relative diffraction intensity from crystal planes of GaN samples.

hkil **plane**	**Diffraction intensity (%)**			
	GaN/sapphire	**GaN/Si(111)**	**GaN/Ge/Si(111)**	**GaN/ZnO/sapphire**
0002	100.0	100.0	100.0	100.0
11-20	70.6	69.4	67.0	68.3
2-1-10	70.6	69.4	67.0	68.3
1-210	70.6	69.4	67.0	68.3
1-100	46.4	45.5	44.0	45.4
10-10	46.4	45.5	44.0	45.4
01-10	46.4	45.5	44.0	45.4
10-13	39.0	37.9	35.6	37.6
01-1-3	39.0	37.9	35.6	37.6
01-13	39.0	37.9	35.6	37.6

Table 4.9: Distance between planes (observed in EBSD scan) of GaN samples.

hkil **plane**	**Distance between adjacent planes (Å)**			
	GaN/sapphire	**GaN/Si(111)**	**GaN/Ge/Si(111)**	**GaN/ZnO/sapphire**
0002	2.5833	2.5945	2.5927	2.5595
11-20	1.5902	1.5950	1.5946	1.5675
2-1-10	1.5902	1.5950	1.5946	1.5675
1-210	1.5902	1.5950	1.5946	1.5675
1-100	2.7543	2.7627	2.7619	2.7150
10-10	2.7543	2.7627	2.7619	2.7150
01-10	2.7543	2.7627	2.7619	2.7150
10-13	1.4602	1.4661	1.4652	1.4447
01-1-3	1.4602	1.4661	1.4652	1.4447
01-13	1.4602	1.4661	1.4652	1.4447

Rutherford backscattered diffraction spectroscopy (RBS) was used to study the thin film and substrate interface (Figure 4.16) with a 1.5 MeV $^4He^+$ ion beam from a Van de Graaff accelerator. As appears in Fig. 4.16(a) for the GaN/sapphire sample, the interface of the GaN and sapphire (Al_2O_3) shows a not very distinctive boundary between the substrate and the thin film, as the Al tail is slightly inclined. This might be caused from some Al-Ga alloy formation in presence of high energy Ga species in the plasma and a 750^{o}C substrate temperature. On the other hand, the samples on silicon-based substrates, GaN/Si(111) and GaN/Ge/Si(111) show distinct thin film and substrate boundaries. Using the RBS simulation software, the Ga:N ratio was calculated very close to 1:1 in both GaN/Si(111) and GaN/Ge/Si(111) (Figure 4.16(b) and 4.16(c)). Comparing the RBS spectra for GaN/sapphire with that published in [52], the RBS channeling is significantly improved in PED grown GaN/sapphire samples at a lower temperature than that reported in [52].

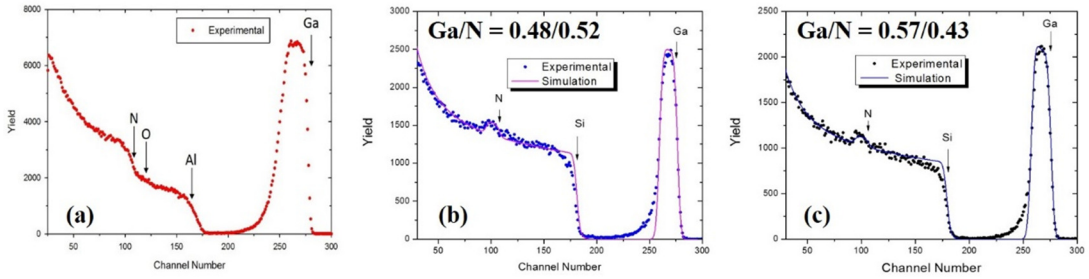

Figure 4.16: RBS scanning of (a) GaN/sapphire,
(b) GaN/Si(111), and (c) GaN/Ge/Si(111).

4.3.3 Optical characterization

Photoluminescence (PL) was done on GaN/Si(111), GaN/Ge/Si(111), and GaN/ZnO/sapphire samples using a 325 nm He-Cd laser. Data were taken at both 4K and 295K sample temperatures and are presented in Figure 4.17. It appears that GaN/Si(111) shows more intense near band edge (NBE) emission at 368 nm compared

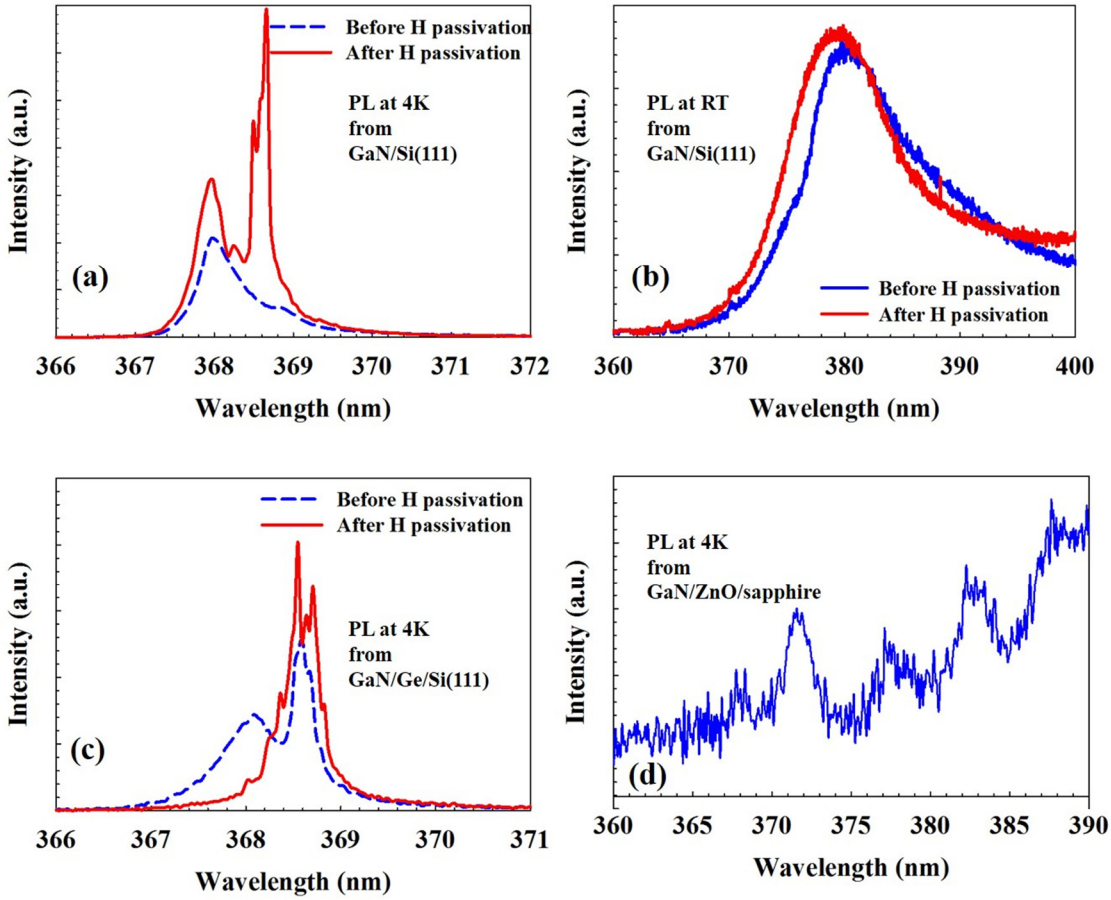

Figure 4.17: Photoluminescence spectra of (GaN/Si(111)) at (a) 4K, (b) 295K, (GaN/Ge/Si(111)) at (c) 4K, and (GaN/ZnO/sapphire) at (d) 4K. (Blue lines: PL spectra before H passivation, and Red lines: PL after H passivation).

to GaN/Ge/Si(111) as appears in Figure 4.17(a) and 4.17(c). However, much broader RT emission was observed from GaN/Si(111) which is assumed to be caused by the emission due to increased phonon scattering at higher temperature. The GaN/Ge/Si(111) sample did not show any distinguishable PL emission at room temperature. To improve the luminescence, these GaN samples on silicon-based substrates were passivated using H implantation. As can be seen, the emission (at 4K, Fig. 4.17(a)) from as-grown GaN/Si(111) includes mostly 368.0 nm photons (3.378 eV), while after H passivation, in parallel to the intensity increase of the 368.0 nm peak, a new and much stronger emission peak is observed at 368.6 nm (3.372 eV). On the

other hand, before H passivation, the as-grown GaN/Ge/Si(111) sample (at 4K, Fig. 4.17(c)) showed NBE emission at both 368.0 nm and 368.6 nm. After H passivation the intensity of the 368.6 nm peak increases significantly, while the 368.0 nm emission was reduced, however, this sample did not show any PL emission at room temperature even after H passivation. PL at room temperature is presented for GaN/Si(111) (Fig. 4.17(b)), demonstrating red shift in the emission centering at 380 nm (3.26 eV) with a broader FWHM due to increased phonon scattering at the higher lattice temperature. After H passivation a small amount of increased intensity with blue shift is observed for the GaN/Si(111) sample with a slightly reduced FWHM. Comparing the PL emission from the GaN/Si(111) and GaN/Ge/Si(111) samples, it appears that GaN grown on a bare Si(111) substrate demonstrates better optical performance than GaN grown on a Ge/Si(111) substrate as evidenced by stronger PL emission at 4K and distinguishable band-edge emission at room temperature (although red shifted and broadened due to phonon scattering). The GaN/ZnO/sapphire sample was studied at 4K for photoluminescence. Weak PL emission was observed at 371.5 nm, which is slightly red shifted as compared to the NBE observed from the other samples. Room temperature PL emission from this sample was not observed.

4.3.4 Electrical characterization

The GaN samples on silicon substrates, GaN/Si(111) and GaN/Ge/Si(111), were also characterized using Hall effect measurements (Figure 4.18). Of the two samples, GaN/Si(111) shows a higher electron mobility (5,386 cm^2/V-sec at T~100 K) than the GaN/Ge/Si(111) sample, (2,713 cm^2/V-sec at T~100K). The mobility is reduced in both

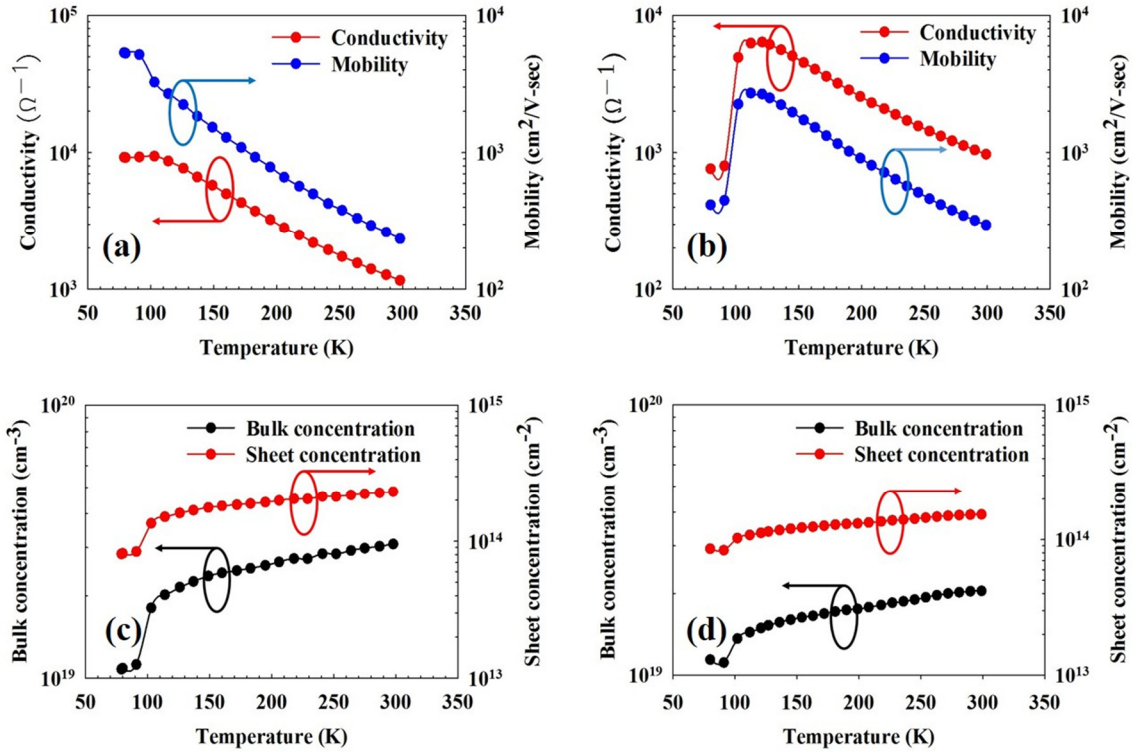

Figure 4.18: Temperature dependent conductivity and mobility of (a) GaN/Si(111) and (b) GaN/Ge/Si(111). Temperature dependent bulk and sheet carrier concentration of (c) GaN/Si(111), and (d) GaN/Ge/Si(111).

samples at room temperature as both samples demonstrate a mobility of ~300 cm^2/V-sec at 300K due to phonon scattering. The Si(111) and Ge/Si(111) substrates were also characterized using Hall effect measurement and both the substrates showed low mobility assuming no contribution to the mobility of the GaN layer. In addition, the silicon substrates are *p*-type, which results in a *pn* junction at the thin film-substrate interface (creates a depletion region) opposing the concept of any carrier contribution from the substrate. Both the samples show high bulk and sheet carrier concentration in the order of ~$5x10^{19}/cm^3$, and ~$5x10^{13}/cm^2$ – $10^{14}/cm^2$, respectively. The PED grown GaN films demonstrate a RT sheet carrier concentration of ~1.5x 10^{14} cm^{-2} for GaN/Si(111), while for GaN/Ge/Si(111) this value is ~ 10^{14} cm^{-2}. Such high carrier

concentration is assumed to originate from the defects associated in the grown film from N vacancies taken place during growth.

4.3.5 Summary of GaN growth

In this section, PED technology has been demonstrated for low temperature growth of GaN on different kinds of cost-effective substrates. Grown samples have been characterized to determine structural, morphological, optical and electrical properties. From detail analysis it appears that the GaN samples grown using PED process at low temperature demonstrate their optical and electrical performance which can be improved further. To compare among different samples grown, it appears that the GaN samples grown on silicon based substrates show better properties compared to the samples grown on sapphire based substrates. Although the growth rate was comparatively slower on silicon based substrates, the presence of planes other than the polar (0002) plane was absent in the silicon based samples. Also, RBS channel profiling showed better interface between film and substrate in case of the silicon based samples. PL characterization showed that GaN/Si(111) and GaN/Ge/Si(111) showed better luminescence compared to the GaN samples on sapphire based substrates, to be more specific, the GaN/Si(111) showed better luminescence of all the samples.

4.4 Growth and characterization of AlN nanowires

AlN nanowires were grown on sapphire and Si(111) at substrate temperatures of 500°C and 550°C, respectively, in a N_2 environment without any surface pre-treatment, i.e., pre-nitridation. Hexagonal faceted high aspect ratio AlN nanowires were found on both sapphire and silicon substrates, which were identified as *c*-plane oriented AlN structures. The growth process parameters are presented in Table 4.10.

Table 4.10: Growth parameters for AlN NW.

Base pressure	~ 6.57 x 10^{-7} Torr
Electron voltage	15 KV
Pulse rate	1 Hz
Target to substrate distance	5 cm
Source to target distance	2 mm
Process gas pressure	20 mTorr (UHP N_2)
Number of pulses	3600 (1 hour)
Heater bulb temperature	920^{o}C
Substrate temperature	500^{o}C (sapphire) and 550^{o}C (Si)

4.4.1 Experimental detail

The substrates were prepared according to the process mentioned in Section 3.3. Every growth run was preceded by obtaining a base pressure of ~10^{-7} Torr through overnight pumping following the substrate loading process. After the substrates were heated to the desired temperature, sufficient time was provided to pump the chamber back down ~6.57 x 10^{-7} Torr after heating the substrates. Two sapphire and two Si(111) coupons were used for each growth run. In the vacuum, the substrates were backside heated with high intensity optical lamps and were rotated continuously (10 rpm) to attain uniform heat distribution. UHP nitrogen was fed to the chamber to attain a working pressure, and the electron source was set for firing. Following the procedure in Section 3.5, an AlN plasma was produced in UHP N_2 environment, and deposition began. The emission spectroscopy lines (Al, NI, and NII lines: Figure 4.19) were keenly monitored to avoid any dominance of metal reactant Al species. Table 4.10 contains the numerical values of the key deposition parameters for this process. After the deposition was completed, the wafers were cooled in the nitrogen environment.

The samples were first imaged optically (using Nomarski microscopy) revealing the presence of long nanowires. Then SEM imaging was done using a Zeiss Neon high resolution scanning electron microscope. SEM images were taken for planar view and

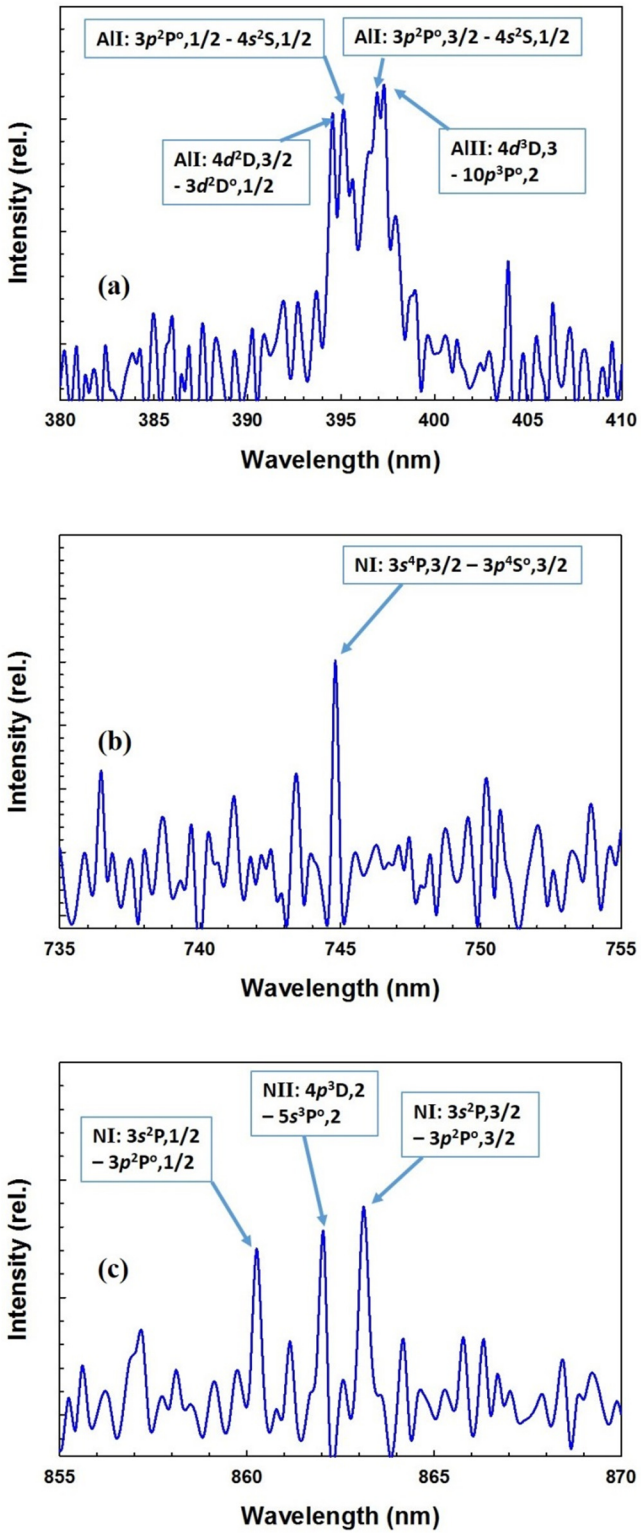

Figure 4.19: Emission spectra of aluminum lines (a), and nitrogen lines (b) and (c).

cross-section, followed by EDX and EBSD characterization. Samples on sapphire substrates showed larger AlN nanowires compared to the samples on silicon. A possible reason is that while growing on sapphire the III-nitrides experience a 30^{o} rotation with respect the substrate that ultimately results in a reduced lattice mismatch with sapphire going down to 13.3% from 34.6%, while the lattice mismatch is 18.49% with Si(111). Nanowire walls appeared to be hexagonally faceted. Grown samples were taken for characterization using powder diffraction (XRD). This tells about the growth orientation of the deposited AlN NW. In the next sections, the characterization data will be presented.

4.4.2. Structural and morphological characterization

Figure 4.20 shows the AlN nanowires grown on sapphire and Si(111) substrates. Abrupt growth of hexagonal faceted AlN NWs is observed on both types of substrates. It is clearly observed that the nanowire dimensions are higher with the sapphire

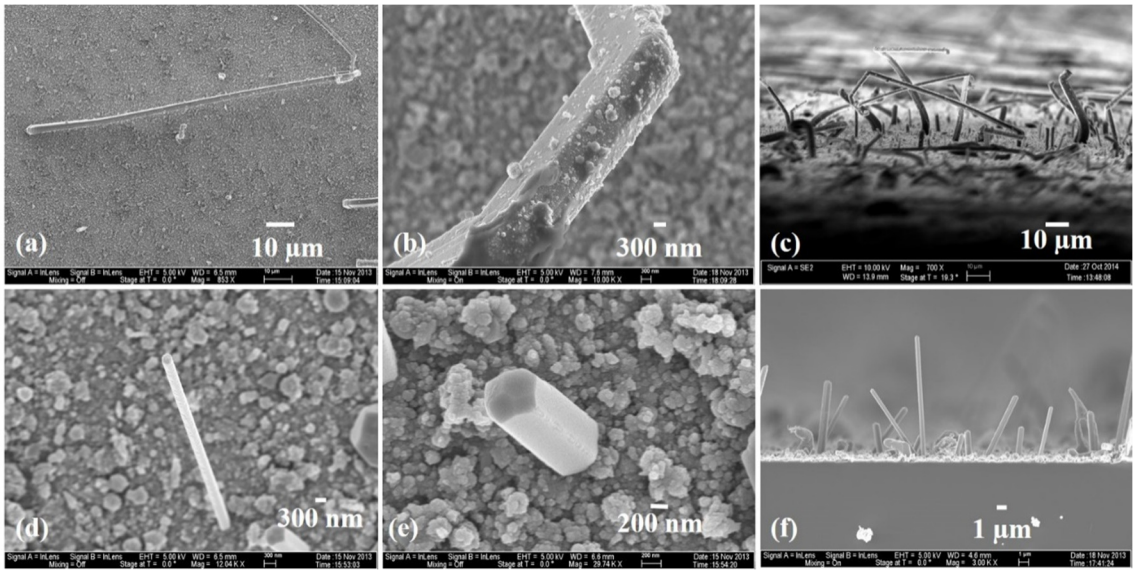

Figure 4.20: SEM image of AlN nanowires on sapphire: (a) a single nanowire showing length of > 100 µm, (b) segment of a NW with diameter of ~ 2.5 µm, and (c) cross-section of AlN NW on sapphire sample. AlN nanowires on Si (111): (d) a single nanowire showing length.

substrate samples, which is considered a more native and matching substrate for III-nitride structure growth compared to Si(111).

EDX analysis was performed to study the chemical stoichiometry of a nanowire (Focusing at different points of the nanowire). A nanowire (grown on sapphire) of ~25 µm length was chosen for this analysis as shown in Figure 4.21(a). Three points of the nanowire were used as data points to collect the element atomic percentage at those points (Figure 4.21): (Spec 1) at the base of the NW (~1 µm from base), (Spec 2) at the middle of the NW (~12 µm from base), and (Spec 3) at the tip of the NW (~25 µm from base). It appears that the Al:N ratio changes along the NW length. At the base region, the stoichiometry is highly metal Al rich. As analysis is moved along the NW length to the tip of the NW, the Al:N ratio attains a stoichiometric = 1:1 value, as shown in Figure 4.22.

The NW sample on sapphire was scanned using x-ray powder diffraction to determine the growth orientation of the NWs. The XRD scan, Figure 4.23, shows only an Al(111) peak at 37.56^{o}, along with the sapphire(0006) peak at 42^{o}. No AlN peak was observed in the XRD scan. Thus, to verify the identity and crystal orientation of the micron scale NWs on both the samples, they were scanned with EBSD to analyze each NW for their lattice parameters and growth orientation. The EBSD scan results are shown in Figure 4.24 along with the relative diffraction intensity and plane spacing presented in Table 4.11.

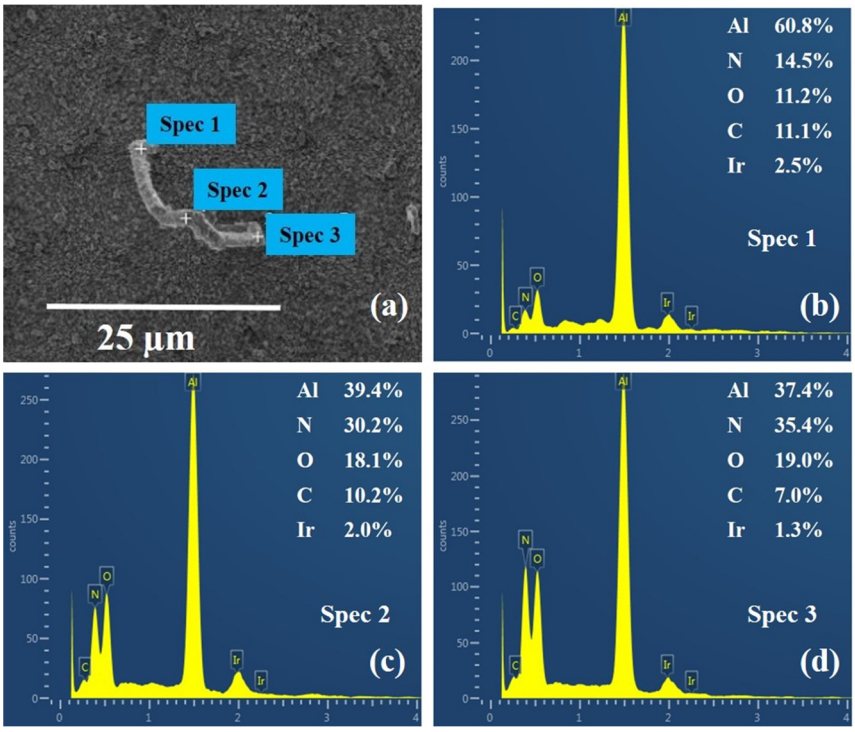

Figure 4.21: (a) An AlN NW on sapphire, subject to EDX analysis; EDX scan at (b) the base: Spec 1, (c) middle of the NW: Spec 2, and (d) tip of the NW: Spec 3.

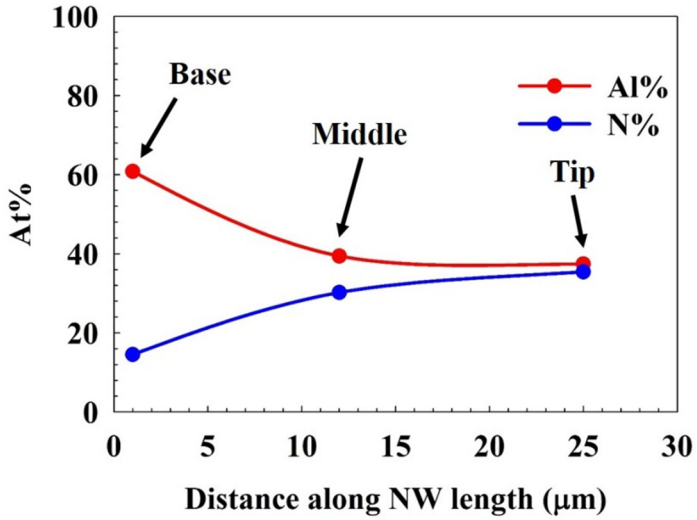

Figure 4.22: Changes in Al and N atomic weight percentage along an AlN NW length.

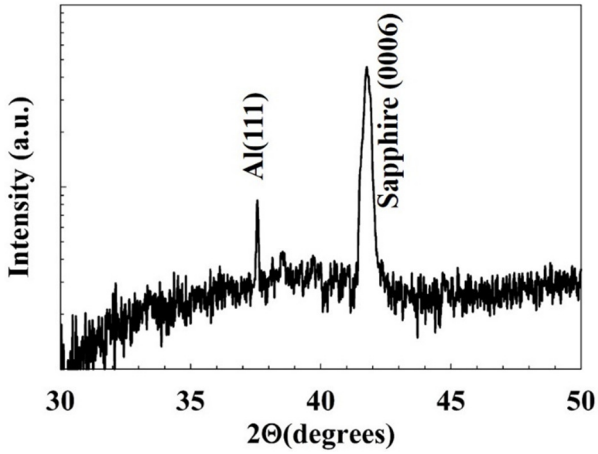

Figure 4.23: X-ray powder diffraction scan of AlN NW on sapphire.

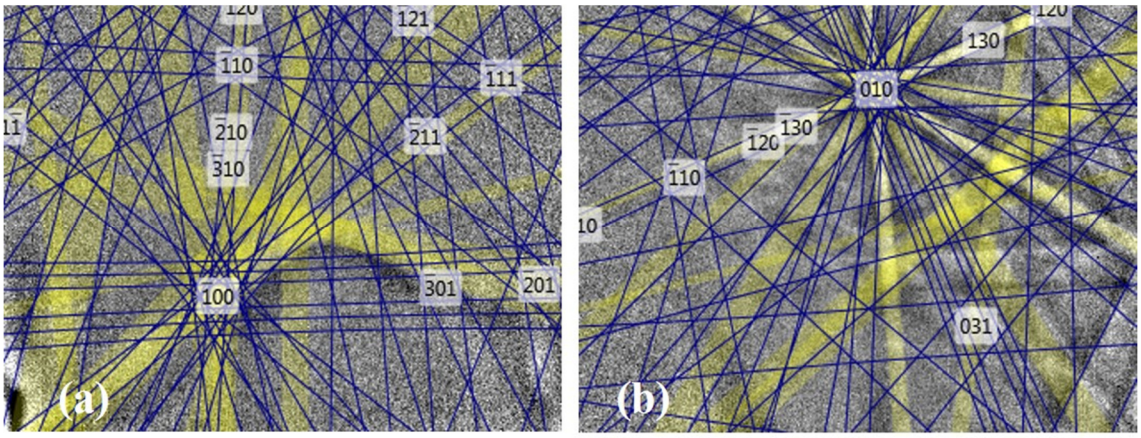

Figure 4.24: Kikuchi patterns generated from electron back-scattered diffraction (EBSD) in (a) AlN NW on sapphire and (b) AlN NW on Si(111).

Table 4.11: Relative diffraction intensity and distance between two adjacent planes in AlN NW/sapphire and AlN NW/Si(111).

hkil **plane**	**Diffraction intensity (%)**		**Distance between adjacent planes (Å)**	
	AlN/sapphire	**AlN/Si(111)**	**AlN/sapphire**	**AlN/Si(111)**
0002	100.0	100.0	2.5155	2.5155
11-20	56.8	56.8	1.5405	1.5405
1-210	56.8	56.8	1.5405	1.5405
2-1-10	56.8	56.8	1.5405	1.5405
1-100	49.5	49.5	2.6682	2.6682
10-10	49.5	49.5	2.6682	2.6682
01-10	49.5	49.5	2.6682	2.6682
10-13	27.8	27.8	1.4199	1.4199
01-1-3	27.8	27.8	1.4199	1.4199
01-13	27.8	27.8	1.4199	1.4199

As shown in Figure 4.24(a) and (b), the Kikuchi patterns generated from the EBSD scans show diffraction from a hexagonal wurtzite crystal structure. The lattice plane spacing matches with the polar plane (0002) spacing and the other semi-polar and non-polar plane spacings. The majority of the localized electron diffraction intensity is observed from the (0002) plane, and this confirms that the growth direction of the AlN NWs on both substrates is in the *c*-plane orientation. This also clarifies the confusion from powder diffraction data shown in Figure 4.23. Since, the number of wurtzite *c*-plane AlN NWs are considerably low, the diffracted x-ray intensity off the NW structures are negligible compared to the diffraction from the prior deposited Al(111) thin film. Thus, the more diffuse x-ray diffraction shows only the Al(111) peak on the substrates.

4.4.3 Summary on growth of AlN NW

This section demonstrates growth of wurtzite AlN NW on sapphire and Si(111) at comparatively low temperatures than reported so far. In addition, this report is the first demonstration of such large scale dimension of AlN NW grown at such a low temperature. It is assumed that in the early stages of plasma generation, at low substrate temperature, the metal aluminum gets condensed on the substrate surface without bonding atomic nitrogen to it, forming a metal Al layer on the substrate (as revealed in Figure 4.23). This condensed metal film acts as a low temperature influenced self-catalytic layer for NW growth. Thus, the PED process demonstrates growth of AlN NW without any prior metal deposition to initiate NW growth.

4.5 Summary

This chapter presents the growth and characterization of wide bandgap ZnO, GaN, and AlN NWs on cost effective sapphire, Si(111) and Si(100) substrates. The properties show that PED tool is capable to grow these materials with competitive optical and electrical properties along with highly directional structures.

Chapter 5 : Future prospects of pulsed electron beam deposition process

5.1 Motivation

Chapter 2 reviewed the importance and potential applications of wide bandgap semiconductor materials for LEDs in the lighting industry and transistors for radar and power electronics applications. It is highly desirable to have a low temperature growth procedure to obtain WBG materials since that would allow using of lower cost substrate materials. This dissertation presented preliminary results on wide bandgap material growth using from a plasma generated using high energy electron pulses. The plasma was optimized using optical emission spectroscopy to identify reactive species, and growth was performed on substrates that included sapphire, silicon and germanium coated silicon. Although, some promising results were presented in Chapters 3 and 4, the pulsed electron beam deposition (PED) process still needs further development to produce material of sufficient quality to be suitable for device fabrication work.

This chapter will present some proposed improvements (based on observations and experiences while preparing this dissertation) as well as some guidelines for future experiments that should improve the performance of the equipment, and most importantly can lead to growth of WBG materials for development of novel device fabrication methods that involve use of silicon-based substrates with engineered buffer layers that allow remove of epitaxial layers from the growth substrate.

5.2 Modification of the existing PED system

As observed during growth of the specimens discussed in Chapter 4, the surface of the epilayers are rough compared to epitaxial films grown by commercial PVD and CVD processes as described in the literature. Commercial MOCVD and MBE processes employ ultraclean wafers, such as, Shiraki cleaned [53] silicon substrates. Due to budget constraints it was not affordable to engage a load-lock chamber to the PED setup to ensure very clean substrate surface prior to material deposition. As a result, no matter how cautious the cleaning processes were involved, any clean substrate was exposed to atmospheric environment in the clean room (at least for 2 minutes) prior to loading in the chamber for overnight pumping. This, for sure, had contaminated the substrate surface with at least nm scale oxide layers. However, if Shiraki cleaned wafers were used, it might not be of great utility since the vacuum could reach only up to 1.5×10^{-7} Torr, not enough to maintain an unoxidized surface following a high temperature oxide desorption step as is possible in an ultra-high vacuum MBE system [54] [55].

During growth, a major challenge comes forth from the first few hundred pulses of the plasma. It could not be managed to have a shutter on the substrate manipulator (containing the samples). As a result, the substrate surfaces were exposed to the plasma from the very beginning of its generation. This is of great importance because when the samples are loaded in the chamber, no matter how much positive nitrogen pressure is applied in the chamber when the growth chamber is opened, the target materials are exposed to the atmosphere and its components at some extent. This atmospheric exposure contaminates the top surface of the target material, which later contributes to plasma generation through electron pulse. When the high energy electrons hit the target

surface, the first few hundred pulses actually ablate the contaminated target surface, creating a plasma containing "unwanted" reactive species. Since, the existing PED configuration is not equipped with a shutter to guard the substrate portion from any unwanted direct exposure, these plasma pulses containing contamination are deposited on the substrate as the first few monolayers of the grown film. Thus it can be depicted that the studied samples in this dissertation have a great chance of not having a very good initial nucleation layer. However, although with a great probability of having contaminated nucleation layer, the grown samples have shown impressive results of wide bandgap material growth using the PED technique. The PED-grown AlN nanowires described in Chapter 4, for example, provide solid proof that it is possible to grow crystalline nitride materials with PED. Thus, it is assumed with confidence that associating a shutter with a linear feedthrough will positively impact the future growths, as it could reduce the incorporation of the plasma containing contamination (from target surface) from depositing as the first few monolayers on the substrate materials.

Another important equipment issue arises from the lack of controlled pumping in the molecular regime. Since, the PED equipment has two gauges to monitor pressure in the electron gun-tip region (using a pirani gauge) and near the opening of the turbo-molecular pump region (for estimating the base pressure, using an ion gauge associated with convectron gauge), significant pressure differential is observed as background process gas is fed to the chamber. The process gas pressure increased from ~15 mTorr (from the target surface/gun-tip region, using pirani gauge) to ~250mTorr (at the turbo molecular pump, using convectron gauge). As mentioned earlier, a base pressure of ~10^{-7} Torr is obtained before the growth process is initiated, through overnight pumping.

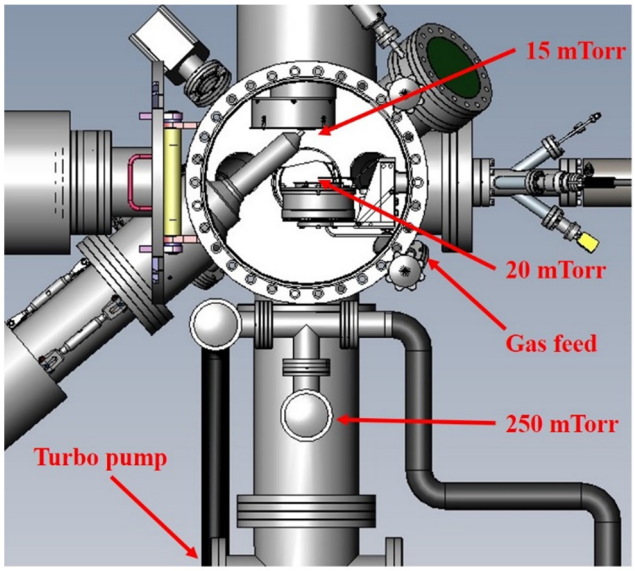

Figure 5.1: PED chamber with pressure variation during growth.

When background gas, UHP N_2 or Ar, is fed to the chamber for growth, the gauge readings are different from top to bottom. As seen in Figure 5.1, based on observed pressure readings, while attempting to obtain a pressure of 15 mTorr UHP N_2 in the gun-tip area, a lot of gas had to be fed to the chamber, approximately 180-200 sccm. This caused a lot higher pressure in the lower portion of the chamber, and obviously a higher pressure in the substrate region. As mentioned, the pressure along the path from the source of the plasma to the convectron gauge equipped ion gauge increases from ~15 mTorr to ~250 mTorr. It is very important since the presence of background gas can change the average energy of the arriving plasma components to the substrate. If the distance between the target (origin of the plasma) and the substrate is x, the plasma flux parameters change drastically with changes in this distance, and thus it is very important for thin film growth. At a characteristic distance L_0 from the plasma source point on the target surface, the plasma flux loses its unidirectional behavior, and the plasma becomes a subject to scattering, thermalization and

deceleration. It has been reported that the optimum condition for film growth exists in the vicinity of the distance $x = L_0$ [56] [57].

Figure 5.2 shows the study by Strikovski *et al* [58] change of directional, V, and thermal velocities, V_T, of the plasma ensemble at a normalized distance *L/R* from the target surface. They used the following equations:

$$V/V_0 = (1 + x^3)^{-1} \tag{5.1}$$

$$V_T/V_0 = x^{3/2}[3(1 + x^3)(1 + \mu x^3)]^{-1/2} \tag{5.2}$$

Here, V_0 is considered the initial velocity of the uninterrupted gas atoms as they propagate. Considering the deceleration and thermalization processes, using conservation of momentum and energy in an adiabatic process, V is defined as the velocity of the directed movement of the plasma ensemble. V_T is the thermal velocity of the particles defined as. Here, $\mu = M/m$ is the atomic mass ratio between the target material and the gas with $x = L/R$ being the normalized distance. R is defined as the distance after which the total mass of the gas atoms become equal to the mass of ejected atoms during ablation. Strikovski *et al* [58] compared the directional and thermal velocities of the plasma particles with respect to changes in the normalized distance (*L/R*) from the target surface, as presented in Figure 5.2.

A characteristic point is determined in the plot, which is the intersection of the two graphs and it demonstrates the overcoming of the thermal expansion of the plasma ensemble over the forward moving particles. This has been analyzed with assumption that there exists roughly similar pressure throughout the chamber. However, it has been

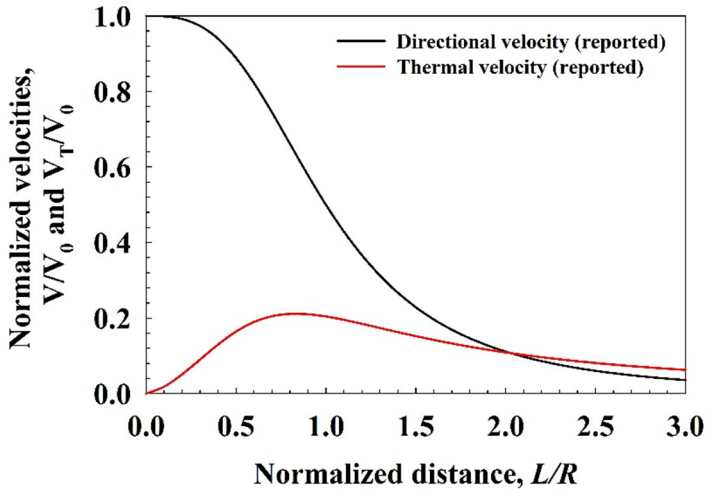

Figure 5.2: Variation of directional and thermal velocities with respect to changes in the normalized distance from the target surface.

seen in the research described in this dissertation that the pressure differential is significant in rising starting from the target surface (electron gun-tip area) towards the substrate. As it appeared from study, this pressure rise is an increment rising from ~15 mTorr at the target surface to ~20 mTorr on the substrate, as shown in Figure 5.1. This rise in pressure is explained by the following equation, formulated according to the observed pressure data from the PED chamber:

$$P = 15e^{x/15} \tag{5.3}$$

In addition to the pressure rise, the plasma ensemble temperature also experiences massive amount of temperature decay (exponential) from origin (target surface) to thin film deposition spot (substrate region). Based on the physics described by [58] , a simple exponential temperature decay model is formulated, and this explains the origin of highly energized plasma components (with a characteristic energy of 5 eV, corresponding to T = 58,000 K) cooling down to 873 K (600 ^{o}C) during growth:

$$T = 58000e^{-x/1.1915} \quad (5.4)$$

Applying these two equations, and the exponential decay hypotheses, the particle mean free path is calculated throughout the region from the target surface to the substrate, and surprisingly it appears that the mean free path reduces from 530 mm (on the target surface) to 0.5 mm (on the substrate) under the influence of a background gas, as used in the PED system. This massive reduction in mean-free path ultimately reduces the blending capability of the plasma reactants. Another great possibility is that under the strong influence of a 300 l/sec turbo molecular pump, to maintain a pressure in the mTorr range, a massive amount of gas needs to be fed to the chamber (180-200 sccm). Such a high amount of gas actually scatters the plasma components more, and most importantly recombines the lighter plasma components, such as, the atomic nitrogen, much faster leaving a high population of the heavier metal components somehow active enough to condense as a thin film on the substrate (Figure 3.10 and Figure 3.11). Figures 5.3 shows the changes in chamber pressure, plasma particle temperature, and mean-free path distance from the target surface to the substrate. These results have been applied to the plots shown in Figure 5.2, and distinguishable change has been observed as shown in Figure 5.4.

It appears from Figure 5.4, the meeting point of the directional and thermal velocities is at the same value of *L/R* = 2.0, as demonstrated by Strikovski *et al* [58]. However, the value of normalized velocities for both categories were scaled down by a factor of three, slowing down atomic species as they traverse path further towards the substrate.

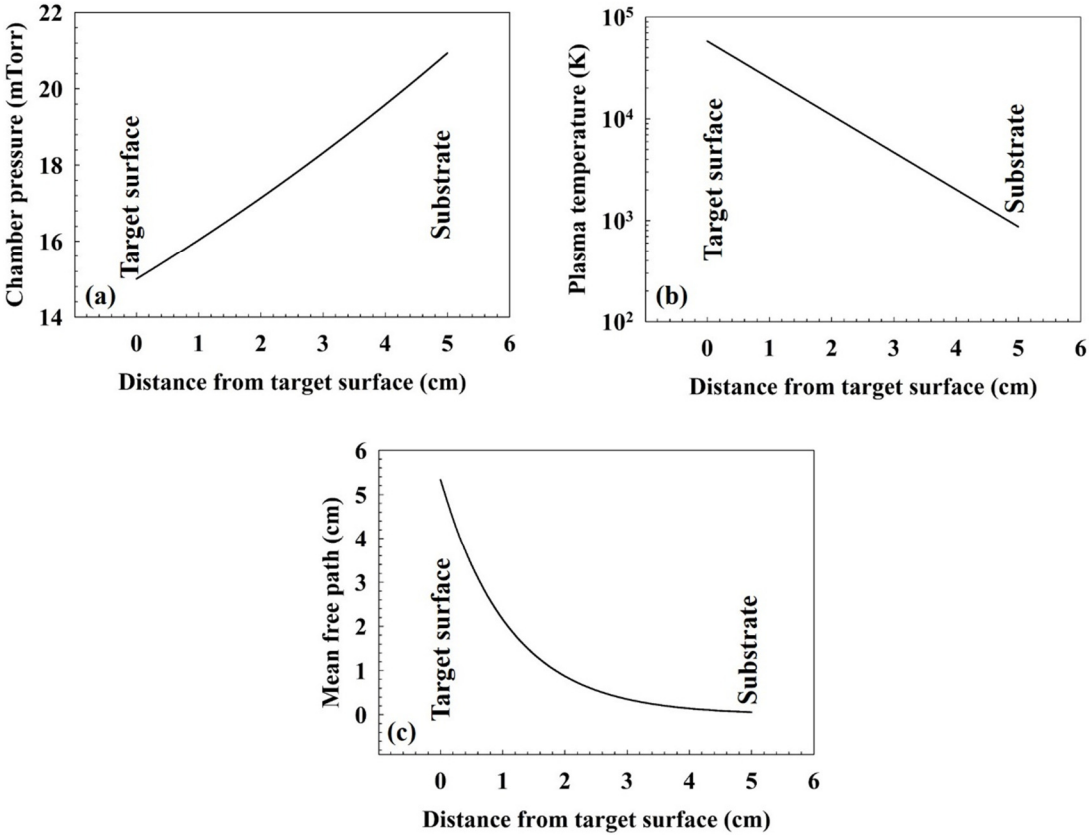

Figure 5.3: Changes in pressure, plasma temperature, and mean-free path from target surface to substrate in the PED system.

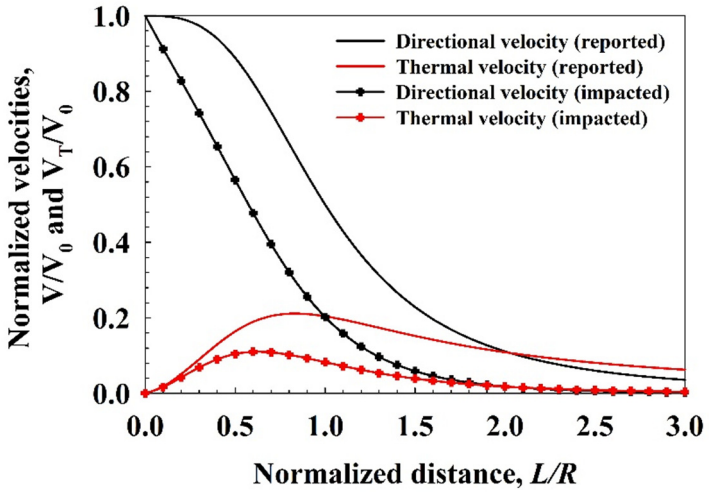

Figure 5.4: Variation of directional and thermal velocities with respect to changes in the normalized distance from the target surface (including the impacts from pressure increment).

Based on the discussion so far, it appears that, equipment modification needs to be performed to upgrade the performance of the PED tool, to confirm:

1. Avoidance of contaminated target plasma, to ensure a better nucleation layer prior to thick epi growth. For this shutter door needs to be used between the target and the substrate.
2. Control the influence from the turbo molecular pump, as this will allow maintaining a desired amount of chamber pressure through feeding of smaller amount of gas, removing the chances of building up a very high pressure differential along the path of the plasma. To confirm this, a butterfly valve is required to be used in between the chamber and the turbo molecular pump.

3. To ensure better blending among the metal components in the plasma and atomic nitrogen species. Atomic nitrogen lifetime needs to be lengthened, apart from collision based recombination, or it needs to be highly populated using a nitrogen plasma source as used in other commercial processes to increase probability of reaction on the substrate. From experiments done in this research, lack of nitrogen atomic species results in metal rich or metal thin film on substrate (Section 4.4).

5.3 New buffer layers for III-nitride growth at lower temperature

In Section 4.3, it has been demonstrated that GaN thin films are grown on sapphire substrates (incorporating a 15 nm ZnO buffer layer) at 300^{o}C using the PED process. It appears that the ZnO buffer layer improved the structural properties of the GaN epilayer. Attempts were also taken in the course of this research to grow GaN on

engineered buffer layers grown on silicon using MBE methods. These are PbSe/BaF_2/CaF_2/Si(111) structures [54]. A benefit of using a buffer layer containing fluoride materials is that the epilayers grown on this structure can be flip-chip bonded to other substrates and can be detached from the parent substrate only soaking the sample in water dissolve the fluoride layers [59]. There is one obstacle in using this process to transfer any PED grown epilayer. The fluorides cannot be exposed to atmospheric environment as it will deteriorate the fluoride epitaxy, making it not usable for epi-transfer process. Thus, PbSe coated fluoride layers were used to grow GaN on top to study the capability of the PED system. Figure 5.5 shows the simulated structure of the attempted samples of GaN on fluoride coated silicon with a PbSe on top (to secure the fluorides from atmospheric impact). In the simulated structure a strained GaN(0002) layer is assumed before the relaxed layer deposition to compensate the mismatch between PbSe(111) and GaN(0002).

Several attempts were made to deposit GaN according to the structure presented in Figure 5.5. The PbSe/BaF_2/CaF_2/Si(111) structures were grown in a Veeco Gen II MBE at University of Oklahoma using published procedures reported in [60] [61] [62]. The grown samples were diced into 1cm x 1cm substrates as required by the PED substrate stage mount, and loaded in the chamber for overnight pumping to attain a base pressure of ~10^{-7} Torr. A growth procedure similar to that described in Section 4.3 was applied the next day, and two different growth temperatures were attempted: 300^o and 600^{o}C. Figure 5.6 shows the powder diffraction XRD scans of the samples grown according to the procedure mentioned. As it appears, mostly non-polar GaN is grown on the PbSe layers. Some Ga_2O_3 is grown too. Figure 5.6 (a) shows the XRD scan of GaN

growth at 300°C on PbSe/BaF_2/CaF_2/Si(111). In a similar PED growth run, another sample was used, Figure 5.6(b) (same growth temperature), but the buffer coated Si(111) was also W coated on the back. This was confirmed as a procedure that the PbSe buffer

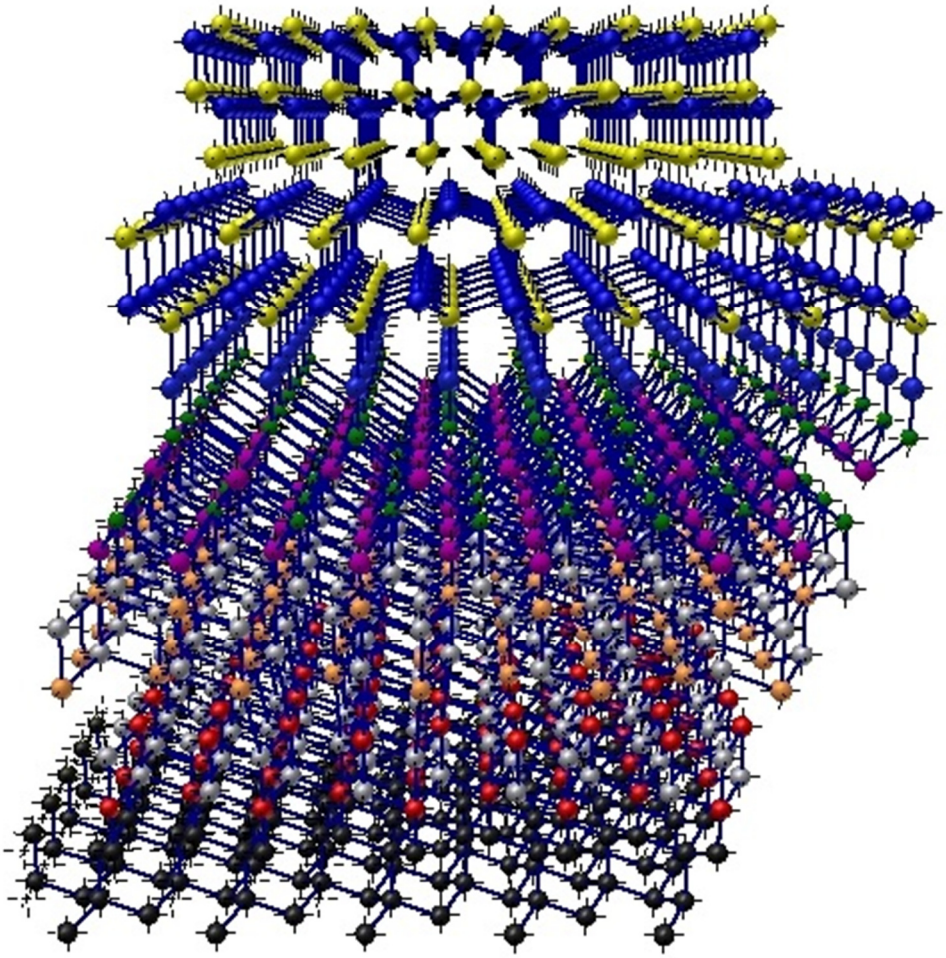

Figure 5.5: GaN/PbSe/BaF_2/CaF_2/Si(111) structure.

growth went through during MBE growth for uniform heat absorption at the substrate. It appeared that the sample with no W coating produced more profound signatures of non-polar GaN. Non-polar GaN is gaining interest in the solid state lighting industry as non-polar GaN is more defect free compared to the polar GaN [63] [64] [65] since defects during GaN growth propagate towards the polar <0002> direction. In addition, non-

polar GaN is desired for fabrication of efficient green LEDs since it does not suffer from the quantum confined Stark effect, which is known to reduce light emission efficiency in

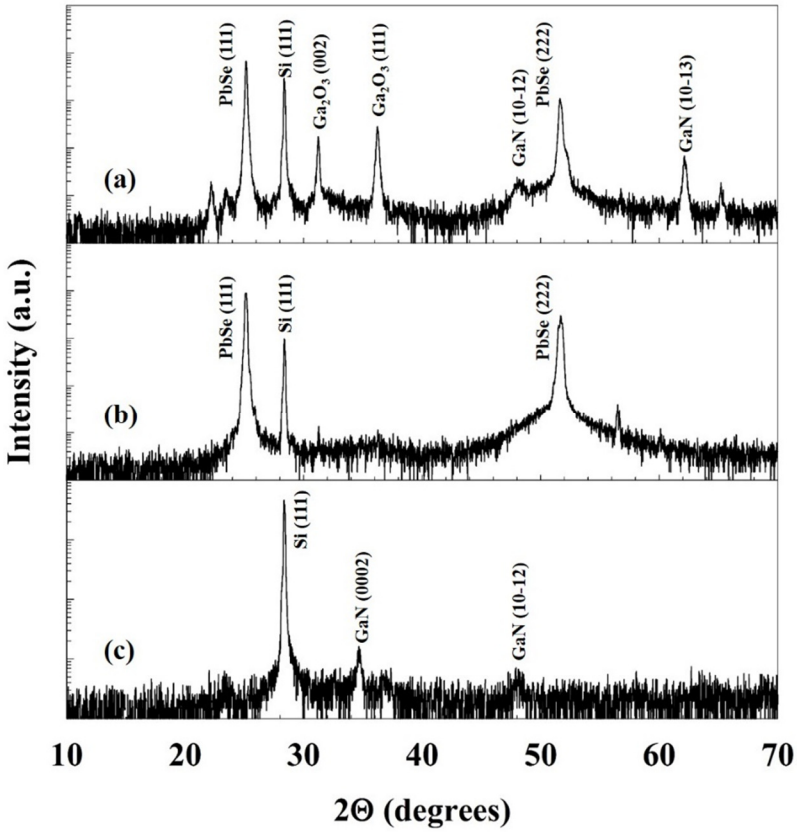

Figure 5.6: Powder XRD scan of GaN growth on (a) PbSe/BaF_2/CaF_2/Si(111) at 300°C, (b) PbSe/BaF_2/CaF_2/Si(111)/W at 300°C, and (c) PbSe/BaF_2/CaF_2/Si(111) at 600°C.

LEDs that have InGaN quantum wells. After the growth temperature was raised to 600°C, to avail the similar results as reported in Section 4.3, a combination of polar (0002) and non-polar (10-12) GaN was observed on Si(111). But the drawback of this temperature increment ultimately caused an obstacle in the primary objective of this study. The PbSe XRD peaks were not observed which stands that at increased substrate temperature the Se got disassociated from the PbSe structure and the PbSe epilayer was damaged which ultimately does not help in using the sample for flip-chip bonding.

Thus, the study with IV-VI material as a buffer layer on fluoride coated silicon demonstrates that PED is capable to grow low temperature GaN on the new kind of buffer layer coated Si(111) and further study can make the GaN epilayers improved in properties.

5.4 Continuation of previous research

Growth of GaN on thin ZnO (15 nm) coated sapphire at 300^{o}C has shown promise for the PED technique to produce low temperature GaN epilayers and buffer layers. Future research will be focused on similar growth approaches on Si(111) and Si(100) substrates with variation in growth temperature and other plasma parameters. The growth of AlN epilayers will also be studied to demonstrate the PED capability for ultra wide bandgap materials. For this ZnO buffer layers and GaN/ZnO buffer layers will be used on both sapphire and silicon substrates with growth temperature variations.

5.5 Summary

This dissertation had a primary objective of demonstration of pulsed electron beam deposition (PED) as a growth tool for binary wide bandgap materials (ZnO, GaN, AlN). With different research experiments it has thus been established that PED holds the capability to grow these materials at temperatures as low as 300^{o}C on cost-effective substrates, which is highly demanded by the solid state lighting and the electronics industries. In this chapter some future research objectives are suggested with some preliminary observations with a strong expectation that further research on this tool for wide bandgap material growth can increase its capability.

References

1. Nakamura, S., et al., *Superbright Green Ingan Single-Quantum-Well-Structure Light-Emitting-Diodes.* Japanese Journal of Applied Physics Part 2-Letters, 1995. **34**(10B): p. L1332-L1335.
2. Nakamura, S., T. Mukai, and M. Senoh, *Candela-class high-brightness InGaN/AlGaN double-heterostructure blue-light-emitting diodes.* Applied Physics Letters, 1994. **64**(13): p. 1687-1689.
3. Culbertson, L. *Wide Bandgap Semiconductors Go Beyond Silicon in Power, RF, LED Lighting, and Optoelectronics*. 2014 [cited 2014 Oct. 3, 2014]; Available from: http://www.mouser.com/applications/wide-bandgap-beyond-silicon/.
4. University of California, D., Chemwiki Project, *Intrinsic Semiconductors.*
5. contributors, W., *Monolithic microwave integrated circuit.* Wikipedia, The Free Encyclopedia, 2014.
6. Zinck, L.R.a.C., *RF filters, PAs, Antenna Switches & Tunability for Cellular Handsets.* Yole Developpment, 2012.
7. Round, H.J., *A note on carborundum.* Electrical world, 1907. **49**(6): p. 309.
8. Lehovec, K., C. Accardo, and E. Jamgochian, *Injected light emission of silicon carbide crystals.* Physical Review, 1951. **83**(3): p. 603.
9. Semiconductor, C., *Global LED Market to Reach $42.7 Billion by 2020.* 2014.
10. Sobanska, M., et al., *Plasma-assisted MBE growth of GaN on Si(111) substrates.* Crystal Research and Technology, 2012. **47**(3): p. 307-312.
11. Aidam, R., et al., *Strain control of AlGaN/GaN high electron mobility transistor structures on silicon (111) by plasma assisted molecular beam epitaxy.* Journal of Applied Physics, 2012. **111**(11).
12. Chiba, Y., T. Araki, and Y. Nanishi, *ECR-MBE growth of GaN using hydrogen-nitrogen mixed gas plasma.* Ieice Transactions on Electronics, 2000. **E83c**(4): p. 627-632.
13. Zhang, X.G., et al., *Investigation of MOCVD growth parameters on the quality of GaN epitaxial layers.* Journal of Crystal Growth, 2011. **318**(1): p. 436-440.
14. Ishikawa, H., et al., *Improved MOCVD growth of GaN on Si-on-porous-silicon substrates.* physica status solidi (c), 2010. **7**(7-8): p. 2049-2051.
15. Kobayashi, A., et al., *Room temperature epitaxial growth of AlGaN on ZnO by pulsed laser deposition.* Applied Physics Letters, 2006. **89**(11).
16. Ueno, K., et al., *Growth temperature dependence of structural properties of AlN films on ZnO (000(1)over-bar) substrates.* Applied Physics Letters, 2007. **90**(14).
17. Sakurada, K., et al., *Low temperature epitaxial growth of GaN films on LiGaO2 substrates.* Applied Physics Letters, 2007. **90**(21).
18. Porter, H.L., et al., *Growth of ZnO films on C-plane (0001) sapphire by pulsed electron deposition (PED).* Materials Science and Engineering B-Solid State Materials for Advanced Technology, 2005. **119**(2): p. 210-212.
19. Paine, D. and J. Bravman, *Laser ablation for materials synthesis.* 1990.
20. LLC, N., *User Manual for PEBS-21 System.* User Manual for PEBS-21 System.

21. Muller, G. and C. Schultheiss. *Deposition by means of pulsed electron beam ablation*. in *High-Power Particle Beams, 1994 10th International Conference on*. 1994. IET.
22. Strikovski, M. and K. Harshavardhan, *Parameters that control pulsed electron beam ablation of materials and film deposition processes.* Applied physics letters, 2003. **82**(6): p. 853-855.
23. Ohta, J., et al., *Growth of group III nitride films by pulsed electron beam deposition.* Journal of Solid State Chemistry, 2009. **182**(5): p. 1241-1244.
24. Lee, S.R., et al., *Effect of threading dislocations on the Bragg peakwidths of GaN, AlGaN, and AlN heterolayers.* Applied Physics Letters, 2005. **86**(24).
25. Tricot, S., et al., *Epitaxial ZnO thin films grown by pulsed electron beam deposition.* Surface Science, 2010. **604**(21-22): p. 2024-2030.
26. Williams, D.S., et al., *Nitrogen, Oxygen, and Argon Incorporation during Reactive Sputter Deposition of Titanium Nitride.* Journal of Vacuum Science & Technology B, 1987. **5**(6): p. 1723-1729.
27. Özgür, Ü., et al., *A comprehensive review of ZnO materials and devices.* Journal of Applied Physics, 2005. **98**(4): p. -.
28. Look, D.C., et al., *Electrical properties of bulk ZnO.* Solid State Communications, 1998. **105**(6): p. 399-401.
29. Wang, X. and A. Yoshikawa, *Molecular beam epitaxy growth of GaN, AlN and InN.* Progress in Crystal Growth and Characterization of Materials, 2004. **48–49**(0): p. 42-103.
30. Kawai, Y., et al. *Thick InGaN growth on several crystal planes of ZnO substrate by metalorganic vapor phase epitaxy*. in *Integrated Optoelectronic Devices 2008*. 2008. International Society for Optics and Photonics.
31. Watanabe, A., et al., *The growth of single crystalline GaN on a Si substrate using AIN as an intermediate layer.* Journal of crystal growth, 1993. **128**(1): p. 391-396.
32. Takeuchi, T., et al., *Growth of single crystalline GaN film on Si substrate using 3C-SiC as an intermediate layer.* Journal of crystal growth, 1991. **115**(1): p. 634-638.
33. Bläsing, J., et al., *The origin of stress reduction by low-temperature AlN interlayers.* Applied physics letters, 2002. **81**(15): p. 2722-2724.
34. Gong, J.-R., M.-F. Yeh, and C.-L. Wang, *Growth and characterization of GaN and AlN films on (111) and (001) Si substrates.* Journal of crystal growth, 2003. **247**(3): p. 261-268.
35. Arslan, E., et al., *Buffer optimization for crack-free GaN epitaxial layers grown on Si (1 1 1) substrate by MOCVD.* Journal of Physics D: Applied Physics, 2008. **41**(15): p. 155317.
36. Xiu, F., et al., *ZnO growth on Si with low-temperature ZnO buffer layers by ECR-assisted MBE.* Journal of crystal growth, 2006. **286**(1): p. 61-65.
37. Kramida, A., Ralchenko, Yu., Reader, J., and NIST ASD Team (2014), *NIST Atomic Spectra Database (ver. 5.2).* 2014.
38. Saji, K.J., N.V. Joshy, and M.K. Jayaraj, *Optical emission spectroscopic studies on laser ablated zinc oxide plasma.* Journal of Applied Physics, 2006. **100**(4): p. -.

39. Silie, F., et al., *Optical emission spectroscopy of electron cyclotron resonance-plasma enchanced metalorganic chemical vapor deposition process for deposition of GaN film.* Plasma Science and Technology, 2008. **10**(1): p. 70.
40. Laboratory, S.R.N.M., *Zeiss NEON High Resolution Scanning Electron Microscope.* 2014.
41. Cullity, B.D. and S.R. Stock, *Elements of X-ray Diffraction*. 2001: Pearson.
42. Castaneda-Lopez, H., *Deposition Temperature dependence of ZnO/Si Grown by Pulsed Laser Deposition.* 2004.
43. Omichi, K., et al., *AP-HVPE growth of ZnO with room-temperature ultraviolet emission.* J. Mater. Chem., 2001. **11**(12): p. 3158-3160.
44. Bang, K.-H., et al., *Effects of growth temperature on the properties of ZnO/GaAs prepared by metalorganic chemical vapor deposition.* Journal of Crystal Growth, 2003. **250**(3–4): p. 437-443.
45. Guziewicz, E., et al., *ALD grown zinc oxide with controllable electrical properties.* Semiconductor Science and Technology, 2012. **27**(7): p. 074011.
46. KIKUCHI, S., *Diffraction of cathode rays by mica.* Proceedings of the Imperial Academy, 1928. **4**(6): p. 271-274.
47. Stojakovic, D., *Electron backscatter diffraction in materials characterization.* Processing and Application of Ceramics, 2012. **6**(1): p. 1-13.
48. Thool, G.S., et al., *Facile synthesis of flat crystal ZnO thin films by solution growth method: A micro-structural investigation.* Journal of Saudi Chemical Society, 2014. **18**(5): p. 712-721.
49. Gurav, K.V., et al., *Controlled crystallite orientation in ZnO nanorods prepared by chemical bath deposition: Effect of H2O2.* Journal of Alloys and Compounds, 2011. **509**(29): p. 7723-7728.
50. Djurišić, A.B., et al., *Photoluminescence and Electron Paramagnetic Resonance of ZnO Tetrapod Structures.* Advanced Functional Materials, 2004. **14**(9): p. 856-864.
51. Zhang, X., et al., *Effect of aspect ratio and surface defects on the photocatalytic activity of ZnO nanorods.* Sci. Rep., 2014. **4**.
52. Vispute, R., et al., *Growth of epitaxial GaN films by pulsed laser deposition.* Applied physics letters, 1997. **71**(1): p. 102-104.
53. Ishizaka, A. and Y. Shiraki, *Low temperature surface cleaning of silicon and its application to silicon MBE.* Journal of the Electrochemical Society, 1986. **133**(4): p. 666-671.
54. McCann, P.J., et al., *MBE growth of PbSe/CaF2/Si(1 1 1) heterostructures.* Journal of Crystal Growth, 1997. **175–176, Part 2**(0): p. 1057-1062.
55. Liu, W., X. Fang, and P. McCann, *Reflection high-energy electron diffraction study of the molecular beam epitaxial growth of CaF2 on Si (110).* Applied physics letters, 1995. **67**(12): p. 1695-1697.
56. Kim, H. and H. Kwok, *Correlation between target-substrate distance and oxygen pressure in pulsed laser deposition of YBa2Cu3O7.* Applied physics letters, 1992. **61**(18): p. 2234-2236.
57. Kwok, H., et al., *Correlation between plasma dynamics and thin film properties in pulsed laser deposition.* Applied surface science, 1997. **109**: p. 595-600.

58. Strikovski, M.D., J. Kim, and S.H. Kolagani, *Plasma energetics in pulsed laser and pulsed electron deposition*, in *Springer Handbook of Crystal Growth*. 2010, Springer. p. 1193-1211.
59. McCann, P.J., *Method for thin film thermoelectric module fabrication*. 2012, Google Patents.
60. Wu, H.Z., et al., *Transfer of PbSe/PbEuSe epilayers grown by MBE on BaF2-coated Si(111).* Thin Solid Films, 1999. **352**(1–2): p. 278-282.
61. Wu, H., et al., *Molecular beam epitaxy growth of PbSe on BaF 2-coated Si (111) and observation of the PbSe growth interface.* Journal of Vacuum Science & Technology B: Microelectronics and Nanometer Structures, 1999. **17**(3): p. 1263-1266.
62. Fang, X., et al., *Molecular beam epitaxy of periodic BaF2/PbEuSe layers on Si (111).* Journal of Vacuum Science & Technology B, 1999. **17**(3): p. 1297-1300.
63. Haskell, B.A., et al., *Microstructure and enhanced morphology of planar nonpolar m-plane GaN grown by hydride vapor phase epitaxy.* Journal of electronic materials, 2005. **34**(4): p. 357-360.
64. Schmidt, M.C., et al., *Demonstration of nonpolar m-plane InGaN/GaN laser diodes.* Japanese journal of applied physics, 2007. **46**(3L): p. L190.
65. Haskell, B., et al., *Defect reduction in (112¯ 0) a-plane gallium nitride via lateral epitaxial overgrowth by hydride vapor-phase epitaxy.* Applied physics letters, 2003. **83**(4): p. 644-646.

Appendix A: PED System Drawings

This appendix contains the Solid Works drawings of the customized chamber, chamber door, view port flange, and nipple for the placement of the whole chamber on the stage. The vendor was MDC Vacuum, CA.

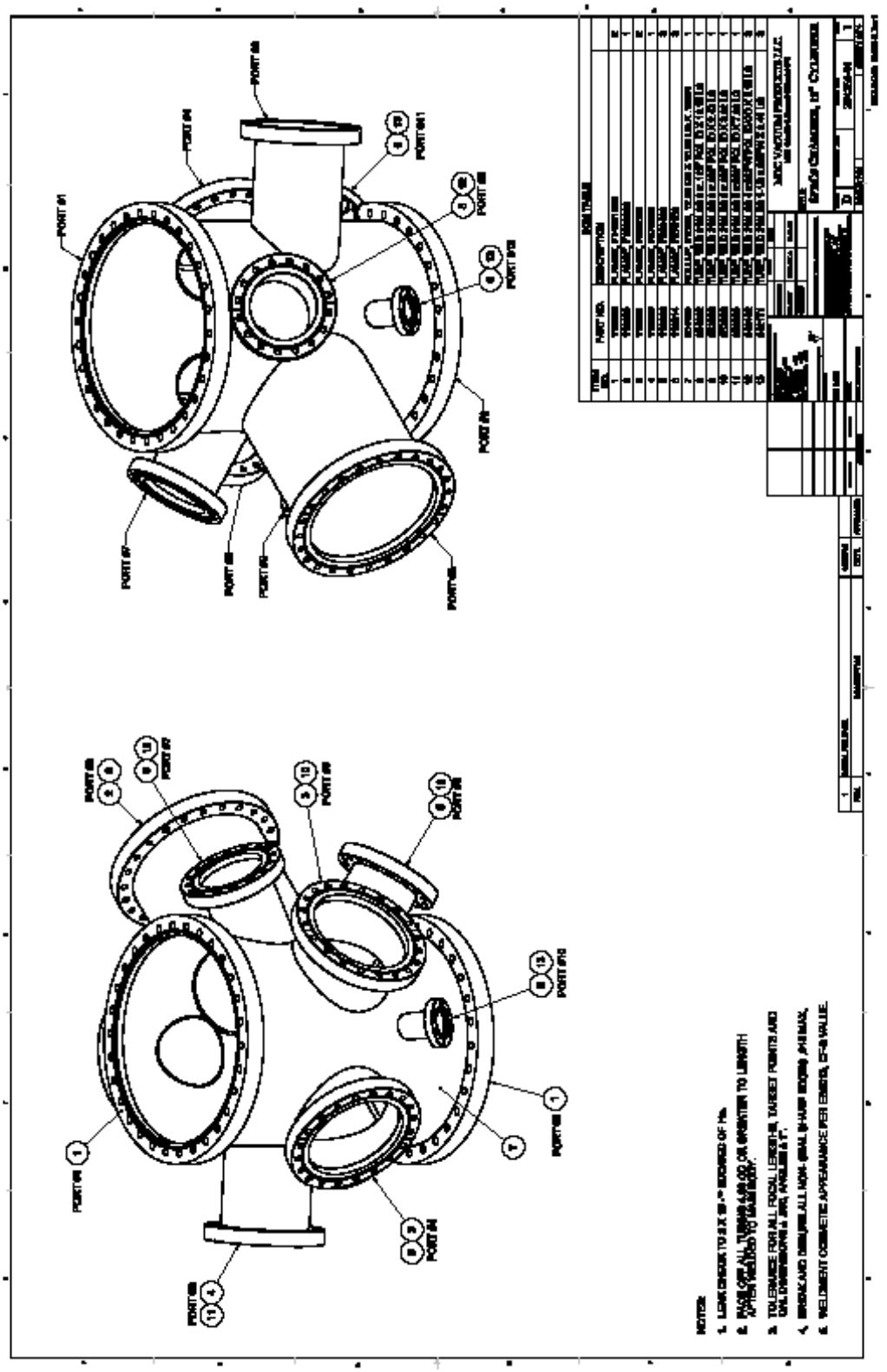

Chamber (Sheet 1)

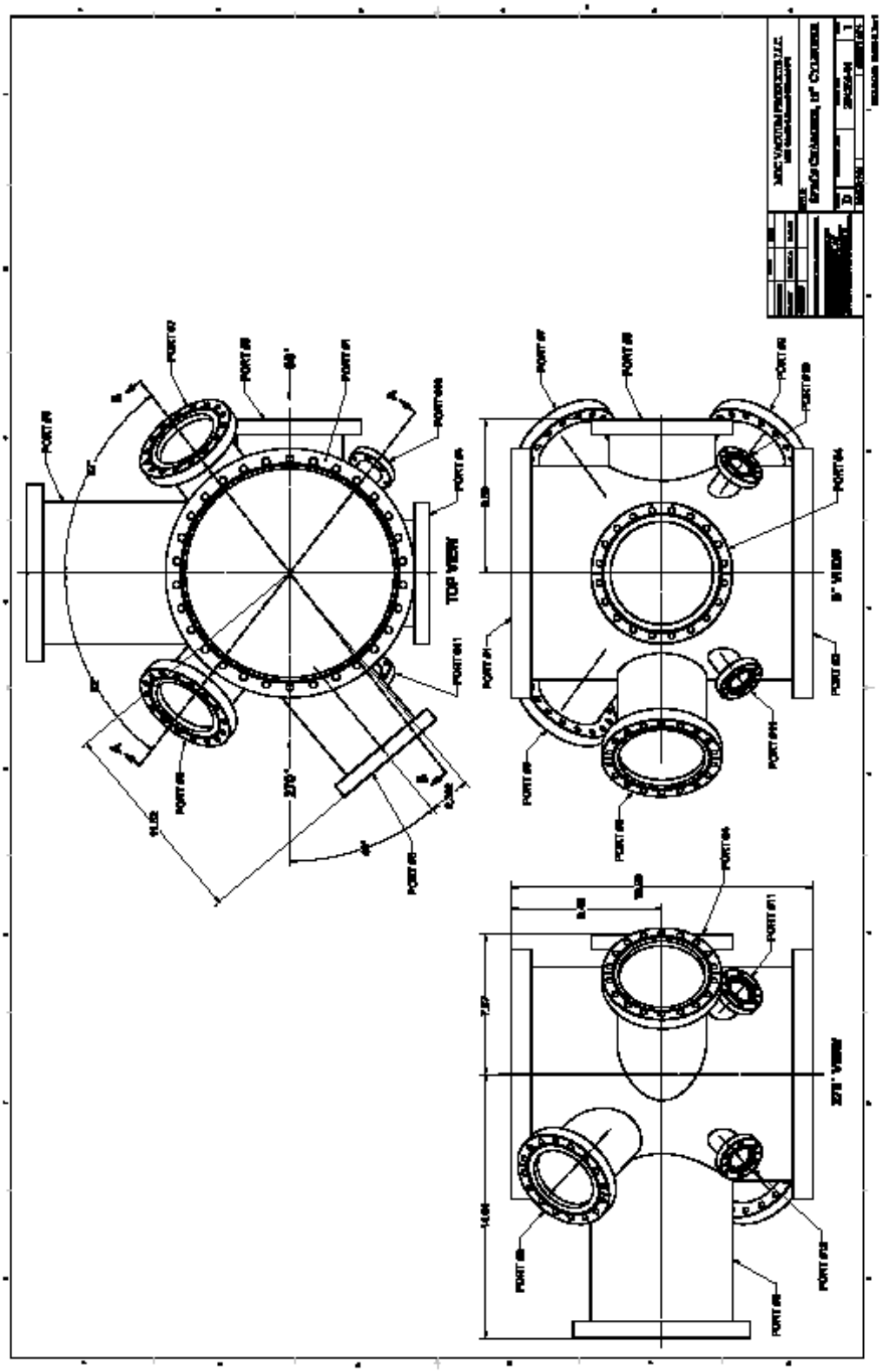

(Chamber Sheet 2)

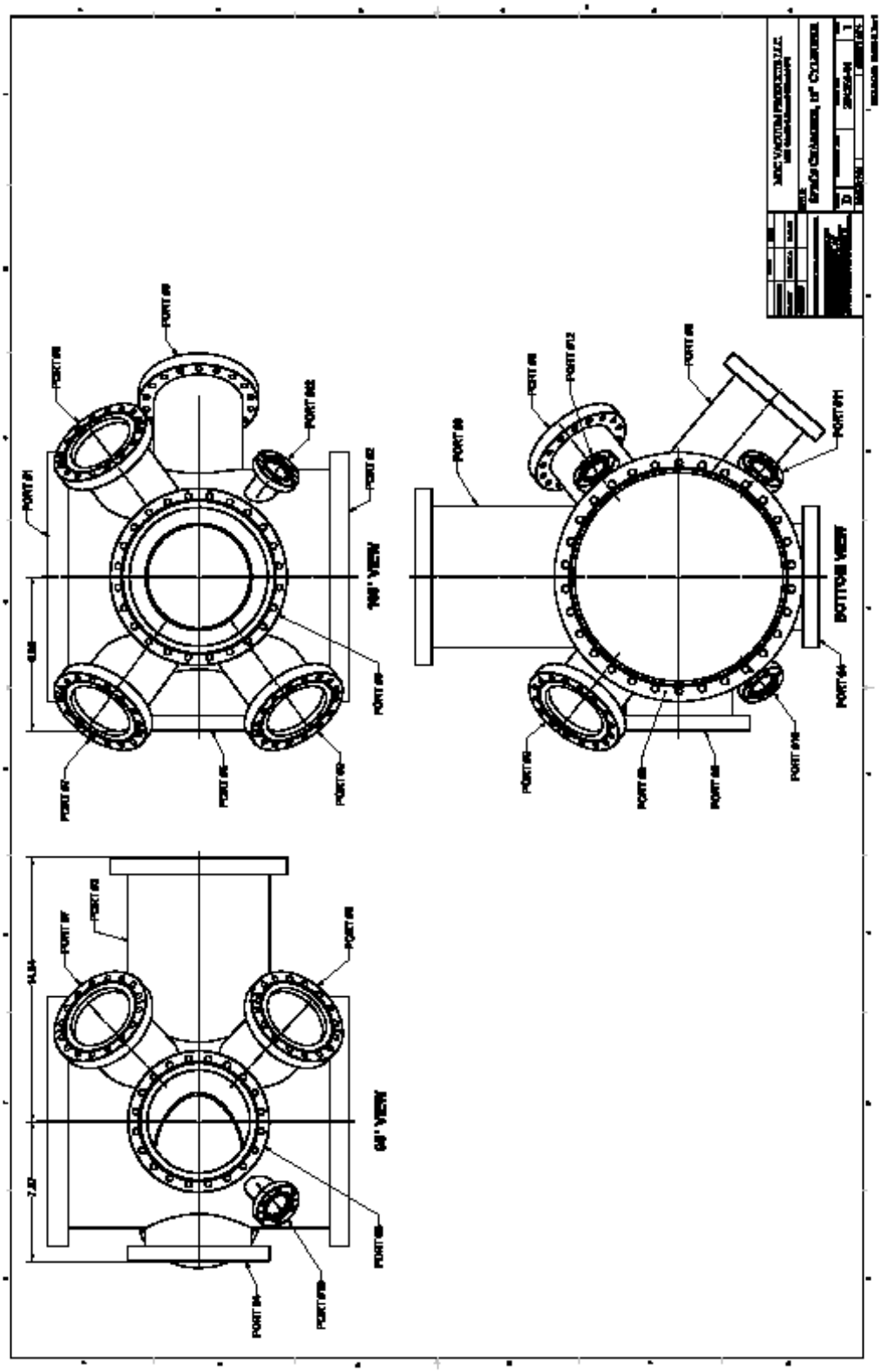

(Chamber Sheet 3)

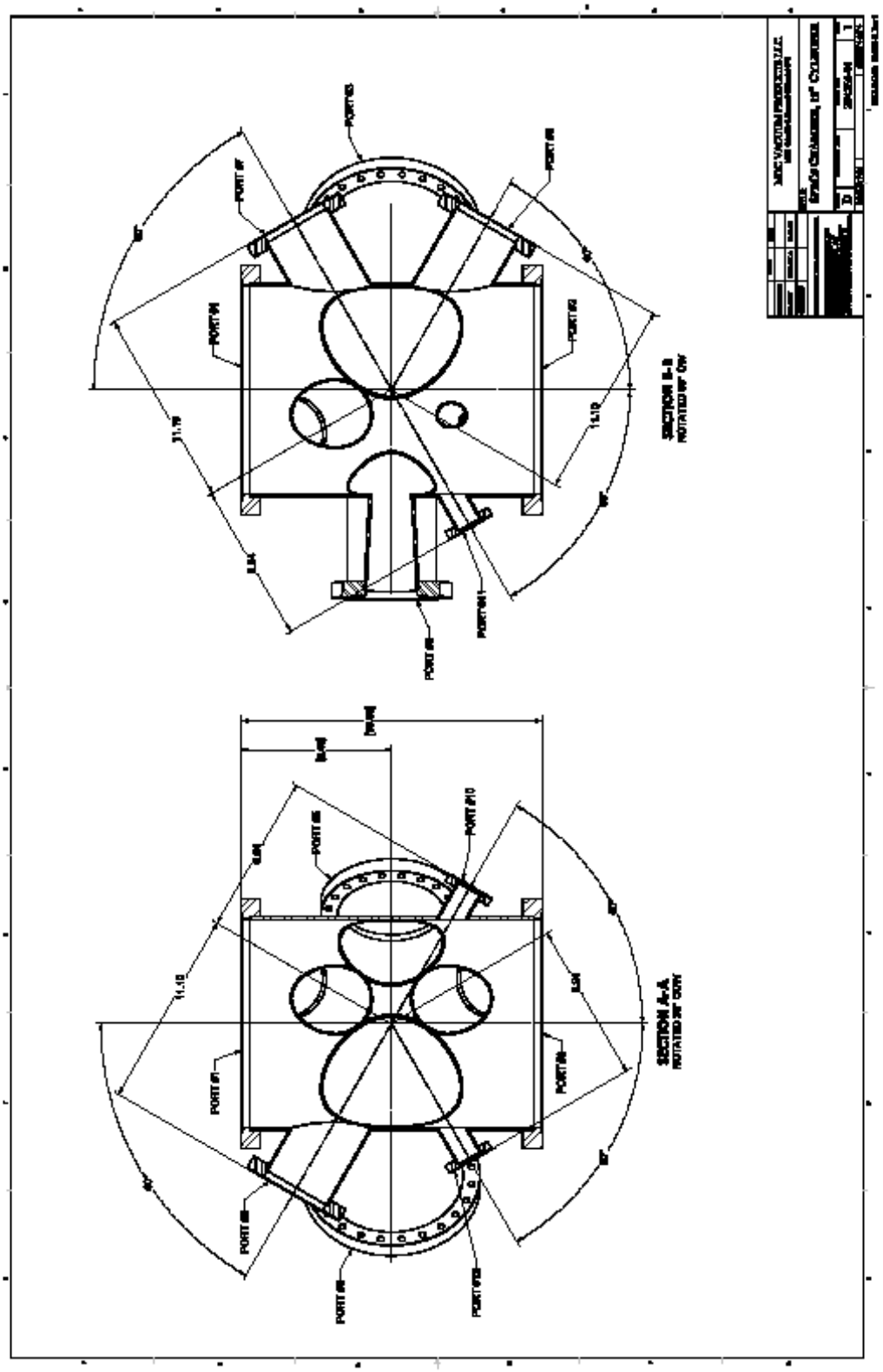

(Chamber Sheet 4)

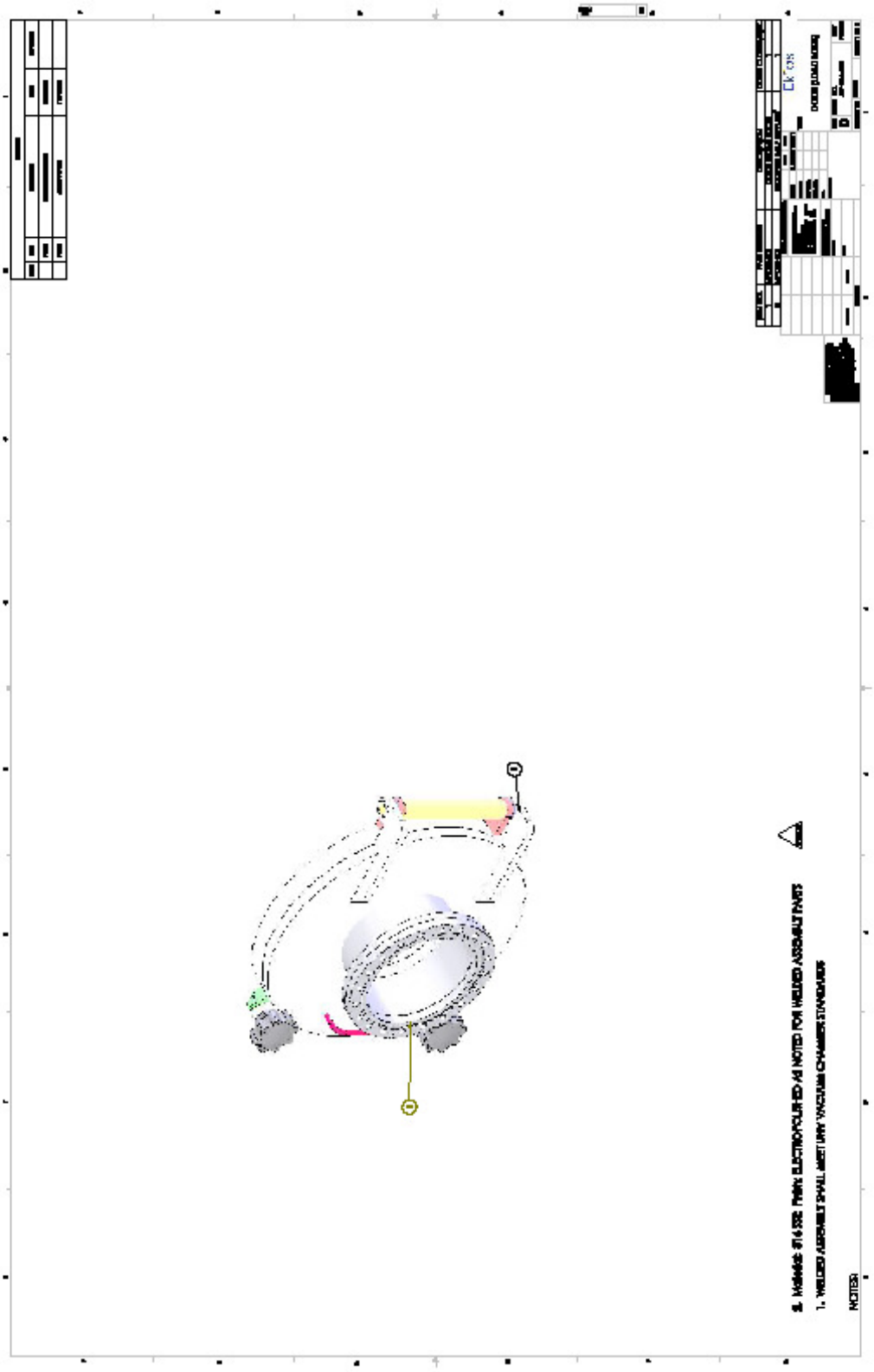

(Chamber Door Sheet 1)

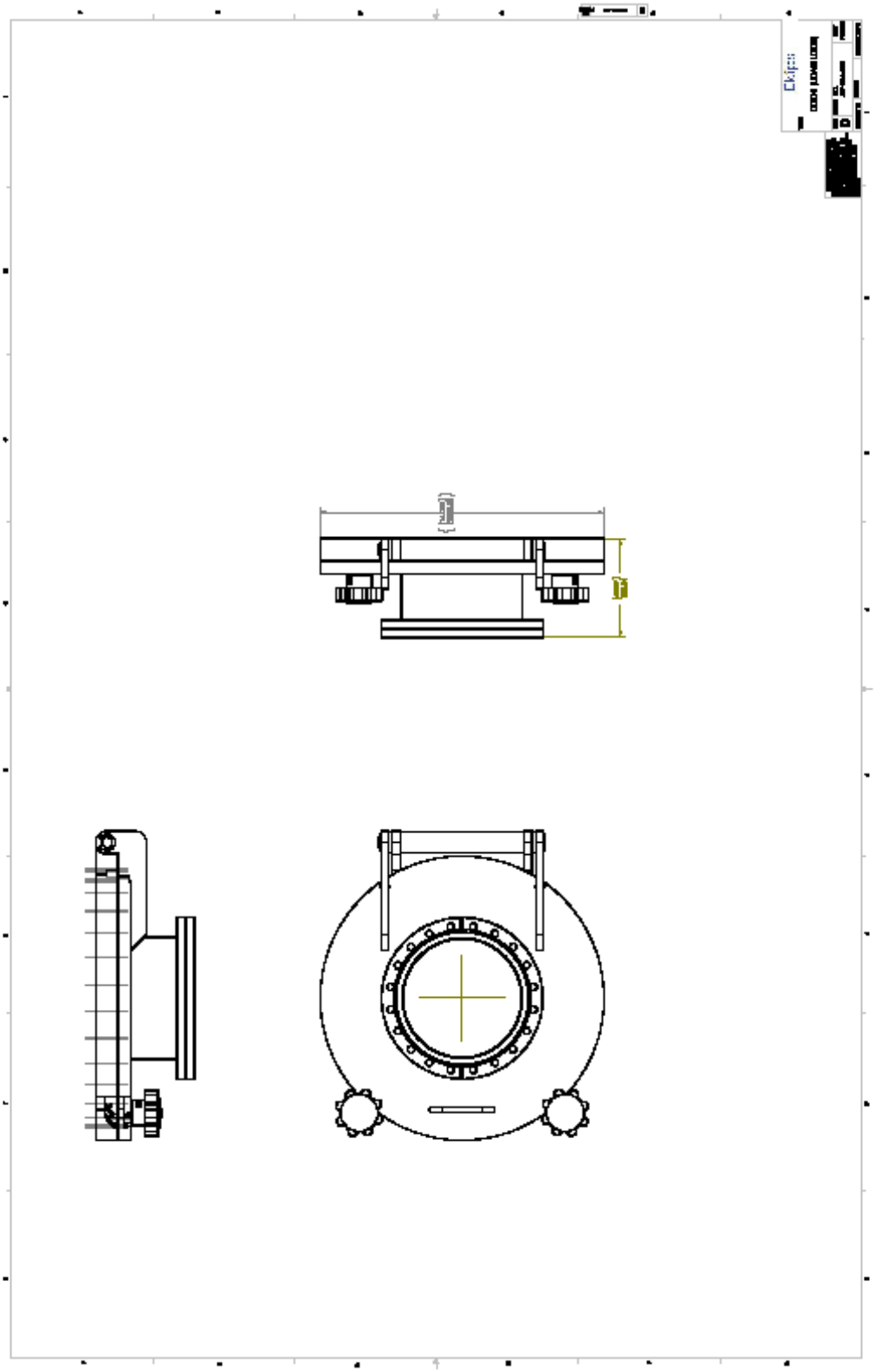

(Chamber Door Sheet 2)

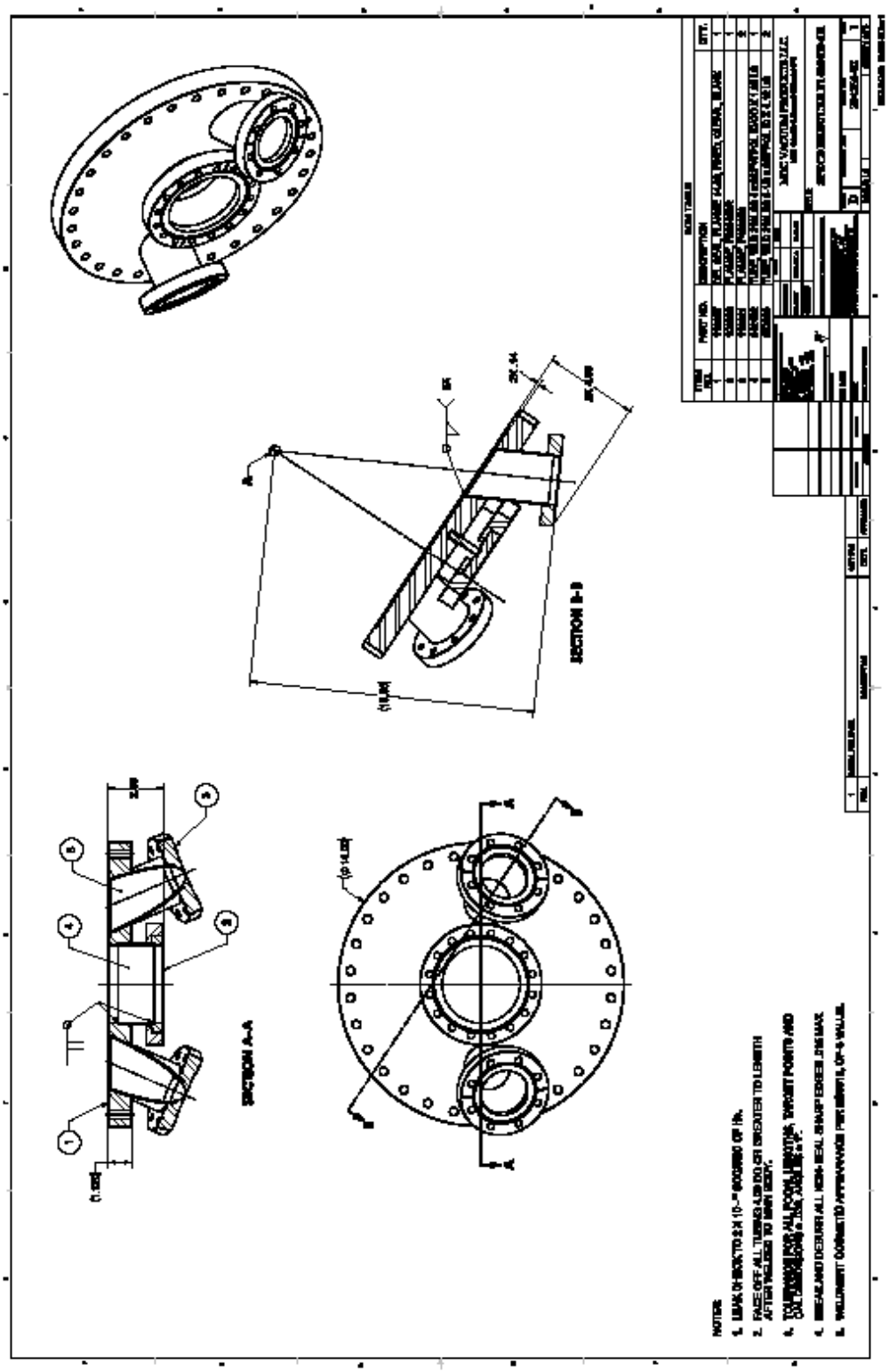

(Chamber Viewport Flange Sheet 1)

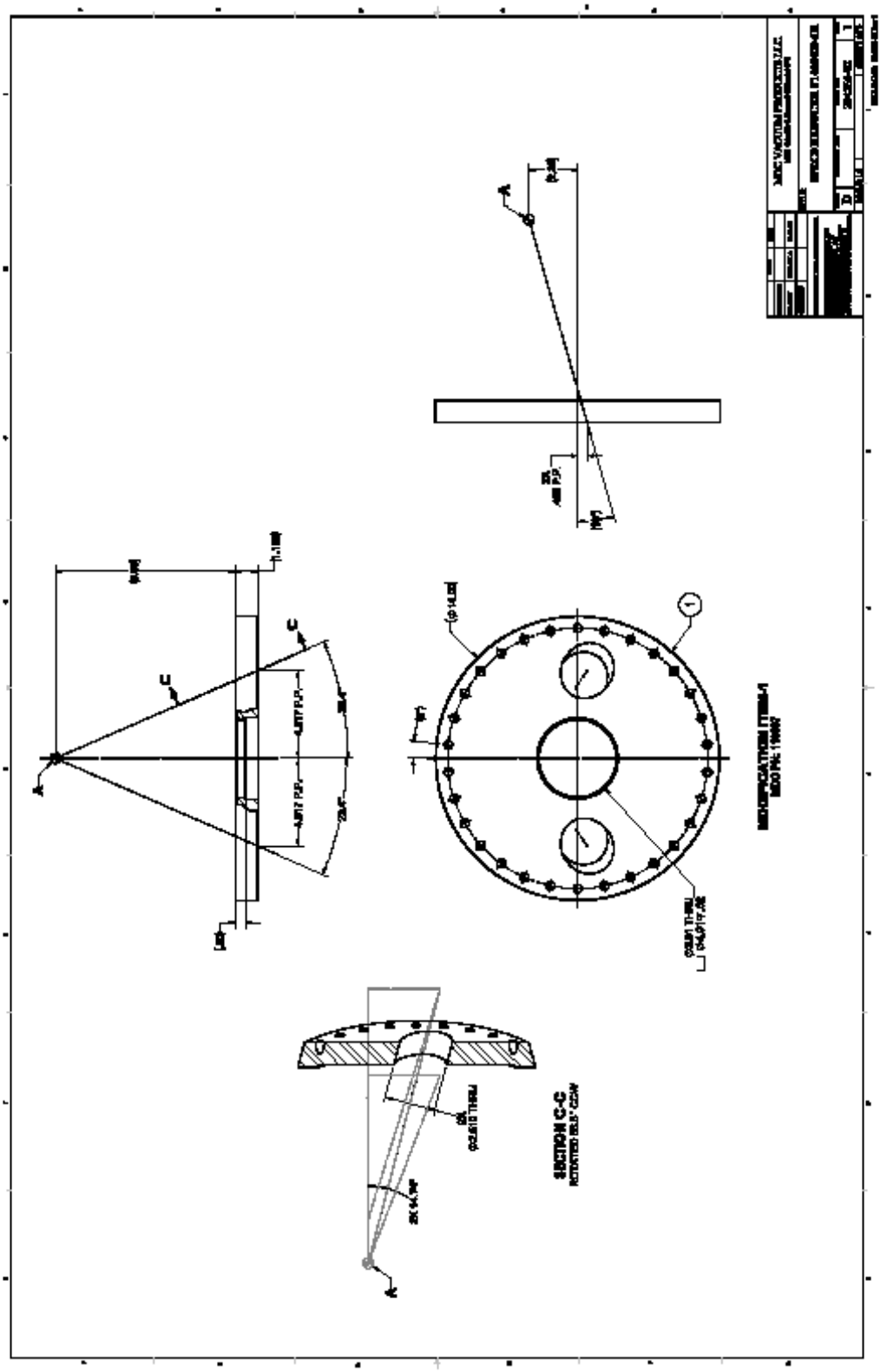

(Chamber Viewport Flange Sheet 2)

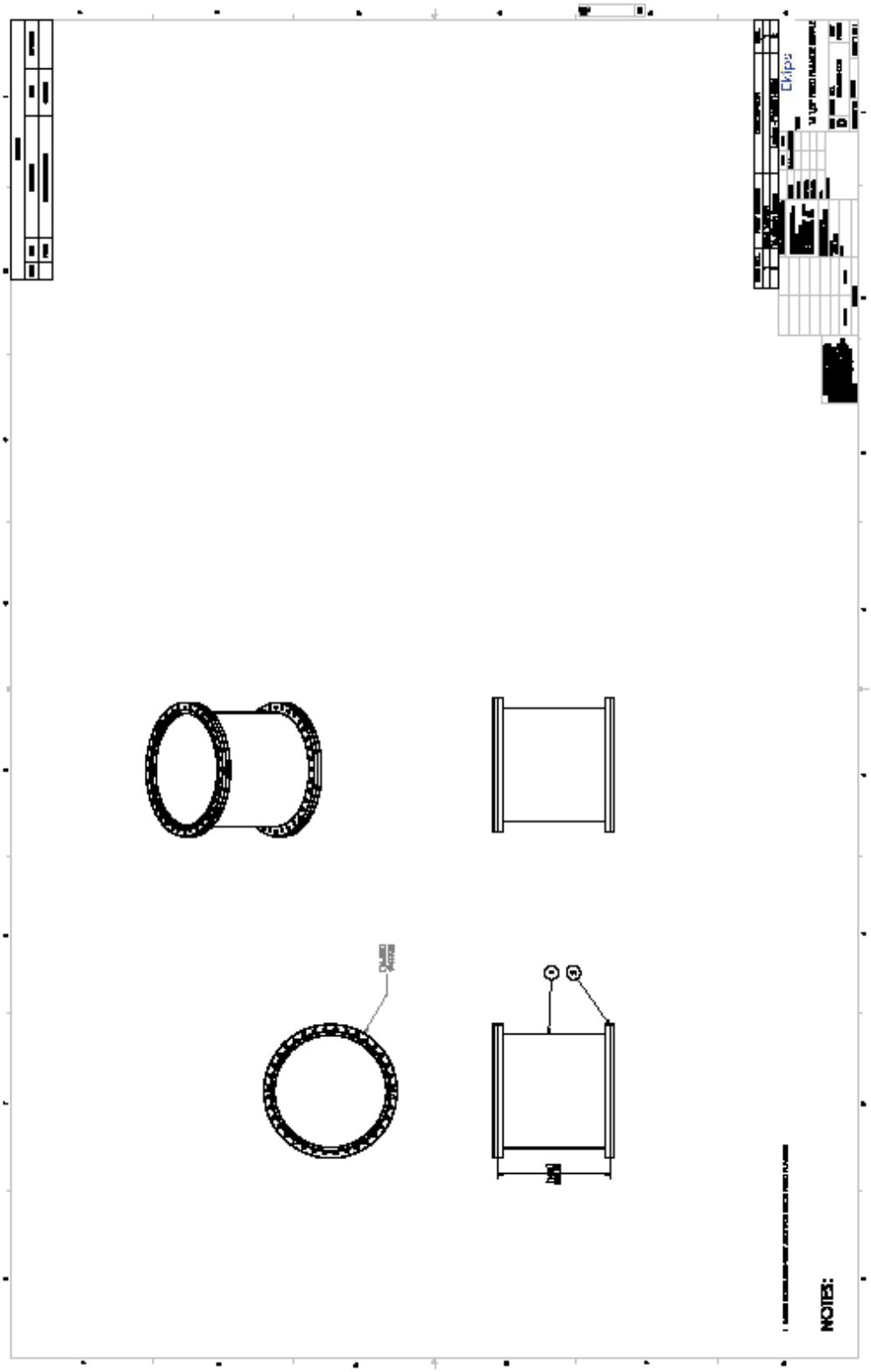

(Chamber Mount Nipple)

Appendix B: Growth Specifications

A total number of 74 experiments (depositions) were performed using the PED system during this research work. The system being the first of its custom design, different parameters were studied using wide range of values to estimate an appropriate recipe for the materials of interest. Such as, the substrate temperature, pulse rate, electron pulse voltage, chamber pressure, background gas have been studied to fix suitable growth parameters. Although this effort involved a great amount of time and dedication, but to characterize fabrication equipment such trial error operation is very useful to experience the impacts from different parameter variations.

Of the total 74 growth runs, specifications will be provides in this appendix on the last 29 experiments (from 46 to 74). The first 45 experiments have been performed to study the quality of films varying different process parameters. As example, during the first 20 growths, 10Hz pulse rate was used, which ultimately caused metal rich film deposition, as too much plasma particle generation resulted in light-weight N and O recombination leaving behind the heavier metal plasma components active in the plasma plume. This helped to estimate a lower pulse rate (1, 3, and 5Hz) for III-nitride and ZnO deposition process for future successful experiments. The use of different pulse voltages were also explored for the materials. As it appeared, maximum pulse energy with high pulse rate does not ensure better plasma, rather using a wisely chosen combination of pulse energy and pulse rate comprises a suitable parameter set for plume generation. It was found that 15KV pulse voltage is good for III-nitrides, while for ZnO 11-12KV pulse energies are more appropriate. Use of a background gas pressure was also studied which helped to find the “safe zone” of operation for the e-gun confirming

better plasma plume. So, different background gas pressures were studied to analyze the impacts on the gun operation and simultaneously on the deposited film quality.

Plasma was studied using the emission spectroscopy method identifying the plasma components in the plume. The NIST database has been used to identify the components. It was found that the emission spectroscopy requires a calibration as the peaks were 0.6nm left-shifted as it appears in the spectra. Multiple evidences were justified to confirm this claim. In addition, the substrate mount used in the first 40 experiments was a Ni-Cr platen with no customization done on it. However, after the first 40 experiments were performed, the customized platen (used in the later experiments) was introduced to expose the back of the substrates for better heating purpose. The following presents the growth parameter specification used in experiments 45 through 74.

P046

Substrate Batch #	Sample(s)/Block	Grower(s)	Dates
2" Sapphire Wafer, Lot. No: 238Z006, Cassette No: 01M4159	2 x 1cm^2 coupons	Arefin	11/05/13
3" Si(111) wafer	2 x 1cm^2 coupons	Arefin	11/05/13

Ex-situ Cleaning	Date	Comments
Running DI water, Acetone US, Methanol US, UHP N_2 Purge	11/04/2013	

Base Pressure (Torr)	Working Pressure (Torr)	Gun tip-to-Gas Tip (mm)	Tip-to-Target (mm)	Sub-to-Target (mm)	Target Rotation Speed (rpm)/Rot. Direction	Sub. Temp. (^{o}C)	Sub. Rotation Speed (rpm)
6.57x10^{-7}	20x10^{-3}	15	2~3 (1.380" HT)	50	~60/CCW	500	~20/CCW

e-gun Voltage	Repetition Rate	Number of Pulses	MFC (read, sccm)	Needle valve (read)
15 KV	1 Hz	3600	(2600, 203)	343

Comments:

1. Raised SS temperature to 924^{o}C and chamber pressure increased to 2.53 x 10^{-5} Torr (for out gassing). Waited for 30 minutes before pressure went stable at 2 x 10^{-5} Torr.

P047

Substrate Batch #	Sample(s)/Block	Grower(s)	Dates
2" Sapphire Wafer, Lot. No: 238Z006, Cassette No: 01M4159	2 x 1cm^2 coupons	Arefin	11/06/13
3" Si(111) wafer	2 x 1cm^2 coupons	Arefin	11/06/13

Ex-situ Cleaning	Date	Comments
Running DI water, Acetone US, Methanol US, UHP N_2 Purge	11/05/2013	

Base Pressure (Torr)	Working Pressure (Torr)	Gun tip-to-Gas Tip (mm)	Tip-to-Target (mm)	Sub-to-Target (mm)	Target Rotation Speed (rpm)/Rot. Direction	Sub. Temp. (^{o}C)	Sub. Rotation Speed (rpm)
$1.05x10^{-6}$	$20x10^{-3}$	15	2~3 (1.380" HT)	50	~60/CCW	550	~20/CCW

e-gun Voltage	Repetition Rate	Number of Pulses	MFC (read, sccm)	Needle valve (read)
15 KV	1 Hz	3600	(2600, 203)	343

P048

Substrate Batch #	Sample(s)/Block	Grower(s)	Dates
2" Sapphire Wafer, Lot. No: 238Z006, Cassette No: 01M4159	2 x 1cm^2 coupons	Arefin	11/07/13
3" Si(111) wafer	2 x 1cm^2 coupons	Arefin	11/07/13

Ex-situ Cleaning	Date	Comments
Running DI water, Acetone US, Methanol US, UHP N_2 Purge	11/06/2013	

Base Pressure (Torr)	Working Pressure (Torr)	Gun tip-to-Gas Tip (mm)	Tip-to-Target (mm)	Sub-to-Target (mm)	Target Rotation Speed (rpm)/Rot. Direction	Sub. Temp. (^{o}C)	Sub. Rotation Speed (rpm)
$1.06x10^{-6}$	$20x10^{-3}$	15	2~3 (1.380" HT)	50	~60/CCW	500	~20/CCW

e-gun Voltage	Repetition Rate	Number of Pulses	MFC (read, sccm)	Needle valve (read)
15 KV	1 Hz	1000 (AlN) & 3600 (GaN)	(2600, 203)	343

Comments:

1. First 1000 pulses of AlN was deposited followed by 3600 pulses of GaN.
2. Raised SS temperature to 930^{o}C and chamber pressure increased to 7.53×10^{-5} Torr (for out gassing). Waited for 30 minutes before pressure went stable at 8.61×10^{-6} Torr.
3. In the end, the chamber pressure had to go up to 22mTorr to ensure continuous gun operation (as missing pulses issues showed up).

P049

Substrate Batch #	Sample(s)/Block	Grower(s)	Dates
2" Sapphire Wafer, Lot. No: 238Z006, Cassette No: 01M4159	2 x 1cm^2 coupons	Arefin	11/12/13
3" Si(111) wafer	2 x 1cm^2 coupons	Arefin	11/12/13

Ex-situ Cleaning	Date	Comments
Running DI water, Acetone US, Methanol US, UHP N_2 Purge	11/11/2013	

Base Pressure (Torr)	Working Pressure (Torr)	Gun tip-to-Gas Tip (mm)	Tip-to-Target (mm)	Sub-to-Target (mm)	Target Rotation Speed (rpm)/Rot. Direction	Sub. Temp. (^{o}C)	Sub. Rotation Speed (rpm)
$4.25x10^{-6}$	$20x10^{-3}$	15	2~3 (1.380" HT)	50	~60/CCW	500	~20/CCW

e-gun Voltage	Repetition Rate	Number of Pulses	MFC (read, sccm)	Needle valve (read)
15 KV	1 Hz	1000(AlN), 7200(GaN)	(2600, 203)	343

Comments:

1. Raised SS temperature to 930^{o}C and chamber pressure increased to 3.25 x 10^{-6} Torr (for out gassing). Waited for 30 minutes before pressure went stable at 2 x 10^{-6} Torr.
2. Pressure in chamber had to go up to 21mTorr to have stable gun operation.

P050

Substrate Batch #	Sample(s)/Block	Grower(s)	Dates
	(i) 1 x 1cm^2 coupon [Sapphire] (ii) 1 x 1cm^2 coupon [Si(111)] (iii) 1 x 1cm^2 coupon of M116	Arefin	11/13/13

Ex-situ Cleaning	Date	Comments
Running DI water, Acetone US, Methanol US, UHP N_2 Purge (Sapphire and Silicon), M116 was only N_2 purged	11/12/2013	(i) Dip in 25% HF solution for 2 minutes (ii) Dip in 25% HF solution for 30 sec

Base Pressure (Torr)	Working Pressure (Torr)	Gun tip-to-Gas Tip (mm)	Tip-to-Target (mm)	Sub-to-Target (mm)	Target Rotation Speed (rpm)/Rot. Direction	Sub. Temp. (^{o}C)	Sub. Rotation Speed (rpm)
10^{-6}	$20x10^{-3}$	15	3 (1.380" HT)	50	~60/CCW	750	~20/CCW

e-gun Voltage	Repetition Rate	Number of Pulses	MFC (read, sccm)	Needle valve(mTorr)
15 KV	1Hz	1000 (AlN) and 7200(GaN)	190 sccm	N/A

Comments:

1. Raised SS bulb temperature to 1200^{o}C. Waited for 30 minutes before pressure went stable, after outgassing occurred and raised to $4.25x10^{-5}$Torr, initially.
2. 7200 pulses of GaN were fired at 1Hz with an increased pressure of 22mTorr.

P051

Substrate Batch #	Sample(s)/Block	Grower(s)	Dates
	(i) 1 x 1cm^2 coupon [Sapphire] (ii) 1 x 1cm^2 coupon [Si(111)] (iii) 1 x 1cm^2 coupon of M116	Arefin	11/19/13

Ex-situ Cleaning	Date	Comments
Running DI water, Acetone US, Methanol US, UHP N_2 Purge (Sapphire and Silicon), M116 was only N_2 purged	11/18/2013	(i) Dip in 25% HF solution for 2 minutes (ii) Dip in 25% HF solution for 30 sec

Base Pressure (Torr)	Working Pressure (Torr)	Gun tip-to-Gas Tip (mm)	Tip-to-Target (mm)	Sub-to-Target (mm)	Target Rotation Speed (rpm)/Rot. Direction	Sub. Temp. (^{o}C)	Sub. Rotation Speed (rpm)
$6.15x10^{-7}$	$24x10^{-3}$	15	3 (1.380" HT)	50	~60/CCW	750	~20/CCW

e-gun Voltage	Repetition Rate	Number of Pulses	MFC (read, sccm)	Needle valve(mTorr)
15 KV	1Hz	1000 (AlN), 10800(GaN)	190 sccm	N/A

Comments:

1. Raised SS bulb temperature to 1200^{o}C. Waited for 30 minutes before pressure went stable, after outgassing occurred and raised to $6.46x10^{-6}$ Torr, initially.
2. 10800 pulses of GaN were fired at 1Hz with an increased pressure of 33mTorr including some contribution from the needle valve.

P052

Substrate Batch #	Sample(s)/Block	Grower(s)	Dates
2" Sapphire Wafer, Lot. No: 238Z006, Cassette No: 01M4159	2 x 1cm^2 coupons	Arefin	12/08/13
3" Si(111) wafer	2 x 1cm^2 coupons	Arefin	12/08/13

Ex-situ Cleaning	Date	Comments
Running DI water, Acetone US, Methanol US, UHP N_2 Purge	12/09/2013	

Base Pressure (Torr)	Working Pressure (Torr)	Gun tip-to-Gas Tip (mm)	Tip-to-Target (mm)	Sub-to-Target (mm)	Target Rotation Speed (rpm)/Rot. Direction	Sub. Temp. (^{o}C)	Sub. Rotation Speed (rpm)
$4.87x10^{-7}$	$20x10^{-3}$	15	3 (1.685" HT)	50	~60/CCW	750	~20/CCW

e-gun Voltage	Repetition Rate	Number of Pulses	MFC (read, sccm)	Needle valve (read)
15 KV	(i) 1 Hz, (ii) 3Hz	8100	(2300, 180)	N/A

Comments:

1. Raised SS bulb temperature to 1200^{o}C and chamber pressure increased to 7.55 x 10^{-6} Torr (for out gassing). Waited for 30 minutes before pressure went stable.
2. Few hundred test pulses were fired at 1Hz, then another 500 @ 1Hz, then 5000 pulses @ 3Hz, and later 500 pulses @1Hz.
3. Final deposition was done at 18 mTorr, not using any needle valve.

P053

Substrate Batch #	Sample(s)/Block	Grower(s)	Dates
2" Sapphire Wafer, Lot. No: 238Z006, Cassette No: 01M4159	4 x 1cm^2 coupons	Arefin	02/10/14

Ex-situ Cleaning	Date	Comments
Running DI water, Acetone US, Methanol US, UHP N_2 Purge	02/09/2014	Dip in H_3PO_4:H_2SO_4=1:3 solution for 2-3 minutes

Base Pressure (Torr)	Working Pressure (Torr)	Gun tip-to-Gas Tip (mm)	Tip-to-Target (mm)	Sub-to-Target (mm)	Target Rotation Speed (rpm)/Rot. Direction	Sub. Temp. (^{o}C)	Sub. Rotation Speed (rpm)
$8.54x10^{-7}$	$7x10^{-3}$	15	3 (1.690" HT)	50	~60/CCW	700	~20/CCW

e-gun Voltage	Repetition Rate	Number of Pulses	MFC (read, sccm)	Needle valve (read)
11 KV	(i) 1 Hz, (ii) 3Hz, (iii) 5Hz	(i) 500, (ii) 1000, (iii) 1200	(2300, 180)	N/A

Comments:

1. Raised SS bulb temperature to 1180^{o}C (700^{o}C). Waited for 30 minutes before pressure went stable, after outgassing occurred.
2. 500 pulses were fired at 1Hz, then another 1000 @ 3Hz, then 1200 pulses @ 5Hz.
3. During growth the chamber pressure (Ar) was increased from 5.1mTorr to 7.1mTorr.

P054

Substrate Batch #	Sample(s)/Block	Grower(s)	Dates
2" Sapphire Wafer, Lot. No: 238Z006, Cassette No: 01M4159	4 x 1cm^2 coupons	Arefin	02/13/14

Ex-situ Cleaning	Date	Comments
Running DI water, Acetone US, Methanol US, UHP N_2 Purge	02/12/2014	Dip in H_3PO_4:H_2SO_4=1:3 solution for 2-3 minutes

Base Pressure (Torr)	Working Pressure (Torr)	Gun tip-to-Gas Tip (mm)	Tip-to-Target (mm)	Sub-to-Target (mm)	Target Rotation Speed (rpm)/Rot. Direction	Sub. Temp. (^{o}C)	Sub. Rotation Speed (rpm)
$6.57x10^{-7}$	$7.3x10^{-3}$	15	3 (1.690" HT)	50	~60/CCW	500	~20/CCW

e-gun Voltage	Repetition Rate	Number of Pulses	MFC (read, sccm)	Needle valve (read)
11 KV	(i) 1 Hz, (ii) 3Hz	(i) 750, (ii) 2000	(2300, 180)	N/A

Comments:

1. Raised SS bulb temperature to 915^{o}C (500^{o}C). Waited for 30 minutes before pressure went stable, after outgassing occurred and raised to $1.19x10^{-5}$Torr, initially.
2. 750 pulses were fired at 1Hz, then another 2000 @ 3Hz.
3. During growth the chamber pressure (Ar) was increased from 7.1mTorr to 7.3mTorr. Then another 0.3 mTorr was added by the needle valve to reach 7.6 mTorr for plasma optimization.

P055

Substrate Batch #	Sample(s)/Block	Grower(s)	Dates
2" Sapphire Wafer, Lot. No: 238Z006, Cassette No: 01M4159	4 x 1cm^2 coupons	Arefin	02/16/14

Ex-situ Cleaning	Date	Comments
Running DI water, Acetone US, Methanol US, UHP N_2 Purge	02/15/2014	Dip in H_3PO_4:H_2SO_4=1:3 solution for 2-3 minutes

Base Pressure (Torr)	Working Pressure (Torr)	Gun tip-to-Gas Tip (mm)	Tip-to-Target (mm)	Sub-to-Target (mm)	Target Rotation Speed (rpm)/Rot. Direction	Sub. Temp. (^{o}C)	Sub. Rotation Speed (rpm)
$4.61x10^{-7}$	$7.3x10^{-3}$	15	3 (1.640" HT)	50	~60/CCW	300	~20/CCW

e-gun Voltage	Repetition Rate	Number of Pulses	MFC (read, sccm)	Needle valve(mTorr)
11 KV	(i) 3Hz	(i) 2700	(2340, 180)	0.2

Comments:

1. Raised SS bulb temperature to 640^{o}C (300^{o}C). Waited for 30 minutes before pressure went stable, after outgassing occurred and raised to $3.60x10^{-6}$Torr, initially.
2. 2700 pulses were fired at 3Hz.
3. During growth the chamber pressure (Ar) was increased to 7.1 mTorr (using MFC). Then another 0.2 mTorr was added by the needle valve to reach 7.3 mTorr for plasma optimization.

P056

Substrate Batch #	Sample(s)/Block	Grower(s)	Dates
3" Si(111) wafer	2 x 1cm^2 coupons	Arefin	02/20/14

Ex-situ Cleaning	Date	Comments
Running DI water, Acetone US, Methanol US, UHP N_2 Purge	02/19/2014	

Base Pressure (Torr)	Working Pressure (Torr)	Gun tip-to-Gas Tip (mm)	Tip-to-Target (mm)	Sub-to-Target (mm)	Target Rotation Speed (rpm)/Rot. Direction	Sub. Temp. (^{o}C)	Sub. Rotation Speed (rpm)
$4.25x10^{-7}$	$15x10^{-3}$	15	2~3 (1.710" HT)	50	~60/CCW	850, 750	~20/CCW

e-gun Voltage	Repetition Rate	Number of Pulses	MFC (read, sccm)	Needle valve (read)
15 KV	3, 5 Hz	5000(AlN), 22000(GaN)	(2600, 203)	

Comments:

1. 5000 pulses of AlN was deposited first at 850^{o}C at 3 Hz.
2. Similar growth environment was applied to GaN deposition trying ~20000 pulses at 3 and 5 Hz.

P057

Substrate Batch #	Sample(s)/Block	Grower(s)	Dates
M204, M215	2 x 1cm^2 coupons	Arefin	03/03/14

Ex-situ Cleaning	Date	Comments
UHP N_2 Purge	03/02/2013	

Base Pressure (Torr)	Working Pressure (Torr)	Gun tip-to-Gas Tip (mm)	Tip-to-Target (mm)	Sub-to-Target (mm)	Target Rotation Speed (rpm)/Rot. Direction	Sub. Temp. (^{o}C)	Sub. Rotation Speed (rpm)
$6.37x10^{-7}$	$15x10^{-3}$	15	2~3 (1.380" HT)	50	~60/CCW	500	~20/CCW

e-gun Voltage	Repetition Rate	Number of Pulses	MFC (read, sccm)	Needle valve (read)
15 KV	1 Hz	10000	(2600, 203)	343

P058

Substrate Batch #	Sample(s)/Block	Grower(s)	Dates
2" Sapphire Wafer, Lot. No: 238Z006, Cassette No: 01M4159	4 x 1cm^2 coupons	Arefin	02/16/14

Ex-situ Cleaning	Date	Comments
Running DI water, Acetone US, Methanol US, UHP N_2 Purge	02/15/2014	Dip in H_3PO_4:H_2SO_4=1:3 solution for 2-3 minutes

Base Pressure (Torr)	Working Pressure (Torr)	Gun tip-to-Gas Tip (mm)	Tip-to-Target (mm)	Sub-to-Target (mm)	Target Rotation Speed (rpm)/Rot. Direction	Sub. Temp. (^{o}C)	Sub. Rotation Speed (rpm)
$5.76x10^{-7}$	$7.3x10^{-3}$	15	3 (1.670" HT)	50	~60/CCW	300	~20/CCW
	$15x10^{-3}$	15	3 (1.670" HT)	50	~60/CCW	300	~20/CCW

e-gun Voltage	Repetition Rate	Number of Pulses	MFC (read, sccm)	Needle valve(mTorr)
11 KV	3Hz	1000		
15KV	3Hz	15000	(2200, 175)	

Comments:

1. Raised SS bulb temperature to 640^{o}C (300^{o}C). Waited for 30 minutes before pressure went stable, after outgassing occurred and raised to $5.88x10^{-6}$Torr, initially.
2. 1000 pulses of ZnO were fired at 3Hz, in an environment of 7.3 mTorr Ar.
3. Switched from Ar to N_2 environment.
4. 15000 pulses of GaN were fired at 3Hz, in an environment of 14 mTorr Ar.
5. After stopping Ar flow, chamber was pumped with turbo-pump for 30 mins (to pump out any remaining).

P059

Substrate Batch #	Sample(s)/Block	Grower(s)	Dates
2" Sapphire Wafer, Lot. No: 238Z006, Cassette No: 01M4159	2 x 1cm^2 coupons	Arefin	03/13/14
3" Si(111) wafer	1 x 1cm^2 coupons	Arefin	03/13/14

Ex-situ Cleaning	Date	Comments
Running DI water, Acetone US, Methanol US, UHP N_2 Purge	03/12/2014	The PbSe/Cu was just N_2 purged

Base Pressure (Torr)	Working Pressure (Torr)	Gun tip-to-Gas Tip (mm)	Tip-to-Target (mm)	Sub-to-Target (mm)	Target Rotation Speed (rpm)/Rot. Direction	Sub. Temp. (^{o}C)	Sub. Rotation Speed (rpm)
$3.10x10^{-7}$	$7x10^{-3}$	15	2~3 (1.380" HT)	50	~60/CCW	RT	~20/CCW

e-gun Voltage	Repetition Rate	Number of Pulses	MFC (read, sccm)	Needle valve (read)
11 KV	5 Hz	20000		

Comments:

1. Ar pressure was carefully adjusted as above the threshold the electron-Ar interaction reduces plasma generation.

P060

Substrate Batch #	Sample(s)/Block	Grower(s)	Dates
2" Sapphire Wafer, Lot. No: 238Z006, Cassette No: 01M4159	1 x 1cm^2 coupons	Arefin	03/24/14
3" Si(111) wafer	1 x 1cm^2 coupons	Arefin	03/24/14

Ex-situ Cleaning	Date	Comments
Running DI water, Acetone US, Methanol US, UHP N_2 Purge	03/23/14	

Base Pressure (Torr)	Working Pressure (Torr)	Gun tip-to-Gas Tip (mm)	Tip-to-Target (mm)	Sub-to-Target (mm)	Target Rotation Speed (rpm)/Rot. Direction	Sub. Temp. (^{o}C)	Sub. Rotation Speed (rpm)
$2.25x10^{-7}$	$15x10^{-3}$	15	2~3 (1.956" HT)	~50	~60/CCW	400	~20/CCW

e-gun Voltage	Repetition Rate	Number of Pulses	MFC (read, sccm)	Needle valve (read)
15 KV	3 Hz	10000	(2600, 203)	343

Comments:

1. Chamber pressure was optimized throughout the whole experiment to ensure significant counts of Ga and N in the emission spectrum.

P061

Substrate Batch #	Sample(s)/Block	Grower(s)	Dates
2" Sapphire Wafer, Lot. No: 238Z006, Cassette No: 01M4159	2 x 1cm^2 coupons	Arefin	02/26/13
3" Si(111) wafer	2 x 1cm^2 coupons	Arefin	03/26/13

Ex-situ Cleaning	Date	Comments
Running DI water, Acetone US, Methanol US, UHP N_2 Purge	03/25/2013	M116 and M117 were only N_2 purged

Base Pressure (Torr)	Working Pressure (Torr)	Gun tip-to-Gas Tip (mm)	Tip-to-Target (mm)	Sub-to-Target (mm)	Target Rotation Speed (rpm)/Rot. Direction	Sub. Temp. (^{o}C)	Sub. Rotation Speed (rpm)
$4.06x10^{-7}$	$14x10^{-3}$	15	2~3 (1.956" HT)	~50	~60/CCW	500	~20/CCW

e-gun Voltage	Repetition Rate	Number of Pulses	MFC (read, sccm)	Needle valve (read)
15 KV	3 Hz	10000	188 sccm	

Comments:

1. Chamber pressure was optimized throughout the whole experiment to ensure significant counts of Ga and N in the emission spectrum.

P062

Substrate Batch #	Sample(s)/Block	Grower(s)	Dates
	(i) 1 x 1cm^2 coupon [Si(111)] (ii) 1 x 1cm^2 coupon [Ge/Si(111)] (iii) 1 x 1cm^2 coupon of M116 (iv) 1 x 1cm^2 coupon of M117	Arefin	03/28/14

Ex-situ Cleaning	Date	Comments
Running DI water, Acetone US, Methanol US, UHP N_2 Purge (ALL)	03/27/2014	(i) Dip in 25% HF solution for 2 minutes (ii) Dip in 25% HF solution for 30 sec

Base Pressure (Torr)	Working Pressure (Torr)	Gun tip-to-Gas Tip (mm)	Tip-to-Target (mm)	Sub-to-Target (mm)	Target Rotation Speed (rpm)/Rot. Direction	Sub. Temp. (^{o}C)	Sub. Rotation Speed (rpm)
$3.47x10^{-7}$	$14x10^{-3}$	15	3 (1.956" HT)	50	~60/CCW	600	~20/CCW

e-gun Voltage	Repetition Rate	Number of Pulses	MFC (read, sccm)	Needle valve(mTorr)
15 KV	3Hz	8100	190 sccm	N/A

Comments:

1. Raised SS bulb temperature to 600^{o}C (960^{o}C @ bulb). Waited for 30 minutes before pressure went stable, after outgassing occurred and raised to $8.00x10^{-6}$Torr, initially.
2. 8100 pulses of GaN were fired at 3Hz, in an environment of 14 mTorr N2, before gun stopped working for some error. Experiment not continued further.

P063

Substrate Batch #	Sample(s)/Block	Grower(s)	Dates
2" Sapphire Wafer, Lot. No: 238Z006, Cassette No: 01M4159	2 x 1cm^2 coupons	Arefin	04/11/14
3" Si(111) wafer	2 x 1cm^2 coupons	Arefin	04/11/14

Ex-situ Cleaning	Date	Comments
Running DI water, Acetone US, Methanol US, UHP N_2 Purge	04/10/14	M116 and M117 were only N_2 purged

Base Pressure (Torr)	Working Pressure (Torr)	Gun tip-to-Gas Tip (mm)	Tip-to-Target (mm)	Sub-to-Target (mm)	Target Rotation Speed (rpm)/Rot. Direction	Sub. Temp. (^{o}C)	Sub. Rotation Speed (rpm)
$3.47x10^{-7}$	$14x10^{-3}$	15	2~3 (1.956" HT)	~50	~60/CCW	700	~20/CCW

e-gun Voltage	Repetition Rate	Number of Pulses	MFC (read, sccm)	Needle valve (read)
15 KV	3 Hz	10000	188 sccm	

Comments:

1. Chamber pressure was optimized throughout the whole experiment to ensure significant counts of Ga and N in the emission spectrum.

P064

Substrate Batch #	Sample(s)/Block	Grower(s)	Dates
2" Sapphire Wafer, Lot. No: 238Z006, Cassette No: 01M4159	1 x 1cm^2 coupons	Arefin	04/12/14
3" Si(111) wafer	1 x 1cm^2 coupons	Arefin	04/12/14

Ex-situ Cleaning	Date	Comments
Running DI water, Acetone US, Methanol US, UHP N_2 Purge	04/11/14	M116 and M117 were only N_2 purged

Base Pressure (Torr)	Working Pressure (Torr)	Gun tip-to-Gas Tip (mm)	Tip-to-Target (mm)	Sub-to-Target (mm)	Target Rotation Speed (rpm)/Rot. Direction	Sub. Temp. (^{o}C)	Sub. Rotation Speed (rpm)
$2.86x10^{-7}$	$7x10^{-3}$ (Ar)	15	2~3 (1.956" HT)	~50	~60/CCW	700	~20/CCW

e-gun Voltage	Repetition Rate	Number of Pulses	MFC (read, sccm)	Needle valve (read)
15 KV	3 Hz	10000		

Comments:

1. Chamber pressure was optimized throughout the whole experiment to ensure significant counts of Ga and N in the emission spectrum.

P065

Substrate Batch #	Sample(s)/Block	Grower(s)	Dates
2" *p*-type Si(100), Lot. No: 5466328	A whole 2" wafer	Arefin	05/20/14

Ex-situ Cleaning	Date	Comments
Running DI water, Acetone US, Methanol US, UHP N_2 Purge	05/19/2014	Dip in 25% HF solution for 2-3 minutes

Base Pressure (Torr)	Working Pressure (Torr)	Gun tip-to-Gas Tip (mm)	Tip-to-Target (mm)	Sub-to-Target (mm)	Target Rotation Speed (rpm)/Rot. Direction	Sub. Temp. (^{o}C)	Sub. Rotation Speed (rpm)
$4.41\text{x}10^{-7}$	$7.2\text{x}10^{-3}$	15	3 (1.870" HT)	50	~60/CCW	500	~20/CCW

e-gun Voltage	Repetition Rate	Number of Pulses	MFC (read, sccm)	Needle valve(mTorr)
11 KV	3Hz	200+3000	150 sccm	

Comments:

1. Raised SS bulb temperature to 840^{o}C (wafer @ 500^{o}C). Waited for 30 minutes before pressure went stable, after outgassing occurred and raised to $5.41\text{x}10^{-6}$ Torr, initially.
2. 3200 pulses were fired at 5Hz. Some hundred pulses were fired previously to stabilize the plasma.
3. During growth the chamber pressure (Ar) was increased to 7.2 mTorr (using MFC). Then another 0.1 mTorr was added by the needle valve to reach 7.3 mTorr for plasma optimization. But later, using the needle valve gas feed proved not good in this experiment.

P066

Substrate Batch #	Sample(s)/Block	Grower(s)	Dates
2" *p*-type Si(100), Lot. No: 5466328	A whole 2" wafer	Arefin	05/22/14

Ex-situ Cleaning	Date	Comments
Running DI water, Acetone US, Methanol US, UHP N_2 Purge	05/20/2014	Dip in 25% HF solution for 2-3 minutes

Base Pressure (Torr)	Working Pressure (Torr)	Gun tip-to-Gas Tip (mm)	Tip-to-Target (mm)	Sub-to-Target (mm)	Target Rotation Speed (rpm)/Rot. Direction	Sub. Temp. (^{o}C)	Sub. Rotation Speed (rpm)
$2.75\text{x}10^{-7}$	$7.2\text{x}10^{-3}$	15	3 (1.830" HT)	50	~60/CCW	300	~20/CCW

e-gun Voltage	Repetition Rate	Number of Pulses	MFC (read, sccm)	Needle valve(mTorr)
11 KV	5Hz	3200	150 sccm	

Comments:

1. Raised SS bulb temperature to 640^{o}C (wafer @ 300^{o}C). Waited for 30 minutes before pressure went stable, after outgassing occurred and raised to $4.58\text{x}10^{-6}$ Torr, initially.
2. 3200 pulses were fired at 5Hz. Some hundred pulses were fired previously (1Hz, and 5Hz) to stabilize the plasma.

3. During growth the chamber pressure (Ar) was increased to 7.2 mTorr (using MFC). Then another 0.1 mTorr was added by the needle valve to reach 7.3 mTorr for plasma optimization. This time adding the needle valve feed was better in response.

P067

Substrate Batch #	Sample(s)/Block	Grower(s)	Dates
2" *p*-type Si(100), Lot. No: 5466328	A whole 2" wafer	Arefin	06/01/14
Ex-situ Cleaning	**Date**	**Comments**	
Running DI water, Acetone US, Methanol US, UHP N_2 Purge	05/31/14	Dip in 25% HF solution for 2-3 minutes	

Base Pressure (Torr)	Working Pressure (Torr)	Gun tip-to-Gas Tip (mm)	Tip-to-Target (mm)	Sub-to-Target (mm)	Target Rotation Speed (rpm)/Rot. Direction	Sub. Temp. (^oC)	Sub. Rotation Speed (rpm)
$1.60x10^{-7}$	$7.2x10^{-3}$	15	3 (1.830" HT)	50	~60/CCW	300	~20/CCW

e-gun Voltage	Repetition Rate	Number of Pulses	MFC (read, sccm)	Needle valve(mTorr)
11 KV	5Hz	3200	150 sccm	

Comments:

1. Deposition was not good as plasma was not significant, possibly due to increased incident angle on target surface due to grooving from electron bombardment.

P068

Substrate Batch #	Sample(s)/Block	Grower(s)	Dates
n-Si-(111)	$3x1cm^2$	Arefin	07/25/14

Ex-situ Cleaning	Date	Comments
Running DI water, Acetone US, Methanol US, UHP N_2 Purge	07/24/14	Dip in 25% HF solution for 2-3 minutes

Base Pressure (Torr)	Working Pressure (Torr)	Gun tip-to-Gas Tip (mm)	Tip-to-Target (mm)	Sub-to-Target (mm)	Target Rotation Speed (rpm)/Rot. Direction	Sub. Temp. (^oC)	Sub. Rotation Speed (rpm)
$1.60x10^{-7}$	$12x10^{-3}$	15	3 (1.990" HT)	50	~60/CCW	200	~20/CCW

e-gun Voltage	Repetition Rate	Number of Pulses	MFC (read, sccm)	Needle valve(mTorr)
15 KV	5Hz	10000	165 sccm	

P069

Substrate Batch #	Sample(s)/Block	Grower(s)	Dates
n-Si-(111)	$3x1cm^2$	Arefin	07/30/14

Ex-situ Cleaning	Date	Comments
Running DI water, Acetone US, Methanol US, UHP N_2 Purge	07/29/14	Dip in 25% HF solution for 2-3 minutes

Base Pressure (Torr)	Working Pressure (Torr)	Gun tip-to-Gas Tip (mm)	Tip-to-Target (mm)	Sub-to-Target (mm)	Target Rotation Speed (rpm)/Rot. Direction	Sub. Temp. (^{o}C)	Sub. Rotation Speed (rpm)
$1.60x10^{-7}$	$10x10^{-3}$	15	3 (1.990" HT)	50	~60/CCW	RT	~20/CCW

e-gun Voltage	Repetition Rate	Number of Pulses	MFC (read, sccm)	Needle valve(mTorr)
15 KV	5Hz	10000	165 sccm	

P070

Substrate Batch #	Sample(s)/Block	Grower(s)	Dates
n-Si-(111)	$1x1cm^2$	Arefin	08/03/14

Ex-situ Cleaning	Date	Comments
Running DI water, Acetone US, Methanol US, UHP N_2 Purge	08/02/14	Dip in 25% HF solution for 2-3 minutes

Base Pressure (Torr)	Working Pressure (Torr)	Gun tip-to-Gas Tip (mm)	Tip-to-Target (mm)	Sub-to-Target (mm)	Target Rotation Speed (rpm)/Rot. Direction	Sub. Temp. (^{o}C)	Sub. Rotation Speed (rpm)
$2.77x10^{-7}$	$6x10^{-3}$	15	3 (1.995" HT)	50	~60/CCW	RT	~20/CCW

e-gun Voltage	Repetition Rate	Number of Pulses	MFC (read, sccm)	Needle valve(mTorr)
12 KV	3Hz	10000	145 sccm	

Comments:

1. The MBE grown samples were purged with N_2.
2. Again metal contamination occurred during growth (possibly too much energy pulsed).

P071

Substrate Batch #	Sample(s)/Block	Grower(s)	Dates
		Arefin	08/06/14

Ex-situ Cleaning	Date	Comments
All samples were N_2 purged	08/05/14	

Base Pressure (Torr)	Working Pressure (Torr)	Gun tip-to-Gas Tip (mm)	Tip-to-Target (mm)	Sub-to-Target (mm)	Target Rotation Speed (rpm)/Rot. Direction	Sub. Temp. (^{o}C)	Sub. Rotation Speed (rpm)
$9.43x10^{-7}$	$5.7x10^{-3}$	15	3 (1.980" HT)	50	~60/CCW	200	~20/CCW

e-gun Voltage	Repetition Rate	Number of Pulses	MFC (read, sccm)	Needle valve(mTorr)
11 KV	3Hz	10000	140 sccm	

P072

Substrate Batch #	Sample(s)/Block	Grower(s)	Dates
		Arefin	08/07/14

Ex-situ Cleaning	Date	Comments
All samples were N_2 purged	08/06/14	

Base Pressure (Torr)	Working Pressure (Torr)	Gun tip-to-Gas Tip (mm)	Tip-to-Target (mm)	Sub-to-Target (mm)	Target Rotation Speed (rpm)/Rot. Direction	Sub. Temp. (^oC)	Sub. Rotation Speed (rpm)
$4.47x10^{-7}$	$10x10^{-3}$	15	3 (1.852" HT)	50	~60/CCW	500	~20/CCW

e-gun Voltage	Repetition Rate	Number of Pulses	MFC (read, sccm)	Needle valve(mTorr)
15 KV	1,3Hz	10000	155 sccm	

P073

Substrate Batch #	Sample(s)/Block	Grower(s)	Dates
		Arefin	08/26/14

Ex-situ Cleaning	Date	Comments
All samples were N_2 purged	08/25/14	

Base Pressure (Torr)	Working Pressure (Torr)	Gun tip-to-Gas Tip (mm)	Tip-to-Target (mm)	Sub-to-Target (mm)	Target Rotation Speed (rpm)/Rot. Direction	Sub. Temp. (^oC)	Sub. Rotation Speed (rpm)
$5/06x10^{-7}$	$10x10^{-3}$	15	3 (1.852" HT)	50	~60/CCW	500	~20/CCW

e-gun Voltage	Repetition Rate	Number of Pulses	MFC (read, sccm)	Needle valve(mTorr)
15 KV	2Hz	10000	155 sccm	

P074

Substrate Batch #	Sample(s)/Block	Grower(s)	Dates
Sapphire	$1cm^2$ coupons	Arefin	08/28/14
Si(111) and Ge/Si(111)	$1cm^2$ coupons	Arefin	08/28/14

Ex-situ Cleaning			Date		Comments		
Running DI water, Acetone US, Methanol US, UHP N_2 Purge			08/27/14		Samples were etched		
Base Pressure (Torr)	**Working Pressure (Torr)**	**Gun tip-to-Gas Tip (mm)**	**Tip-to-Target (mm)**	**Sub-to-Target (mm)**	**Target Rotation Speed (rpm)/Rot. Direction**	**Sub. Temp. (^oC)**	**Sub. Rotation Speed (rpm)**
$4.75x10^{-7}$	$10x10^{-3}$	15	2~3 (1.830" HT)	~50	~60/CCW	600	~20/CCW

e-gun Voltage	Repetition Rate	Number of Pulses	MFC (read, sccm)	Needle valve (read)
15 KV	3, 5 Hz	10000	141 sccm	

Comments:

1. Chamber pressure was optimized throughout the whole experiment to ensure significant counts of Ga and N in the emission spectrum.